

Abstract of “Experimental Studies of the Bragg Glass Transition in Niobium.” by Nikolaos Daniilidis, Ph.D., Brown University, May 2008.

One very fascinating result in condensed matter physics in recent decades is the realization that long-range topological order associated with broken continuous symmetries can survive in systems with weak quenched disorder. For vortex lattices in type-II superconductors this property implies the existence of a new state of matter, called Bragg Glass. Previous experiments showed that weakly-pinned vortex lattices in type-II superconductors undergo an order-disorder transition between the Bragg Glass and a structurally disordered high-temperature phase. This phase transition seems to be the underlying mechanism of the well-known peak effect anomaly in critical current.

We performed an experimental investigation of various aspects of the Bragg Glass transition in a niobium single crystal which displays the peak effect. We present a combination of calorimetric, magnetocaloric, and ac-susceptibility studies. These allow us to evaluate the roles and relative importance of sample inhomogeneity, thermal fluctuations, and surface effects on the evolution and disappearance of the peak effect in our niobium single crystal. Our findings suggest that the disappearance of the peak effect at low fields, which is widely reported in the literature, is not related to surface superconductivity. We propose two alternative scenarios that can explain the experimentally observed absence of the peak effect at low fields.

In addition to the above, we present small angle neutron scattering measurements of flux-line lattice translational correlations in the neighborhood of the peak effect. These allow us to observe the evolution of the disordered phase as it gradually transforms into the Bragg Glass phase through thermal cycling. This structural information allows us to propose a general process by which Bragg Glass crystallization

occurs via the annealing of defects in vortex lattices. This process can be of interest in studies of polymer crystallization and two-dimensional glasses.

Experimental Studies of the Bragg Glass Transition in Niobium.

by

Nikolaos Daniilidis

Electrical Engineering Diploma, National Technical University of Athens, 2001
Sc. M., Brown University, 2003

A dissertation submitted in partial fulfillment of the
requirements for the Degree of Doctor of Philosophy
in the Department of Physics at Brown University

Providence, Rhode Island

May 2008

© Copyright 2008 by Nikolaos Daniilidis

This dissertation by Nikolaos Daniilidis is accepted in its present form by
the Department of Physics as satisfying the dissertation requirement
for the degree of Doctor of Philosophy.

Date _____

Prof. Xinsheng S. Ling, Advisor

Recommended to the Graduate Council

Date _____

Prof. C. Elbaum, Reader

Date _____

Prof. V. F. Mitrović, Reader

Approved by the Graduate Council

Date _____

Sheila Bonde
Dean of the Graduate School

Acknowledgements

Completion of a Doctorate thesis is the capstone of an entire segment of one's life. As such, there is a potentially endless list of people who have contributed to the long journey. Still, I will have to attempt reflecting on mine.

In the last five years I benefited greatly by the diligent, conscientious efforts of my teachers here at Brown: My advisor, Sean Ling, whose discussions about Vortex Physics were such a fertile ground for scientific ideas. Professor Charles Elbaum whose learned historical outlook put my claims, often far-reached, in perspective. Professor Vesna Mitrovic, from whose fresh eye on Condensed Matter Physics I benefited. The criticism of the three, no matter how severe, was most welcome. Their guidance has been professional, sincere, sometimes contradicting; I feel confident I am departing with the best of three worlds in my baggages.

On the battlefield of the lab, my work benefited considerably from the help, technical when new skills were required, physical when the long hours would bear-down on my stamina, psychological when all prospects looked bleak, of Ivo Dimitrov and Sang Park, the graduate students with which I overlapped in the "Vortex Lab". Great thanks to both of thee. I will always be mindful of the confident helping-hand offered by Ambarish Ghosh, at times when the simplest tasks seemed daunting. Many thanks to Andrew Callen-Jones for our occasional informal discussions about this –or the other– topic in Condensed Matter Physics; the discussions did not go too far in specific, but certainly allowed us to dig-out knowledge that would otherwise have

been left buried in oblivion. Finally lot's of respect to our own computer "guru" Daniel Ferrante for devoting some *cpu* time and expertise to my demands.

My deepest feelings go to those who provided me with a memorable living environment here in Providence. First and foremost I must thank my girlfriend, Jennifer Pereira, for her soothing presence outside the lab and for helping me enjoy all the simple things one tends to miss in the daily grind. Once again, I wish to thank the fore-mentioned friends, Ivo, Andrew, Daniel for their good company, day-in and day-out, in Barus & Holley, the Coffee Exchange or the OMAC. The same goes to the Donos couple, Aristos and Maria, for spirited nights, lovely cooking and great company. Last, but not least, I wish to thank Mark Canon and Jerrah Covielo, for their friendship and hospitality, and for revealing to me the mystery that is life outside of graduate school.

Of course, my gratitude extends far beyond Providence. All these years I found great consolation in the continuous support and reassurance from the members of my family. Many thanks to my parents, Danilos and Mary, my sister, Lena, to Ioanna and Gavrilos. Part of the sacrifice is theirs. I know the list can go on for many more pages. Many amazing people from Greece, among them my friends, my teachers from past schools deserve their place in these pages. Once more, many thanks.

Contents

List of Tables	ix
List of Figures	x
1 Vortex matter and the peak effect problem	1
1.1 Introduction	1
1.2 Ginzburg-Landau theory	2
1.3 The Abrikosov solution	5
1.4 The H_{c2} transition	7
1.5 The pinning problem	11
1.6 Transport and critical currents	15
1.7 The Peak Effect	21
1.8 Overview	26
2 Experimental Techniques	28
2.1 Introduction	28
2.2 Calorimetric measurements	30
2.2.1 Principle of relaxation calorimetry	30
2.3 Magnetocaloric measurements	34
2.3.1 Basic Principle	34

2.3.2	Irreversible and non-equilibrium effects	37
2.4	Calorimetric setup	40
2.4.1	Calorimeter design	40
2.4.2	Experimental procedures	42
2.5	Magnetic ac susceptometry	44
2.5.1	Basic experimental setup	44
2.5.2	Application for superconductors	46
2.6	Small Angle Neutron Scattering	47
2.6.1	General treatment of neutron scattering	48
2.6.2	Small angle scattering rocking-curve measurements	50
2.6.3	The rocking-curve resolution function	54
2.6.4	Small angle scattering setup	58
2.7	The niobium sample and sample properties	60
3	Magnetocaloric and Calorimetric Measurements	62
3.1	Introduction	62
3.2	Calorimetric Measurements	65
3.3	Magnetocaloric Measurements	68
3.3.1	Discussion	78
3.3.2	Summary and discussion	84
4	Flux-lattice longitudinal correlation measurements at the Bragg Glass transition	87
4.1	Introduction	87
4.2	Experimental findings	89
4.2.1	General features	90
4.2.2	Qualitative features	92

4.2.3	Quantitative analysis	94
4.3	The process of Bragg Glass crystallization	100
4.4	Summary	102
5	Conclusions	103
5.1	Introduction	103
5.2	Insight from Magnetocalorics	104
5.3	Insight from SANS rocking-curve measurements	108
Bibliography		111

List of Tables

List of Figures

1.1	The $H - T$ phase diagram corresponding to Abrikosov's solution of the mixed state problem. At low fields the superconductor is in the perfectly diamagnetic Meissner state. At fields higher than H_{c1} it enters the mixed state, with periodic a vortex lattice (shown is an example of hexagonal arrangement of vortices). At even higher fields, H_{c2} , superconductivity is destroyed by the magnetic field.	7
1.2	(a) Loop excitation in an isolated vortex line. The directions of the arrows are in the sense of the flux of the vortex segments. The vortex line shifts from configuration “1” to configuration “2”. (b) Loop excitation involving multiple vortex lines. These schematics are adapted from Fisher, Fisher, and Huse [1].	19
1.3	Peak effect in critical current, versus applied field or temperature. We mark the onset H_{on} or T_{on} , the peak H_p or T_p , and the end H_{end} or T_{end} of the peak effect. The upper critical field (H_{c2} or T_{c2}) can be higher than the end of the peak effect.	22

1.4 Schematic of a typical peak-effect phase diagram, found in conventional superconductors. The peak effect line separates an ordered Bragg Glass phase at low temperature from a disordered phase at high temperatures. The nature of the high-temperature disordered phase is unresolved. The peak effect line might [2] or might not [3] terminate on the upper critical field line, H_{c2}	24
2.1 Idealized heat-flow diagram of a calorimeter used for the relaxation (heat-pulse) technique. The sample, at temperature T_s is heated by an external heater via regulated input P_{in} . It is thermally connected to the heat bath at temperature T_{bath} through a heat link of conductance G_{link} . The heat flow through the link is P_{out}	31
2.2 (a)-(c) Schematic representations of the asymmetries induced by irreversible and non-equilibrium effects on the magnetocaloric measurement, $ \Delta T $. The field ramp directions are indicated by arrows, and the equilibrium $(\partial s/\partial H)_T$ curve corresponds to the dashed line. (a) Surface barrier heating. (b) Flux flow heating. (c) Critical state screening. (d) Qualitative schematic of the evolution of the critical state field profile, for increasing field and $\partial j_c/\partial H < 0$. When the applied field increases from H to $H + \delta H$, the flux increase corresponds to the total shaded area, not just the lower shaded part. This results in increased magnetocaloric signal, as shown in (c) and discussed in the text. . . .	38

2.3 Design of the calorimeter used in our measurements. An outer brass can is used to maintain the vacuum conditions. An inner OFHC copper can serves the role of the heat bath, maintained at 4.2 K. The two are joined together by a thermal-contraction based thermal contact which uses an aluminum ring. The inner can is thermally connected to the sample via a piece of high-purity copper wire. The wire is attached to two OFHC copper disks using 95/5 (Sn-Sb) solder. One disk is attached to the sample using conductive silver epoxy. The other is fastened onto the heat-bath can with a brass screw. For simplicity we do not show the thermometers, sample heater, and ac-susceptometry coil.	41
2.4 Circuit diagram for the ac-susceptometry setup used in our measurements. A signal generator provides the input voltage, V_{in} . A shunt resistor, R_s , is used to provide the in-phase signal to the reference channel of the lock-in amplifier. The coil is directly wound on the sample. The voltage on the coil terminals is fed into the signal channel of the lock-in amplifier.	45
2.5 Scattering geometry in SANS measurements. The sample and magnetic field (thus, the flux line lattice) are rotated by ω with respect to the incident neutron beam. The diffracted neutrons satisfy the Bragg condition at angles θ_B .	52

3.4 Specific heat measurements at an applied field of 3052 Oe. The measurements were performed upon in field cooling (FC) and subsequent field cooled warming (FCW). The behavior is reversible to within our resolution.	68
3.5 Superconducting transition widths as a function of applied field from the specific heat measurements. No change is detectable as the field is varied.	68
3.6 Magnetocaloric temperature variation around $T_{s0} = 5.37$ K vs. applied field, for increasing and decreasing field. The field ramp direction is indicated by arrows. $dH/dt = 0.92$ Oe / sec was used.	69
3.7 Results of magnetocaloric measurements on (a) increasing and (b) decreasing field. Also shown (in blue) are the loci traced on the $H - T$ plane by H_p , H_{c2}^{up} , and H_{c3} . The H_{c3} line is drawn according to Park <i>et al.</i> [2]. (c) Full field scan at $T_{s0} = 4.83$ K. Grey: Increasing field. Black: Decreasing field. The fields H_1 and H_{knee} , and the upper limit of the upper critical field are marked.	72
3.8 (a) Magnetocaloric temperature variations and ac magnetic susceptibility for increasing field, at $T = 5.76$ K. The peak effect in χ' is not pronounced due to the small ac amplitude used ($h_{ac} = 0.5$ Oe, $f = 107$ Hz). (b) Detail of magnetocaloric measurement in the upper critical field region at $T = 4.83$ K. Grey: increasing field. Black: Decreasing field. (c) Same as b, at $T = 8.15$ K.	75

3.9 Normalized entropy derivative (ds/dH) versus $\Delta H = H - H_{c2}^{\text{up}}$, for the magnetocaloric data in the upper critical field region. (ds/dH) is rescaled to unity in the ΔH region between -300 and -250 Oe. (a) Increasing field data with and without the peak effect. The 7.41 K data do not show peak effect. The upper critical field shows inhomogeneity broadening between fields H_0 and H_{c2}^{up} . (b) Same as a for decreasing field. (c) Collapsed magnetocaloric curves without peak effect, for increasing (top, vertically offset by +0.2) and decreasing (bottom) fields. Temperatures included: 7.18 K, 7.41 K, 7.55 K, 7.94 K, 8.15 K, 8.33 K. 77

3.10 Phase diagram obtained from magnetocaloric measurements. (a) The identified features in $H - T$ axes. The thin solid line and wide shaded line are linear fits through H_p and H_{c2}^{av} . The width of the H_{c2} line represents the extent of inhomogeneity broadening. The location of the MCP after Park *et al.* is indicated. (b) Detail of the upper critical field region: distance of various features from the conventionally defined H_{c2}^{up} line, vs. H_{c2}^{av} . The shaded area corresponds to the upper critical field region. 80

3.11 Integrals of $(ds/dH)_n$ for ΔH from -150 Oe to 30 Oe, for increasing (\mathcal{F}_{up} , \blacktriangle) and decreasing (\mathcal{F}_{down} , \blacktriangledown) fields. The peak effect feature was not observed at these temperatures. The error bars reflect the uncertainty in alignment of the magnetocaloric curves. Temperatures above 8.15 K correspond to the H_{c2} line of transitions indicated by Park *et al.* [2]. 82

4.1	Typical integrated intensity versus temperature (red data points) and quadratic fit of the form $I = I_0 \cdot (T - T_{c2})^2$ (black line). The fit yields a $T_{c2} = 4.71$ K, in accordance with the phase diagrams in earlier work [4] and with Chapter 3. The data shown correspond to the (1,-1) peak according to the notation defined in Fig. 4.2	90
4.2	Typical succession of SANS patterns in a vortex lattice rocking curve measurement. The SANS detector lies on the xy plane. The data shown were obtained on FCW at $T = 3.35$ K, $H = 4000$ Oe. Rotation angles, left to right, are $\omega = -0.30^\circ, -0.20^\circ, -0.10^\circ, 0.00^\circ, 0.10^\circ, 0.20^\circ, 0.30^\circ$. We use the peak labeling scheme shown in (f).	91
4.3	(a) Normalized intensity versus rotation angle for the (1,-1) Bragg peak at different temperatures on both FC and FCW paths. Also shown are fitted Lorentzian curves. Inset: Geometry of the rocking curve measurement. (b) Half width of Lorentzian fits to the rocking curve data. FC is in blue, FCW in black. Arrows also indicate thermal history. The locations of the peak of the peak effect (T_P) and superconducting transition (T_{c2}) are marked. Grey lines are linear fits performed on the data points within the ranges where the lines are drawn.	93
4.4	Azimuthal widths of Bragg peaks on the $q_x q_y$ plane, in agreement with Ref.[4]	94

4.5	(a)Fits to a FCW rocking curve. Dashed line is a Lorentzian structure function convoluted with the resolution function. Solid line is the two-component fit. (b) Longitudinal correlation length L_z , in the disordered phase. Blue symbols: FC, black symbols: FCW. (c) Volume fraction of Bragg Glass phase in the coexistence picture, for FCW and FC paths. The values shown in (b) and (c) are averages of values obtained from four peaks, error bars are variances about the average.	96
5.1	Schematic of the phase $H - T$ phase diagram of the niobium single crystal used in this work. Three distinct regions are designated: The grey region corresponds to the formation of a vortex lattice. In it, Lowest Landau Level fluctuation effects are significant but not the sole significant factor, since normal regions still exist in the sample. The purple region has insignificant fluctuation effects, i.e. vortices are well formed in this region. In this region the equilibrium vortex lattice is structurally disordered. The blue region is a Bragg glass with insignificant fluctuation effects. The Meissner phase is not shown, for simplicity.	106
5.2	Schematic representation of the process by which the vortex lattice formation proceeds in our niobium single crystal. We show a snapshot of the system in the temperature region where parts of the sample are still normal (red regions). The vortex lines (also in red) inside the superconducting grains (in purple) are tilted with respect to the applied field due to geometric factors and pinning. This process naturally leads to formation of vortex lattice defects upon cooling, in the regions where the domains join each other.	109

Chapter 1

Vortex matter and the peak effect problem

1.1 Introduction

Superconductors have been fascinating researchers all over the world for almost 100 years now. A microscopic theory of conventional superconductivity has been around for 50 years. Still, a lot is to be understood on the behavior of these so-called “conventional” superconductors, a constant reminder that “More is Different”.

Practical questions, such as how to maximize critical currents and defend a device from thermal instabilities, as well as fundamental questions such as how many different superconducting phases exist in nature and if these superconducting phases are “really superconducting” remain open. These questions are the offspring of a remarkable statement made by Alexei Abrikosov 50 years ago: certain superconductors, the ones we call type-II, in a range of magnetic fields and temperatures will spontaneously form a periodic lattice of vortices: topological defects of the superfluid order parameter. This vortex lattice is accompanied by an identical periodic arrangement

of the local magnetic field in the interior of the superconductor.

The Abrikosov lattice is theoretically significant because it is a new phase of matter. It is of great practical value because it is involved in the dissipative processes that take place in any superconducting wire. In this work we try to answer certain questions concerning the peak effect anomaly in the critical current of a superconductor. This has attracted a lot of attention lately in relation to an underlying phase transition of the vortex lattice. In the rest of this chapter we introduce, one-by-one, the ingredients that make up the recipe of the Abrikosov state in a realistic system.

First we introduce the Ginzburg-Landau field theoretic language of our conversation. We then proceed to present Abrikosov's mean field solution to the Ginzburg-Landau equations for an ideal type-II superconductor. This solution defines the upper critical field H_{c2} . The nature of the phase transition at H_{c2} is altered by thermal fluctuations, as we will discuss. Next we turn to the problem of pinning, essential to the treatment of any real system. In this context, the seminal idea of a Bragg Glass phase is introduced. Transport properties and the impact of pinning on those is discussed next. Finally, we introduce the peak effect problem and discuss some old and contemporary views and developments in studying this fascinating problem.

1.2 Ginzburg-Landau theory

The starting point for any treatment of a superconductor with local variations in the superfluid density is the Ginzburg-Landau free energy. This, in the general spirit of Landau theories, offers an expansion of the free energy density of the superconductor in powers of a complex order parameter ψ . To fourth order in ψ one gets

$$F_s = F_n + \int \left\{ \alpha |\psi|^2 + \frac{1}{2} \beta |\psi|^4 + \frac{1}{2m^*} \left| \left(\frac{\hbar}{i} \nabla - \frac{e}{c} \mathbf{A} \right) \psi \right|^2 + \frac{(\nabla \times \mathbf{A})^2}{8\pi} \right\} d^3r. \quad (1.1)$$

F_n is the free energy of the normal metal. The local superfluid density is proportional to the squared modulus of the complex order parameter, $|\psi|^2 = |\psi(r)|^2$. This, as well as the local magnetic field $h(\mathbf{r}) = \nabla \times \mathbf{A}(\mathbf{r})$, can vary spatially [5]. The free energy has a global minimum for $\psi = 0$ when $\alpha > 0$, and $\psi = 0$ corresponds to the normal state. Superconductivity arises when $\alpha \equiv a' \cdot (T/T_c - 1) < 0$, that is when $T < T_c$.

The free energy of the above form was proposed before the development of a microscopic theory of superconductivity, and was later derived from the self-consistent, mean field formulation of the microscopic theory by Gor'kov [6]. In the language of the self-consistent microscopic theory, the complex order-parameter corresponds to the spatially varying gap parameter, $\Delta(\mathbf{r})$.

The free energy density can be separated into three contributions. A condensation energy term

$$\alpha |\psi|^2 + \frac{1}{2} \beta |\psi|^4 .$$

A gauge invariant “kinetic energy” term

$$\frac{1}{2m^*} \left| \left(\frac{\hbar}{i} \nabla - \frac{e}{c} \mathbf{A} \right) \psi \right|^2 .$$

The magnetic field energy density

$$\frac{(\nabla \times \mathbf{A})^2}{8\pi} .$$

Minimization of the free energy with respect to variations of the order parameter and the vector potential leads to the Ginzburg-Landau equations

$$\alpha\psi + \beta |\psi|^2 \psi + \frac{1}{2m^*} \left(\frac{\hbar}{i} \nabla - \frac{e^*}{c} \mathbf{A} \right)^2 \psi = 0 , \quad (1.2)$$

$$\mathbf{J} = \frac{e^* \hbar}{2m^* i} (\psi^* \nabla \psi - \psi \nabla \psi^*) - \frac{e^{*2}}{m^* c} |\psi|^2 \mathbf{A} , \quad (1.3)$$

with an appropriate boundary condition, e.g $\left(\frac{\hbar}{i} \nabla - \frac{e^*}{c} \mathbf{A} \right) \psi \cdot \mathbf{n} = 0$, on the sample surface. These equations define a characteristic length, corresponding to the lengthscales

over which ψ varies . This is the so called Ginzburg-Landau coherence length, given by $\xi = \frac{\hbar}{(2m^* |\alpha|)^{1/2}}$. The parameters involved in the free energy expansion, Eq. 1.1, are related to other measurable quantities. For example, the condensation energy density at some temperature $T < T_c$, is $\frac{F_s - F_n}{V} = -\frac{\alpha^2}{2\beta}$. The London penetration depth equals $\lambda = \frac{m^* c^2 \beta^2}{4\pi \alpha^2 e^{*2}}$. It is convenient to take the effective mass to be $m^* = 2m$, and the starred charge to be the Cooper pair charge $e^* = 2e$. In this case, the superfluid density is just $n_s = 2|\psi|^2$.

The Ginzburg-Landau free energy offers the basis for the classification of superconductors into type-I and type-II. It can be shown that the free energy contribution of a superconducting-to-normal interface in a superconductor is positive for $\kappa \equiv \frac{\lambda}{\xi} < \frac{1}{\sqrt{2}}$ and negative for $\kappa > \frac{1}{\sqrt{2}}$. This property has important consequences on the behavior of superconductors in the presence of magnetic fields. For a type-I material, geometric demagnetization effects can make partial magnetic flux penetration in a sample energetically favorable. In this situation, the S-N interfaces tend to be minimized, resulting in the lamellar magnetic structures observed in the so-called intermediate state. For a type-II material, when magnetic flux penetrates the system tends to maximize the S-N interface area by breaking the flux-carrying regions into small tubes, the vortices. The lower limit on the size of these is set by the requirement that each flux tube carry the minimum amount of magnetic flux compatible with a phase coherent order parameter. This minimum amount of flux defines the “flux quantum”, given by $\Phi_0 = \frac{hc}{2e} = 2.07 \times 10^{-7} \text{ G cm}^2$.

These flux lines carry one fluxon each. They are topological defects of the complex order parameter, and consist of a core region of radius ξ . In the core region the superfluid density drops to zero and low lying electronic excitations are present [6, 7]¹. The magnetic field drops exponentially as $e^{-r/\lambda}$ away from the core. As a result,

¹This is the case in conventional superconductors. In systems with non *s*-wave pairing, nodal quasiparticles are present outside of the core regions.

one can treat superconducting vortices as line objects. These possess a line tension, related to the condensation energy loss in the core, and interact with each other via their magnetic field profiles. The idea of a vortex as a line-object has proved to be an extremely useful conceptual step in understanding the mixed state of type-II superconductors. It allows one to treat the vortex state as an emergent matter with macroscopic, vortex, degrees of freedom.

1.3 The Abrikosov solution

The development that essentially gave rise to the field nowadays known as “Vortex Physics”, was the realization by A. Abrikosov that in the mixed state the flux lines, that tend to repel each other due to their magnetic interaction, would minimize their energy by forming a regular periodic array. Abrikosov constructed a periodic lattice solution starting from the linearized Ginzburg-Landau equations, which are valid for $\psi \approx 0$ in the neighborhood of H_{c2} [8].

The periodic solution can be written as a linear superposition of the solutions to the linearized form of Eq. 1.2. This is a Schrödinger equation for the order parameter ψ . For applied field $\mathbf{H} = H\mathbf{z}$ in the \mathbf{z} direction, working in the Landau gauge $\mathbf{A} = (0, Hx, 0)$, we obtain

$$\left[-\nabla^2 + 2i\frac{x}{\tilde{\xi}}\frac{\partial}{\partial y} + \left(\frac{x}{\tilde{\xi}^2}\right)^2 \right] \psi = \frac{1}{\tilde{\xi}^2} \psi, \quad (1.4)$$

with the definition $\tilde{\xi}^2 = \frac{2\pi H}{\Phi_0}$. This equation has solutions of the form

$$\psi(\mathbf{r}) \propto e^{ik_y y} e^{ik_z z} H_n\left(\frac{x - x_0}{\tilde{\xi}}\right) e^{-\frac{1}{2}(x - x_0)^2/\tilde{\xi}^2}, \quad (1.5)$$

where $x_0 = \tilde{\xi}^2 k_y$, and $H_n(x)$ a Hermite polynomial of order n . Thus, the solutions for ψ come in quantized Landau orbitals. These solutions are possible for values of

the applied field satisfying

$$H(n, k_z) = \frac{\Phi_0}{2\pi(2n+1)} \left(\frac{1}{\xi^2} - k_z^2 \right). \quad (1.6)$$

Therefore, the upper critical field is just the highest field for which a solution of the linearized G-L equation is possible, and it is given by the well known result

$$H_{c2} = \frac{\Phi_0}{2\pi\xi^2}. \quad (1.7)$$

This corresponds to $n = 0$. Thus the superfluid order parameter in the neighborhood of the upper critical field can be constructed from Lowest Landau Level (LLL) orbitals. This property is the basis for statistical mechanical treatments of the superconductor in the neighborhood of the upper critical field, and we shall return to it later.

The Abrikosov periodic solution, with periodicity a_0 in the y direction, is expressed as a sum of $n = 0$ Landau orbitals

$$\Psi_A(\mathbf{r}) = \sum_n C_n e^{inqy} e^{-(x-x_n)/2\xi^2} e^{ik_z z}. \quad (1.8)$$

Here $q = 2\pi/a_0$ and $x_n = nq\Phi_0/2\pi H$. The periodicity in the x direction is determined by the periodicity of coefficients C_n .

The symmetry of the vortex lattice can be determined by introducing the trial solution of the above form into the G-L free energy, Eq. 1.1. The ψ^4 term lifts the degeneracy between solutions of different symmetry. The minimum free energy solution in the neighborhood of the upper critical field has hexagonal symmetry, corresponding to the choice $C_{n+2} = C_n$, and $C_1 = iC_0$. In this case, it is trivial to see that the vortex lattice spacing is determined by the magnetic induction via $a_0 = (4/3)^{1/4}(\Phi_0/B)^{1/2}$.

At low fields, the system enters into the perfectly diamagnetic Meissner state with no equilibrium vortices present. The Meissner state phase boundary, $H_{c1}(T)$, is determined by the field at which the nucleation of a single vortex line in the superconductor becomes energetically favorable. It is given by

$$H_{c1} = \frac{\Phi_0}{2\pi\lambda^2} \ln(\kappa). \quad (1.9)$$

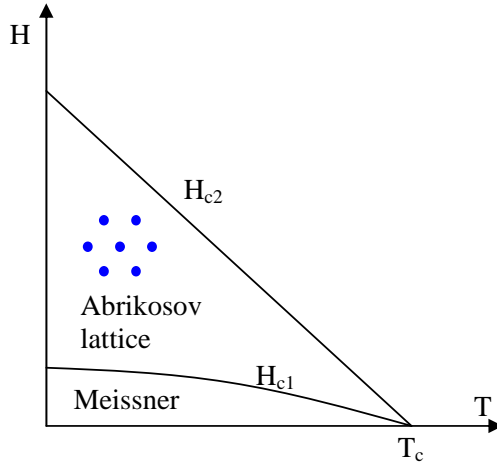


Figure 1.1: The $H - T$ phase diagram corresponding to Abrikosov's solution of the mixed state problem. At low fields the superconductor is in the perfectly diamagnetic Meissner state. At fields higher than H_{c1} it enters the mixed state, with periodic a vortex lattice (shown is an example of hexagonal arrangement of vortices). At even higher fields, H_{c2} , superconductivity is destroyed by the magnetic field.

The $H - T$ phase diagram corresponding to Abrikosov's solution of the mixed state problem is shown in Fig. 1.1.

1.4 The H_{c2} transition

The transition between the normal and the mixed state in the mean field Abrikosov solution is second order. The free energy density can be calculated and the result reads

$$f = \frac{B^2}{8\pi} - \frac{(H_{c2} - B)^2}{1 + \zeta} \quad (1.10)$$

with $B = H(1 + 1/\zeta) - H_{c2}/\zeta$. Here $\zeta = \beta_A(2\kappa^2 - 1)$ and for a triangular lattice $\beta_A = 1.16$. It is easily verified that f drops continuously to zero as the upper critical field is approached from below. Thermodynamic quantities such as the magnetization and entropy are continuous across H_{c2} , and second order derivatives, e.g. the specific heat coefficient show a discontinuity.

A general principle put forth by Landau suggests that phase transitions between a

state of a continuous symmetry and a state of discrete symmetry will be of first order [9]. Thus, the transition between the spatially homogeneous normal state and the Abrikosov lattice, displaying discrete translational symmetry, would be first order. Yet, Abrikosov's mean field solution predicts a continuous transition. To resolve this issue, one has to consider the effect of thermal fluctuations on the nature of the phase transition. It was pointed out by Halperin, Lubensky, and Ma [10] that if fluctuations in the local magnetic field inside the superconductor are traced out of the partition function, the transition from the normal state to the mixed state turns out to be *weakly* first order. An alternative program was followed by Brézin, Nelson, and Thiaville [11], who followed a $6-\epsilon$ renormalization group analysis, of a generalized 6-dimensional Ginzburg-Landau free energy. From the behavior of the RG-flows, they concluded that the free energy becomes unbounded and negative, and thus the Abrikosov transition is driven first order below 6 dimensions².

Phenomenological treatments predicting melting of the flux lattice below the mean field upper critical field have been performed [12]. These start from a treatment of the vortex lattice as an elastic medium, with known elastic moduli calculated in mean field theory. The mean square displacement of the vortex lines is then determined. The melting criterion is that the mean square displacement be a fraction of the vortex lattice spacing, as in the Lindemann criterion for the melting of atomic solids. This melting transition would be expected to be of first order. Yet, no fundamental understanding of the mechanism driving it, or whether it would indeed be first order can be obtained from this treatment.

The conclusion that fluctuations drive the Abrikosov transition first order has become more concrete by perturbative calculations of fluctuation effects on the free energy. These approach the transition from the high and low temperature sides.

²In this work the lowest Landau level treatment, which we discuss shortly, was actually followed.

The starting points are a high temperature “liquid” phase, and the low temperature Abrikosov “crystal” solution. On the high temperature side one includes order parameter fluctuations by using the linearized form of the Ginzburg-Landau equation, Eq. 1.2. This leads to lowest Landau level orbital solutions, which only include one degree of freedom, along z . Thus, the nature of the order parameter fluctuations near the upper critical field is one-dimensional in nature. The LLL solutions for ψ diagonalize the quadratic part of the free energy. One takes advantage of this by writing

$$\psi = \sum_{\lambda} a_{\lambda} \phi_{\lambda}, \quad (1.11)$$

where ϕ_{λ} are Lowest Landau Level functions. Using this expansion, the partition function

$$e^{-\tilde{F}/k_B T} = Z = \int D[\psi] e^{-F[\psi]/k_B T} \quad (1.12)$$

can be handled more easily. The quartic term in the free energy is then included perturbatively. Several efforts have been performed to extend the perturbation expansion below the mean field H_{c2} , for example by Thouless [13], Thouless and Ruggeri [14], and more recently by Li and Rosenstein [15]. Order parameter fluctuations lead to the so-called “lowest Landau level” scaling behavior, expected to dominate the thermodynamic quantities in the neighborhood of H_{c2} , at high magnetic fields. This is in agreement with experiment, for example in Nb, YBCO, and Nb₃Sn the specific heat curves have been found to display broadening of the transition discontinuity at high fields, as well as a local peak located slightly below the mean field H_{c2} , in agreement with LLL scaling [16, 17, 18].

On the low temperature side of H_{c2} , the perturbative treatment of fluctuations is most easily performed around Abrikosov’s solution [19, 20]. The starting point for these, is an expansion around the Abrikosov solution

$$\psi = \Psi_A + \int d^3 k \phi_{\mathbf{k}} f(\mathbf{k}), \quad (1.13)$$

where $\phi_{\mathbf{k}}$ are appropriate functions and $f(\mathbf{k})$ expansion coefficients. The free energy is then calculated perturbatively in f . The range of applicability of this method was recently expanded to high temperatures , where the Abrikosov solution seems to end at a spinodal point [15]. In the same work, the LLL expansion of the liquid state, was carried on to arbitrarily low temperatures.

The emerging picture reaffirms early arguments for a weakly first order crystallization of the Abrikosov flux lattice. Experimentally determined values of the melting temperature and the latent heat of the transition, measured in YBCO and Nb₃Sn, agree with the theoretical predictions [17, 15]. Usually, the experimentally determined latent heat is used to derive the entropy discontinuity at melting. For YBCO this is in the neighborhood of $1.5 k_B/\text{vortex/superconducting layer}$ at low temperatures [21]. As the temperature is increased the melting transition occurs at lower field and the entropy discontinuity decreases toward zero [21]. In Nb₃Sn, a recent report of latent heat at the melting transition gave a value of $0.3 k_B/\text{vortex}/\xi$ for the entropy discontinuity [18].

The zero field superconducting transition is in the 3d-XY universality class, as expected for a phase transition with complex order parameter that can carry topological defects. As the field is increased, the scaling behavior is expected to cross-over to LLL scaling. There has been controversy as to whether 3d-XY scaling persists up to high fields, of the order of a few Tesla for YBCO, or whether the LLL behavior is more relevant [22, 23, 24, 25, 26]. Moreover, it still remains open whether the crossover from 3d-XY to LLL scaling behavior as the field is increased, is anyhow related to the appearance, at high fields, of a “peak-effect” anomaly in critical current.

1.5 The pinning problem

The discussion so far was concerned with an ideal type-II superconductor. Most materials of practical interest show imperfections such as impurities, lattice defects, grain boundaries, and twin planes. In this work we will be interested in the effects of weak point pinning, such as that induced by impurities and local defects in the atomic lattice. This problem can be elegantly treated within the language of Ginzburg Landau theory. The treatment, due to Larkin [27], allows for local variations by $\alpha_1(\mathbf{r})$, $m_1^*(\mathbf{r})$ in the free energy coefficients α and m^* of Eq. 1.1. With these variations, one has $\alpha + \alpha_1(\mathbf{r})$ and $m^* + m_1^*(\mathbf{r})$. These local variations average to zero and have short range of spatial correlations, of order ξ . These two sources of pinning correspond to local variations in T_c and in the electronic mean free path. They are referred to as δT_c and δl pinning respectively.

With these sources of pinning the part of the free energy due to pinning can be separated out. To first order in the variations

$$\delta F_1 = \int \alpha_1 |\psi|^2 - \frac{m_1^*}{2m^{*2}} \left| \left(\frac{\hbar}{i} \nabla - \frac{e}{c} \mathbf{A} \right) \psi \right|^2 d^3 r \quad (1.14)$$

(here we suppressed the spatial dependence of α_1 , m_1^*). The result of pinning on the Abrikosov lattice is that deformations are induced, causing displacement of the vortex core positions by $\mathbf{u}(\mathbf{r})$ from their ideal equilibrium positions. The change in free energy of the deformed lattice contains an elastic contribution, as well as a pinning term. The latter can be expressed as

$$\delta F_{pin} = \int \mathbf{u}(\mathbf{r}) \cdot \nabla \left(\alpha_1 |\psi|^2 - \frac{m_1^*}{2m^{*2}} \left| \left(\frac{\hbar}{i} \nabla - \frac{e}{c} \mathbf{A} \right) \psi \right|^2 \right) d^3 r \quad (1.15)$$

$$\equiv \int \mathbf{u}(\mathbf{r}) \cdot \mathbf{f}_{pin}(\mathbf{r}) d^3 r . \quad (1.16)$$

The pinning energy competes with the elastic energy arising from the displacement

field. It was shown by Larkin that within this treatment, pinning results in a displacement field which grows as a power law for large distances

$$\overline{[\mathbf{u}(\mathbf{R}) - \mathbf{u}(0)]^2} \sim |\mathbf{R}|, \quad (1.17)$$

with the overbar $\overline{(.)}$ denoting average over disorder. The main significance of this result is that arbitrarily weak pinning destroys the translational long-range order of the Abrikosov lattice.

There exists a general scaling argument according to which long range order of an elastic medium is always destroyed by arbitrarily weak point pinning in less than $d_c = 4$ dimensions [28]: In the presence of pinning, relative elastic distortions of order a will be induced inside a volume $V \sim R^d$, where d denotes the dimensionality. Since individual pinning sites act in a random fashion, the typical pinning energy gain on the volume V will scale as the average pinning energy (ϵ_{pin}), times the square root of the number (N) of pinning sites in it: $\epsilon_{pin}\sqrt{N} = \epsilon_{pin}\sqrt{nV}$, with n the average density of pinning sites. The average pinning energy is then of order $\epsilon_{pin}n^{1/2}R^{d/2}$. This energy gain will be balanced against an elastic energy cost of order $\frac{1}{2}c a^2 R^{d-2}$, with c some elastic modulus. For $d > 4$ the net energy gain yields a minimum at some finite R indicating that only local elastic distortions will occur. In dimensions less than four, the pinning energy dominates at large distances. In this case, the energy gain will be minimized at $R \rightarrow \infty$, indicating that the elastic distortions will extend over the entire size of the physical system, destroying long range order. This general result is known as the Imry-Ma argument.

This mechanism offers the basis for the Larkin and Ovchinnikov collective pinning model [29], usually formulated for the $d = 3$ case. The relative displacement field within a volume V will increase as V increases. If the volume is small enough that the relative displacement field within it is less than the range of the pinning forces of the order of ξ , then the vortex lattice over this volume, V_c , is expected to be

collectively pinned. The vortex lattice in this “correlation volume” experiences an average pinning force. The individual pinning forces act over a range of order ξ before changing randomly. Thus the average energy density gain due to the pinning forces will be of order $\xi f_{pin} n^{1/2} V_c^{-1/2}$, where f_{pin} is the average pinning force. The elastic energy cost will result from shear and tilt deformations of the vortex lattice.

The net energy-density change due to the distortion will be of order

$$\delta F = \frac{1}{2} C_{66} \left(\frac{\xi}{R_c} \right)^2 + \frac{1}{2} C_{44} \left(\frac{\xi}{L_c} \right)^2 - \xi f_{pin} \frac{n^{1/2}}{V_c^{1/2}}, \quad (1.18)$$

where the “correlation volume” is $V_c = R_c^2 L_c$. L_c is the longitudinal dimension of V_c in the direction of the applied field and R_c in the transverse direction. The above expression yields maximum gain in energy density for

$$L_c = \frac{2C_{44}C_{66}\xi^2}{nf_{pin}^2}, \quad R_c = \frac{2^{1/2}C_{44}^{1/2}C_{66}^{3/2}\xi^2}{nf_{pin}^2}. \quad (1.19)$$

In the context of Larkin’s result and the Imry-Ma argument this was interpreted as implying some sort of fracturing of the vortex lattice into “Larkin domains” of size of the order L_c and R_c . As a result the mixed state in any realistic system was not expected to posses translational long-range order. Moreover, as we will discuss in the next section, the mixed state was not expected to be truly superconducting³ either. Thus, the question of the nature of the H_{c2} transition in any realistic system with disorder was somewhat of a moot point. The mixed state seemed to maintain the symmetries of the normal state and no phase transition would be justified to exist in the presence of disorder.

On the experimental front, however, the facts suggested that things might not be quite so simple. Decoration experiments had revealed large flux-lattice areas with a high degree of order and virtually no flux-lattice defects [30]. Neutron diffraction experiments had revealed flux line lattices with sharp, resolution limited, Bragg peaks

³Meaning it would not support persistent supercurrents.

[31, 32]. The existence of long-range order on high-quality superconducting samples was an experimental fact. A decisive ingredient was missing from the theoretical treatment of pinning.

This situation changed after careful reconsideration of the pinning summation problem. We can qualitatively understand how the pinning-force summation in the above treatments leads to an overestimate of the effect of pinning: As the vortex lattice wanders away from the undistorted configuration, the elastic energy cost increases boundlessly with increasing displacement field. On the other hand, once the vortex lattice has wandered by one flux lattice spacing, $u \simeq a_0$, it experiences the same pinning potential, due to its periodicity. Thus, collective-pinning type models tend to overestimate the long wavelength effect of pinning on the vortex lattice. A correct treatment has to take into account the coupling of the flux lattice periodicity to the random pinning potential.

This was performed by Nattermann [33] and later by Giamarchi and LeDoussal [34]. In those treatments it is found that at large distances, the displacement field grows logarithmically, instead of the power law in Eq. 1.17

$$\overline{\langle (\mathbf{u}(\mathbf{R}) - \mathbf{u}(0))^2 \rangle} \sim \log |\mathbf{R}| . \quad (1.20)$$

At the shortest length scales the behavior is still collective-pinning like. This is the so-called Larkin regime, where $\langle u(R)^2 \rangle \sim R$. At the scale on which $u(R) \simeq a_0$ the behavior crosses over to the so-called random manifold regime with different roughness exponent $\langle u(R)^2 \rangle \sim R^{2\nu}$, $2\nu \simeq 1/6$ [35]. The random manifold regime covers intermediate length-scales.

The significance of the result of Eq. 1.20 is that quasi long-range order survives in the pinned vortex lattice. To be more specific, the vortex lattice displays *topological* order, not allowing for the presence of unbound dislocations. This new state of matter has been termed a “Bragg Glass” phase, due to the fact that it displays power

law singularities of the structure factor $S(q) \sim 1/q^{3-A}$, $A \simeq 1$. This implies that the diffraction patterns in neutron scattering experiments will yield sharp, resolution limited, Bragg peaks. The existence of resolution limited Bragg peaks from a flux line lattice was confirmed in a neutron diffraction study [36]. The measured intensities were also consistent with the expectations for the Bragg Glass phase.

In addition to topological quasi long range order, the Bragg Glass is an elastic medium with finite long-wavelength shear elasticity. Thus it possesses the properties which characterize solid media. A very significant consequence of the existence of the Bragg Glass phase is that the phase transition between the normal state and the mixed state survives in the presence of disorder. The symmetry-breaking Abrikosov transition of an ultra-clean system, discussed in the previous section, transforms into the Bragg Glass transition under the influence of atomic lattice defects and impurities. The long-range order of the Abrikosov lattice is replaced by the topological quasi long-range order of Bragg Glass. Under this new light, the formerly uninteresting question of the formation of a vortex lattice in a realistic, disordered system, acquired fundamental importance as an example of a phase transition in the presence of quenched disorder.

1.6 Transport and critical currents

We now turn to the dynamical properties of vortex lattices. In an ideal superconductor, the mixed state shows linear resistivity and dissipation under a passing current. The reason for this is that vortices experience a Lorentz force in the presence of a current density \mathbf{j}

$$\mathbf{f} = \mathbf{j} \times \mathbf{n}\Phi_0/c, \quad (1.21)$$

where \mathbf{n} is in the direction of the local magnetic field. The Lorentz force will be balanced by pinning forces when the current density is not too high. For currents

higher than the critical current, j_c , vortices get depinned and flow through the sample. In this process, they experience a viscous force, \mathbf{f}_v , proportional to their velocity, \mathbf{v} . This is $\mathbf{f}_v = -\eta \mathbf{v}$. As a result an electric field is induced in the direction of the current

$$\mathbf{E} = \mathbf{B} \times \mathbf{v}/c. \quad (1.22)$$

This means that vortex flux flow leads to the appearance of electrical resistivity

$$\rho_{ff} = B \frac{\Phi_0}{\eta c^2}. \quad (1.23)$$

Obviously, an ideal superconductor in the mixed state is not *truly superconducting*, in the sense that it shows linear resistivity. The viscosity associated with vortex motion can be estimated. A simplified calculation of Bardeen and Stephen [37] treats the core as a normal region of radius $a \approx \xi$. Dissipation occurs in the core due to quasiparticles and an equal contribution arises from outside the core. The result is $\eta \approx \Phi_0 H_{c2}/\rho_n c^2$, with ρ_n the normal state resistivity. As a result, the flux flow resistivity in this model is given by

$$\rho_{ff} \approx \rho_n B/H_{c2}. \quad (1.24)$$

In the presence of pinning sites, vortex flow is obstructed. Vortices tend to get pinned onto atomic lattice defects. If the Lorentz force is balanced by the pinning force, vortex flow will stall and as a result the superconductor can carry a persistent supercurrent. This will be the case as long as the Lorentz force is smaller than the pinning force. Once this condition is reversed, resistive flux flow appears. The current for which the balance is reversed is the critical current, j_c .

This situation results in the “Bean critical state” model [38, 39]. This model deals with the local magnetic field profile inside a superconducting sample. A gradient in the local field will result in a current density proportional to the gradient, $\nabla \mathbf{H}(\mathbf{r})$. The situation most commonly discussed is that of a cylindrical superconductor in the presence of an increasing magnetic field. A screening supercurrent opposing the field

increase is induced inside the superconductor, flowing in the azimuthal direction. As a result, a magnetic field gradient appears along the radial direction. It is determined by the critical current

$$j_c = \frac{4\pi}{c} \frac{dH}{dr}. \quad (1.25)$$

We will use this basic model to discuss flux changes in the presence of field ramps in the next chapter.

The above discussion of vortex pinning has neglected the rather serious effect of thermal fluctuations. The Bean state is not an equilibrium state: The field profile will decay in time due to thermally activated depinning of vortices. This process of thermally activated flux creep restores the linear dc resistivity associated with flux flow, albeit with a much smaller magnitude. Nevertheless, in this model superconductors are still *not* superconducting.

The concept of thermally assisted flux creep originated in the treatment of Anderson and Kim [40, 41]. In this model, vortex bundles of typical size L behave as individual entities, hopping between pinning sites due to thermal activation. The typical size of a bundle hop is taken to be of order L . The rate of these events will be determined as usual by

$$r_0 = f_0 e^{-F_0/k_B T}, \quad (1.26)$$

with f_0 some attempt frequency and F_0 the free energy barrier for the process. The hopping rate in this case is the same for all directions. In the presence of a current, the free energy barrier becomes asymmetric. The pinning force density is balanced by the Lorenz force density for the bundle, $\Xi \equiv jB/c$, and during a jump the Lorentz force performs work equal to ΞL^4 . As a result, the free energy barrier in the direction of the Lorentz force is lowered, while the one in the opposite direction is increased.

The net hopping rate in the direction of the Lorentz force now is

$$r = r_+ - r_- = f_0 e^{-F_0/k_B T} \left(e^{\Xi L^4/k_B T} - e^{-\Xi L^4/k_B T} \right) \quad (1.27)$$

$$= 2r_0 \sinh \left(\frac{jBL^4}{ck_B T} \right). \quad (1.28)$$

As a result, flux creep velocity $v \approx Lr$, and electric field $E \approx Bv/c$ develop. In the limit of zero current, the induced electric field due to creep is

$$E \approx \frac{2B^2 r_0 L^4}{c^2 k_B T} j. \quad (1.29)$$

The superconductor displays linear dc resistivity at all finite temperatures.

This behavior can be contrasted with that in the Meissner state, where the superconductor shows vanishing linear resistivity in the limit of zero current. In this case a dissipative voltage will appear at finite temperatures through nucleation and growth of vortex loops induced by the passing current. This is known as the “droplet model”, first proposed for vortices in superfluid helium, in conceptual analogy to droplet nucleation from supersaturated vapor [42]. The free energy barrier for a vortex loop lying in the plane normal to the current density is determined by the balance between the energy cost due to the vortex line energy, $\epsilon_1 \approx (\Phi_0/4\pi\lambda)^2 \ln(\kappa)$, and the work done by the Lorentz force in increasing the size of the loop. The latter is

$$\int_0^R 2\pi r \frac{j\Phi_0}{c} dr = j \frac{\Phi_0}{c} \pi R^2. \quad (1.30)$$

The energy cost of the loop is, then

$$\Delta F \approx 2\pi R \epsilon_1 - j \frac{\Phi_0}{c} \pi R^2, \quad (1.31)$$

which yields an energy barrier $\Delta F_0 \approx \pi c \epsilon_1^2 / j \Phi_0$. Every event of nucleation and growth of a vortex loop leads to a phase slip by 2π of the phase of the superconducting order parameter. This increases the free energy of the superconductor via the kinetic energy term in Eq. 1.1. To estimate the net rate of loop nucleation events, one has to take

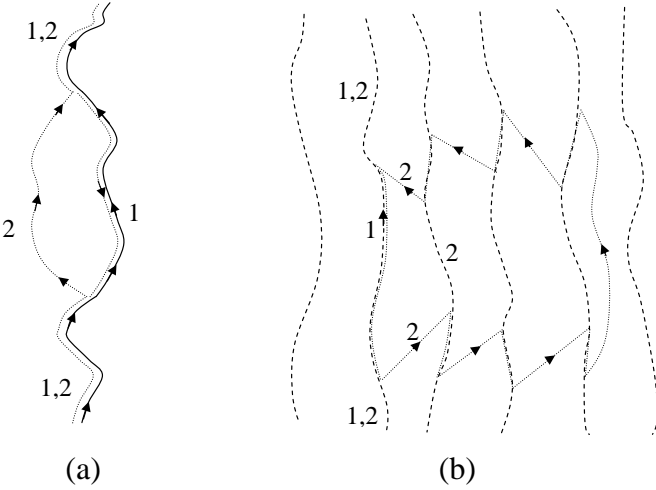


Figure 1.2: (a) Loop excitation in an isolated vortex line. The directions of the arrows are in the sense of the flux of the vortex segments. The vortex line shifts from configuration “1” to configuration “2”. (b) Loop excitation involving multiple vortex lines. These schematics are adapted from Fisher, Fisher, and Huse [1].

into account the free energy difference induced by the phase slips and the result is [43]

$$r_l = f'_0 e^{-\Delta F_0/k_B T} \sinh \left(\frac{\hbar j}{4\pi e k_B T} \right), \quad (1.32)$$

with f'_0 some attempt frequency (not to be confused with the one entering the flux creep analysis). This leads to the appearance of a voltage difference in the direction of the current

$$V = \frac{h}{2e} f'_0 e^{-\Delta F_0/k_B T} \sinh \left(\frac{\hbar j}{4\pi e k_B T} \right), \quad (1.33)$$

Evidently, the resistivity in the limit of zero current in this case is

$$\rho = \frac{E}{j} \sim e^{-\Delta F_0/k_B T} = e^{-j_T/j}, \quad (1.34)$$

with the definition $j_T \equiv \pi c \epsilon_1^2 / \Phi_0 k_B T$. Clearly, non-linear resistivity dominates the response in the Meissner state in the limit of zero driving current, in contrast to the situations obtained in both the flux-flow and flux-creep regimes.

Some 16 years ago, a significant and intriguing question was raised by Fisher, Fisher, and Huse, concerning the effect of pinning on the superconducting properties

of the mixed state [1]. They raised the question of whether phase coherence of the superfluid order parameter can survive in the presence of weak point pinning. In this case, a modified version of the droplet model would apply to the mixed state. A current flowing perpendicular to the vortices, would tend to push the weakest pinned vortex segments sideways. If a length of size L_{\parallel} parallel to the applied field is displaced perpendicularly by L_{\perp} , the scaling relation

$$L_{\perp} \sim L_{\parallel}^{\zeta} \quad (1.35)$$

is expected to hold. The displaced vortex line can be thought of as a superposition of the initial vortex line and a counter circulating vortex loop, as shown in Fig.1.2a. The free energy cost of the vortex loop is expected to scale as

$$F(L_{\perp}) \approx \Upsilon L_{\perp}^{\theta_{\perp}}. \quad (1.36)$$

In addition, the energy barrier between the initial and final configurations will be larger than $F(L_{\perp})$. It will be given by

$$B(L_{\perp}) \sim L_{\perp}^{\psi_{\perp}}, \quad (1.37)$$

with $\psi_{\perp} > \theta_{\perp}$. In the presence of a current density j , the energy barrier can be overcome, for large L_{\perp} , by the energy gained due to the work done by the Lorentz force, which scales as $L_{\parallel} L_{\perp}$

$$W(L_{\perp}) \sim j L_{\perp}^{(1+1/\zeta)}. \quad (1.38)$$

As a result, thermally activated flux loops will cause dissipative phase slips (vortex line displacements) and the resistivity in the mixed state is expected to scale as

$$\rho_{vg} \sim e^{-(j_T/j)^{\mu}}. \quad (1.39)$$

This property can be extended to loops extending over multiple vortices, as shown schematically in Fig. 1.2b. Thus, the superconducting mixed state has vanishingly small linear resistivity.

This pinned superconducting state is a thermodynamic phase distinct from the normal (or vortex liquid) phase since it possesses long-range phase coherence of the superconducting phase. Phase coherence is the key element to the vanishing of linear resistivity, since it allows the unbounded scaling of the free energies of the vortex loop excitations as $L \rightarrow \infty$. This phase can be translationally disordered and it has been termed vortex glass, in analogy with certain spin glass models [1].

The scaling of resistivity predicted by the vortex glass model can be tested experimentally. In practice, one measures $I - V$ curves. A scaling behavior of the form

$$\frac{V}{I} = \xi_{vg}^{(d-2-z)} \vartheta_{\pm}(I\xi_{vg}^{d-1}/T), \quad (1.40)$$

is expected. Here $\xi_{vg} \sim |(T - T_g)/T_g|^{-\nu}$ is the vortex glass correlation length, z the dynamic scaling exponent, and $\vartheta_{\pm}(x)$ a scaling function above (+) and below (-) the glass transition temperature T_g . In the limit $x \rightarrow 0$, the scaling function ϑ_+ above the glass transition approaches a constant, and the function ϑ_- below T_g a power law. This type of scaling has been extensively reported starting with the work of Koch *et al.* [44]. Nevertheless, the reported scaling is not unique, and seems inconclusive [45]. Moreover, simulation work on the actual existence of a thermodynamically stable phase-coherent vortex glass phase is inconclusive [46, 47].

1.7 The Peak Effect

The critical current density of a superconductor in the mixed state normally decreases as the magnetic field or temperature are increased. The peak effect is an “anomalous” increase in the critical current density with increasing magnetic field or temperature, which occurs in the neighborhood of the upper critical field. A schematic of the peak effect in j_c and the nomenclature used for its various features is shown in Fig. 1.3. The peak effect was discovered in 1960 [48] and has since been observed in numerous

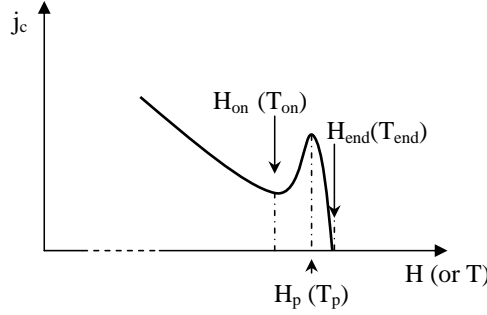


Figure 1.3: Peak effect in critical current, versus applied field or temperature. We mark the onset H_{on} or T_{on} , the peak H_p or T_p , and the end H_{end} or T_{end} of the peak effect. The upper critical field (H_{c2} or T_{c2}) can be higher than the end of the peak effect.

conventional superconducting alloys [49], superconducting elements and compounds, e.g. Nb [50], 2H-NbSe₂ [51], MgB₂ [52], amorphous Nb₃Ge films [53], and high- T_c compounds [54].

The peak effect was explained in the early days by a mechanism proposed by Pippard [55]. In this model, the vortex lattice in the presence of the pinning potential adjusts to the pinning sites. A soft lattice will adjust better to the pinning sites, and will thus be pinned more strongly than a hard lattice. Close to H_{c2} the vortex lattice softens, causing the increase in critical current. Eventually, as the upper critical field is further approached, the strength of pinning sites decreases due to the decreasing superconducting condensation energy and the critical current also vanishes.

The Pippard mechanism can be put into quantitative terms based on the collective pinning model discussed earlier [29]. The critical current in this model is determined by balancing the Lorentz force against the pinning force that a correlation volume $V_c = L_c R_c^2$ feels. In the notation of Eqs. 1.18, 1.19 one gets

$$j_c = \frac{c}{B} \frac{(n f_{pin}^2)^{1/2}}{V_c^{1/2}}. \quad (1.41)$$

Earlier, in Eqs. 1.19, we obtained the values for L_c and R_c . From these we see that $V_c \propto C_{44}^2 C_{66}^4$. Clearly, softening of either of the elastic constants will result in an

increase of the critical current. As H_{c2} is approached, the shear modulus vanishes quadratically in the distance from the mean field transition temperature. Thus, a peak effect with the so-called C_{66} mechanism is obtained. Alternatively, a softening of the tilt modulus for short wavelength distortions could—in principle—lead to a peak effect via the so-called “ C_{44} mechanism”.

This point of view that treats the peak effect as local disordering of the vortex lattice has been used for the interpretation of a wide variety of experiments [53, 56]. Nevertheless, collective-pinning type models do not offer any insight into the mechanism driving the peak effect. In the light of recent understanding of the effects of pinning and thermal fluctuations, which result in various different vortex phases, the relation of the peak effect with a phase transition in vortex matter has become a tempting scenario. In this modern context, one would expect the peak effect to be related to a disordering phase transition of the vortex lattice, between an ordered, low critical current phase and a disordered, high critical current one.

Substantial experimental effort has been put into transport measurements in 2H-NbSe₂. In these one can distinguish between regimes of elastic flux flow below the peak of the peak effect at T_p and plastic flux flow above T_p [51, 57], indicating loss of rigidity of the flux lattice above T_p . In additional work in 2H-NbSe₂, the metastability between a high j_c disordered state above the peak effect and a low j_c ordered state below it was studied [58]. This work provided further support to viewing the peak effect as an order-disorder transition. The observed behavior included current-induced annealing between the ordered and a disordered lattices, and glassy relaxation of the critical current. As a result of this work, “peak-effect phase diagrams” in which the peak effect is taken to designate the limit between ordered and disordered vortex lattices have become common. A typical example of such a phase diagram is schematically presented in Fig. 1.4.

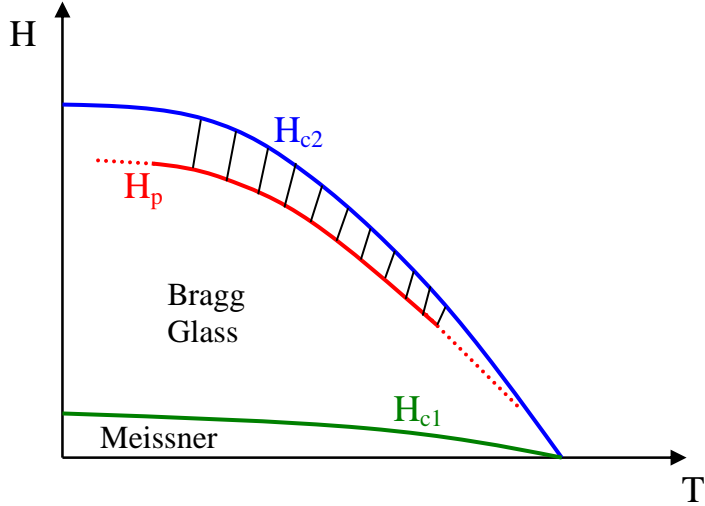


Figure 1.4: Schematic of a typical peak-effect phase diagram, found in conventional superconductors. The peak effect line separates an ordered Bragg Glass phase at low temperature from a disordered phase at high temperatures. The nature of the high-temperature disordered phase is unresolved. The peak effect line might [2] or might not [3] terminate on the upper critical field line, H_{c2} .

The distinction between the “ordered” and “disordered” lattices became more robust in later transport work which reported hysteretic resistivity curves between the onset and the peak of the peak effect, at low currents [59]. In that work it was proposed that the ordered phase below the onset of the peak effect could be the topologically ordered Bragg Glass phase. Decisive structural evidence on establishing the relation of the peak effect to an order disorder transition was provided by neutron diffraction studies in Nb [4]. These revealed an orientationally and translationally disordered state above T_p , and a sixfold symmetric and translationally ordered state below it. Metastability, i.e. superheating of the ordered state and supercooling of the disordered state were found to occur around the peak effect. The state obtained below the peak effect boundary is now universally interpreted as the Bragg Glass phase. The nature of the disordered phase obtained above T_p , i.e. whether it is some sort of vortex glass or a vortex liquid, is still unresolved.

Additional evidence indicative of a phase transition at the peak effect in YBCO

came from magnetization measurements, revealing the presence of a magnetization jump at the peak of the peak effect [60, 61]. More recent calorimetric measurements reported the presence of latent heat in the peak effect in Nb₃Sn. This is found to occur at the melting temperature expected for a clean (zero pinning) system. It is unclear at this point whether the latent heat in these latter measurements arises from the peak effect or from melting of the “floated” vortex crystal, established in those measurements by shaking the vortex lattice with an ac field.

Further insight was provided by imaging studies using Hall probe microscopy in 2H-NbSe₂ [62]. In these it was found that ordered (low j_c) and disordered (high j_c) phases coexist in a large region below the peak-effect phase boundary. Above the peak effect, the flux lattice was found to be dominated by the disordered phase. Thus phase coexistence is thought to be the reason for the observed metastability in transport and neutron diffraction. A recent transport study, again in 2H-NbSe₂, determined the spinodal point above which superheating of the Bragg Glass phase is not possible even in a metastable manner [63].

Although the ordered phase below the peak effect is accepted to be a Bragg Glass, the nature of the phase between the onset and the peak, as well as of that above the peak of the peak effect have not been resolved. A scanning tunneling microscope study of static vortex latices in the peak effect region in 2H-NbSe₂ revealed a loss of vortex motion correlations above the onset of the peak effect [64]. This was argued to indicate a drop in shear elasticity of the vortex lattice in that region. On the other hand, transport measurements in 2H-NbSe₂ using the so-called Corbino geometry to minimize sample-surface induced disordering, indicated that the high j_c disordered phase becomes stable above the peak of the peak effect and is only dynamically injected from the sample surfaces in the region between the onset and the peak. Uncovering the subtle nature of the phases between T_{on} and T_p and between T_p and

T_{c2} is necessary for any attempt to propose a realistic mechanism of the peak effect.

The question of what different vortex phases are involved in the peak effect can be attacked from a thermodynamical point of view, by determining general features of generic $H - T$ peak effect phase diagrams. In recent years peak effect phase diagrams have been measured for various materials [52, 2, 65]. A notable common feature in many of these is the disappearance of the peak effect at low fields, where the peak effect line intersects the upper critical field line. This has raised the question of a multicritical point associated with the disappearance of the peak effect. This question is closely tied to that of the nature of the disordered phase above the peak of the peak effect.

1.8 Overview

This brief overview of the subject of vortex physics has but touched on the multiple different aspects of the field. Several series of experiments and theoretical ideas have been omitted. Even among the topics discussed, few selected works were mentioned. Emphasis was given on topics that are closely related to the issues we will discuss in the subsequent chapters and on issues that potentially have a deep impact on our understanding of superconductivity, such as the Bragg Glass and vortex glass proposals. In the following chapter, we introduce the experimental techniques used in this work. We then proceed to present the new experimental findings. In Chapter 3 we present magnetocaloric measurements on a niobium single crystal which displays the peak effect. From these we obtained better understanding of the peak-effect phase diagram in niobium. In Chapter 4 we present neutron diffraction measurements of flux-lattice translational correlations in the direction of the magnetic field. They were performed on the same niobium crystal studied in Chapter 3, and focused on the behavior in the neighborhood of the peak effect. These measurements allow us

to look into the process of Bragg Glass crystallization. This thesis closes with a concluding chapter, in which the picture of our combined findings is synthesized.

Chapter 2

Experimental Techniques

2.1 Introduction

Before proceeding to present our experimental results in later chapters, we offer an overview of the experimental techniques used. The sample used in our experiments was a niobium single crystal displaying the peak effect anomaly in critical current. It had previously been studied using ac-susceptometry and Small Angle Neutron Scattering (SANS) [4, 2]. This sample was studied in the present work using calorimetry, magnetocalorimetry, ac-susceptometry, and SANS.

Calorimetric measurements could, in principle, reveal a specific heat signature in the neighborhood of the peak effect. Schematically, a sharp specific-heat peak would be expected to arise from the entropy discontinuity, equivalently the latent heat, at a first order transition underlying the peak effect. As already mentioned, such an effect was observed in high sensitivity calorimetric measurements at the vortex lattice melting transition in $\text{YBa}_2\text{Cu}_3\text{O}_{7-\delta}$ [17] and at the peak effect in Nb_3Sn [18]. The magnitude of the entropy discontinuity will be of great significance to understanding the nature of the phase transition, since it is a measure of the degrees of freedom involved in the phase transition, on basis of the equipartition principle.

The less common magnetocaloric measurements probe the magnetocaloric coefficient. This is defined as $M_T = T (dM/dT)_H$. In a metal this is negligible, whereas in the superconducting mixed state it is nonzero. The magnetocaloric measurements are sensitive to presence of vortices in the sample, as well as the amount of vortex flux-flow into, or out of, the sample.

Magnetic ac-susceptibility measurements offer a sensitive and easily implemented way to probe vortex dynamics. They have proved to be useful in identification of the peak-effect [54] and are widely used for this purpose. We used χ' ac-susceptibility measurements as a supplement to our magnetocaloric measurements, in order to compare the manifestation of the peak effect in the two.

The low temperature calorimetric, magnetocaloric, and ac-susceptibility measurements were performed in an Oxford flowing-gas cryostat/superconducting magnet with accessible temperatures in the 2.2-300 K range and maximum accessible field of 7 T.

SANS is a uniquely powerful tool for bulk structural studies of vortex matter in the mixed state [31, 32]. Much like X-ray diffraction from atomic matter, it can reveal the presence of ordered or disordered flux line lattices, quantify the amount of orientational and translational disorder, and distinguish between Abrikosov flux lattices of different symmetry. In this work, we present SANS rocking-curve measurements in the peak effect region. These measure the translational correlations of the flux lines in the longitudinal, parallel to the applied field, direction.

2.2 Calorimetric measurements

2.2.1 Principle of relaxation calorimetry

In calorimetry, careful regulation of the heat exchange between the sample and calorimeter is crucial. All variants of calorimetric measurements are performed by monitoring the net heat input, or output, to a sample and the resulting temperature changes¹. Different techniques are appropriate for different samples, mainly depending on the sample size and the required measurement accuracy [66]. The technique implemented in this work was the so-called “relaxation” technique. The relaxation technique, offers the advantage of recording actual heat capacity values of the sample under study, rather than heat capacity changes. This allows the measurement of important sample properties such as the Debye temperature (Θ_D) of a crystalline solid and the electronic specific heat coefficient (γ). The shortcomings of this technique are that it does not offer the highest resolution or density of data points compared to other approaches.

We describe the principle of the technique and the technical issues involved in extracting the specific heat of a sample and the heat link differential conductance. The latter enters the magnetocaloric measurements as well. For this reason we give a detailed description of the heat-transfer processes here.

The main principle of the technique takes advantage of the fact that a system slightly offset from its static temperature under heat-flow conditions approaches the static temperature exponentially in time. The setup used has to be built with this basic principle in mind. The idealized heat flow diagram of a generic setup is shown in Fig. 2.1. At any given level of heat input, the sample reaches a steady temperature (T_0) determined by the condition that the heat input, through the heater, and output,

¹This is the case even in differential calorimetric setups where two similar samples, the one under study and a reference sample, are heated under “identical” conditions.

through the heat link, be equal

$$P_{in} = G(T_0, T_{bath}) \cdot (T_0 - T_{bath}). \quad (2.1)$$

The heat link conductance, is marked $G(T_0, T_{bath})$, since it depends on both temperatures (to fully appreciate this, the book by Pobell [67] is helpful). Henceforth, the bath temperature argument of G will be suppressed. At a slightly higher heat input $P_{in} + \Delta P_{in}$, a new static sample temperature, $T_0 + \Delta T$, is achieved

$$P_{in} + \Delta P_{in} = G(T_0 + \Delta T) \cdot (T_0 + \Delta T - T_{bath}). \quad (2.2)$$

This can be expanded to first order in the temperature change, by use of $G(T_0 + \Delta T) = G(T_0) + G'(T_0) \Delta T$, and yields

$$P_{in} + \Delta P_{in} = G(T_0) \cdot (\Delta T + T_0 - T_{bath}) + G'(T_0) \cdot \Delta T \cdot (T_0 - T_{bath}) + \mathcal{O}(\Delta T^2). \quad (2.3)$$

Subtraction of equations 2.3 and 2.1 gives, to first order in ΔT

$$\Delta P_{in} = \{G(T_0) + G'(T_0) \cdot (T_0 - T_{bath})\} \cdot \Delta T \equiv \tilde{G}(T_0) \cdot \Delta T. \quad (2.4)$$

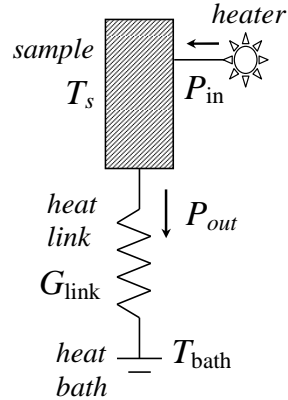


Figure 2.1: Idealized heat-flow diagram of a calorimeter used for the relaxation (heat-pulse) technique. The sample, at temperature T_s is heated by an external heater via regulated input P_{in} . It is thermally connected to the heat bath at temperature T_{bath} through a heat link of conductance G_{link} . The heat flow through the link is P_{out} .

Next, we consider a case where the sample is initially at the static temperature T_0 , corresponding to heat input P_{in} . The heat input is abruptly increased to a new value, $P_{in} + \Delta P_{in}$. Evidently, the sample temperature will increase until it reaches the static temperature satisfying Eq. 2.2. During this process, the heat input from the heater exceeds the heat flow out of the sample, through the heat link. Thus the net effect is absorption of heat from the sample, resulting in the temperature increase. The process obeys the first law of thermodynamics. Heat absorption by the sample is quantified by the heat capacity $C(T)$, where $T = T_0 + \delta T(t)$

$$\begin{aligned} C(T_0 + \delta T) \cdot \delta \dot{T} &= P_{in} + \Delta P_{in} - P_{out} \\ &= P_{in} + \Delta P_{in} - G(T_0 + \delta T) \cdot (T_0 + \delta T - T_{bath}) \end{aligned}$$

Next, we expand the left hand side and the last term on the right hand side to first order in the temperature change, δT

$$\begin{aligned} C(T_0) \cdot \delta \dot{T} &= P_{in} + \Delta P_{in} \\ &\quad - G(T_0) \cdot (T_0 - T_{bath}) - \{G(T_0) + G'(T_0) \cdot (T_0 - T_{bath})\} \cdot \delta T \\ C(T_0) \cdot \delta \dot{T} &= \tilde{G}(T_0) \cdot \Delta T - \tilde{G}(T_0) \cdot \delta T. \end{aligned}$$

The last expression above, can be rewritten as

$$\tilde{G}(T_0) \cdot (\Delta T - \delta T) = -C(T_0) \cdot \frac{d}{dt}(\Delta T - \delta T). \quad (2.5)$$

In this form, the behavior of the sample temperature in response to the applied heat step is obvious. The quantity $\Delta T - \delta T$ decays to zero exponentially. Initially (at $t = 0$) it is equal to ΔT , since the sample temperature does not change instantaneously. Thus the initial condition for the differential equation, Eq. 2.5 is

$$(\Delta T - \delta T)_{t=0} = \Delta T.$$

The solution to the differential equation for δT is

$$\delta T = \Delta T \cdot (1 - e^{-t/\tau}). \quad (2.6)$$

Here the asymptotic temperature change equals $\Delta T = \Delta P_{in}/\tilde{G}(T_0)$, and the relaxation time of the exponential is $\tau = C(T_0)/\tilde{G}(T_0)$. The situation is essentially the same for the case where one decreases the heat input by a given amount, $P_{in} - \Delta P_{in}$. Obviously, in this case the temperature is decreased exponentially, to an asymptotic value $T_0 - \Delta T$. Therefore the relaxation technique allows for calorimetric measurements on both increasing and decreasing temperatures.

In practice, one applies a known increase ΔP_{in} to the heating power, and measures the temperature response as a function of time. This is fitted with an exponential function with the fitting parameters being temperature jump, ΔT , and relaxation time τ . Once these are obtained, the effective link conductance $\tilde{G}(T_0)$, and heat capacity of the sample $C = C(T_0)$ are obtained via

$$\tilde{G}(T_0) = \Delta P_{in}/\Delta T \quad (2.7)$$

$$C(T_0) = \tilde{G}(T_0) \cdot \tau. \quad (2.8)$$

The approximations performed in the derivation of the exponential response of the sample temperature are bound to break down if the temperature steps are not small enough. In most cases, this constraint is satisfied, and a self consistency check can always be performed *a posteriori*. That is, once the link conductance and specific heat curves are obtained using Eqs. 2.7, 2.8, one can check for self consistency.

2.3 Magnetocaloric measurements

2.3.1 Basic Principle

As already mentioned the magnetocaloric coefficient is defined as $M_T = T (dM/dT)_H$.

It is a thermodynamic coefficient complementary to the specific heat $C_H = T (dS/dT)_H$.

By use of the Maxwell thermodynamic identities, one finds that $M_T = T (dS/dH)_T$.

In a metal the latter is negligible, whereas in the superconducting mixed state, the entropy becomes strongly dependent on the applied magnetic field. It is easy to see from the Abrikosov free energy of the previous chapter (*cf.* Eq. 10), that mean field theory predicts $M_T = -T \left(\frac{dH_{c2}}{dT} \right) \frac{1}{4\pi\beta_A(s\kappa^2-1)}$ in the limit $H \rightarrow H_{c2}^-$.

In studies of vortex phases in bulk superconductors, various experimental techniques provide complementary pieces of information. Combining these in a consistent picture is a non-trivial task. Magnetic ac-susceptibility measurements are sensitive to screening currents, and thus to the location of peak effect features, but are not suitable for the identification and study of the mean field H_{c2} transition itself [2]. Commercial magnetometers are not suited for study of large samples. Calorimetric [18, 68] and ultrasonic attenuation [69, 70] measurements determine the upper critical field where bulk condensation of Cooper pairs occurs, but it remains unclear under what circumstances they also provide a peak effect signature. Moreover the combination of information obtained with different techniques has to rely on thermometer calibration issues. Furthermore, the dynamical measurements suffer from thermal gradients in the studied samples. Magnetocaloric measurements overcome these difficulties because they are sensitive to both the presence of bulk superconductivity and to dynamical, flux-flow related effects. Moreover they can be performed in quasi-adiabatic conditions, where virtually no thermal gradients are present in the sample. Finally, they can be easily performed using a common calorimeter.

The magnetocaloric effect is a special case of thermomagnetic effects in the mixed state of superconductors which have long been known and investigated [71, 72]. These arise from the coexistence of the superconducting condensate which is not involved in entropy-exchange processes for the superconductor and the quasiparticles, localized in the vortex cores², which are entropy carriers. Due to the presence of localized quasiparticles in the vortex cores, vortex motion results in entropy transport, which causes measurable thermal effects. Specifically, during field increase, new vortices are created at the edge of the sample, and quasiparticles inside the vortices absorb entropy from the atomic lattice and cause quasiadiabatic cooling of the sample. Conversely, during field decrease, the exiting vortices release their entropy to the atomic lattice, causing quasiadiabatic heating.

A superconductor subject to a changing magnetic field and allowed to exchange heat with the environment undergoes a temperature change. This process is described by the first law

$$dQ_{abs}/dt = n T_s (\partial S/\partial H)_T dH/dt + n C_s dT_s/dt \quad (2.9)$$

where dQ_{abs}/dt is the net rate of heat absorption, positive for absorption of heat by the sample, n is the molar number of the superconductor, T_s its temperature, $T_s (\partial S/\partial H)_T$ the molar magnetocaloric coefficient, and C_s the specific heat of the superconductor.

The schematic of the magnetocaloric setup is shown in Fig. 2.1. In this setup, absorption or release of heat from the sample results in minute, but measurable, variation of its temperature. In a typical measurement, the sample temperature is first fixed at a selected value T_0 . Subsequently, the field is ramped at a steady rate, resulting in quasi-adiabatic absorption or release of heat from the sample. The

²The quasiparticles are localized in the vortex cores only for s-wave superconductors.

resulting sample temperature change is recorded. As shown in the previous section

$$dQ_{abs}/dt = -\tilde{G}(T_0) \Delta T,$$

where $T_s = T_0 + \Delta T$ is the instantaneous sample temperature. The magnetocaloric term in Eq. 2.9 induces the temperature change. This is smeared out by the last term, incorporating the effect of specific heat. Nevertheless, in practice this last term is constrained to be negligible when magnetocaloric effects are measured. In our measurements, we use low field ramp rates dH/dt , which result in low temperature change rates dT_s/dt causing the last term to be negligible³.

Under this condition, the temperature change of the sample (ΔT) around its static value, T_0 , allows us to determine the molar magnetocaloric coefficient $T(\partial S/\partial H)_T$ by use of

$$n T_s (\partial S/\partial H)_T = -\tilde{G}(T_0) \Delta T (dH/dt)^{-1}. \quad (2.10)$$

Here the sample temperature, differential thermal conductance of the heat link $\tilde{G}(T_0)$, molar number for the sample n , and field ramp rate dH/dt are all independently measured. The latter is positive for increasing fields, negative for decreasing fields.

In deriving the above equations we assumed that heat is only exchanged between the superconductor and the environment and that the superconductor reaches its quasi-static state as the measurement is performed. In an actual experiment, non-equilibrium and irreversible effects need to be considered. The heat generated by the dissipative processes (i.e. friction) between the vortex lattice and atomic lattice leads to a modification of the left hand side of Eqs. 2.9 & 2.10. Non-equilibrium effects related to pinning and surface barriers lead to a modification of the right hand side of the equations. While the effects of the Bean-Livingston surface barrier [73], flux

³Note that Eq. 2.9 can be simplified to the form $\Delta T = A \dot{H} + B \Delta T$. As an example, consider the harmonic response to $H = H_0 e^{i\omega t}$ is determined by the magnetocaloric term $\Delta T \approx i \omega A H_0 e^{i\omega t}$ at low frequencies, $\omega B \ll 1$.

flow heating [37], and the Bean critical state [38, 39] can be complex and subtle, a detailed analysis has been performed and we now proceed to discuss these.

2.3.2 Irreversible and non-equilibrium effects

Here we evaluate the results of non-equilibrium and irreversible processes in the magnetocaloric measurements.

We start with the surface barrier. Its presence results in delay of flux entry into the sample on increasing fields, up to a field approximately equal to the thermodynamic critical field, H_C [74]. In addition, the surface barrier has the more subtle consequence of introducing an asymmetry between the measured ΔT on increasing and decreasing fields. On increasing fields, vortices have to enter the sample through an energy barrier in a vortex free region[75, 76]. In this process, entry of individual vortices to the bulk of the sample results in energy dissipation of $\Phi_0 \cdot ((H_C^2 + H^2)^{1/2} - H) / 4\pi$ per vortex unit length [75]. For the entire sample energy is dissipated approximately at a rate

$$\Phi_0 \cdot ((H_C^2 + H^2)^{1/2} - H) \cdot (V/4\pi) \cdot dH/dt,$$

where V is the sample volume and H_C the thermodynamic critical field.

In our measurements, for example at $H \approx 3000$ Oe, this amounts to approximately $2 \mu\text{W}$, and will reduce the (negative) ΔT observed on increasing fields by roughly 1 mK. On decreasing fields, the surface barrier has essentially no effect, and no irreversible heating is expected [75]. An asymmetry of this kind is shown schematically in Fig. 2.2a, and it is present in our data, which we present in the next chapter.

Flux flow heating of the sample leads to a similar asymmetry between the ascending and descending field branches. On increasing fields the negative ΔT is reduced and on decreasing fields the positive ΔT increased. An order of magnitude estimate of flux-flow heating can be obtained on the basis of the Bardeen-Stephen model [37].

For a cylindrical sample of radius R , length L , and for smooth field ramping at a rate dH/dt , one obtains $P_{ff} \approx 10^7 (dH/dt)^2 \pi R^4 L / (8\rho_{ff})$. This turns out to be negligible for the field ramp rates, approximately 1 Oe/sec, used in our measurements. We show the effect of this mechanism in Fig. 2.2b. Between the above two sources of irreversible heating, it is clear that low field ramp rates will render the latter ($\propto (dH/dt)^2$) negligible, but will not reduce the effect of the former which scales as dH/dt , as does the magnetocaloric ΔT .

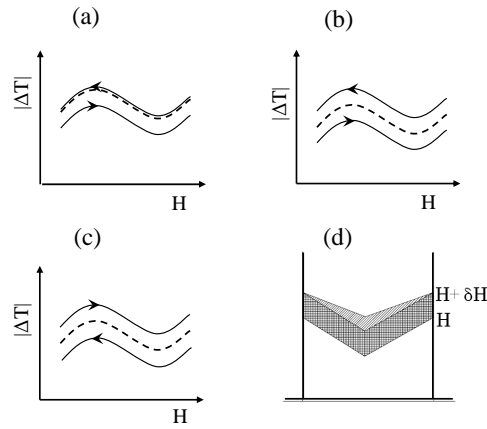


Figure 2.2: (a)-(c) Schematic representations of the asymmetries induced by irreversible and non-equilibrium effects on the magnetocaloric measurement, $|\Delta T|$. The field ramp directions are indicated by arrows, and the equilibrium $(\partial s/\partial H)_T$ curve corresponds to the dashed line. (a) Surface barrier heating. (b) Flux flow heating. (c) Critical state screening. (d) Qualitative schematic of the evolution of the critical state field profile, for increasing field and $\partial j_c/\partial H < 0$. When the applied field increases from H to $H + \delta H$, the flux increase corresponds to the total shaded area, not just the lower shaded part. This results in increased magnetocaloric signal, as shown in (c) and discussed in the text.

Next we examine the case of a non-equilibrium critical state profile outside the peak effect region. A critical current that monotonically decreases with field, i.e. away from the peak effect region, will result in the opposite asymmetry than the one just mentioned. This is so, because on increasing fields the critical state profile becomes less steep, resulting in faster loss of flux than the field ramp rate, and thus increased ΔT . The opposite occurs on decreasing fields, resulting in a lower ΔT than

indicated by the equilibrium $T(\partial S/\partial H)_T$. This mechanism is shown schematically in Fig. 2.2d. A simplified calculation for cylindrical sample geometry, like the ones found in the literature [38, 39, 77], yields an asymmetry factor in ΔT equal to (cgs units)

$$1 \pm (4\pi R/3c)(\partial J_c/\partial H)_T \quad (2.11)$$

for increasing (−) and decreasing (+) fields. Here, R is the sample radius and $J_c(H)$ the H dependent critical current.

To see how this factor of arises, consider a cylindrical sample geometry, with the field applied along the cylindrical axis. The critical current is taken to depend on B , or equivalently on H . We focus on the region close to H_{c2} , where these are linearly related by $B = (1 + 1/\zeta)H - H_{c2}/\zeta$, with $\zeta = \beta_A(2\kappa^2 - 1)$ [6]. Due to critical current screening, the local induction (or field) inside the sample is modified with respect to the applied field and depends on radial distance from the axis (r) of the sample $H = H(r)$. From the Ampère law the field variation resulting from the critical current is

$$\frac{dH}{dr} = \pm \frac{4\pi}{c} J_c(H(r)) ,$$

for increasing (+) and decreasing (−) field. The critical current depends on B , but we make the simplifying assumption that for a given value of applied field H_a , the local induction inside the sample leads to a negligible critical current variation $J_c(r) = J_c = const$. In addition we neglect demagnetizing effects. We then obtain

$$H(r) = H_a \pm (4\pi/c) J_c \cdot (r - R) ,$$

where R is the sample radius and again the solutions correspond to increasing (+) and decreasing (−) field. The corresponding magnetic induction is given by

$$B(r) = \left\{ H_a \pm \frac{4\pi}{c} J_c \cdot (r - R) \right\} \cdot (1 + 1/\zeta) - H_{c2}/\zeta .$$

This is easily integrated over the cross sectional area of the sample, in order to obtain the magnetic flux, Φ , through the sample

$$\Phi = \left\{ H_a \left(1 + \frac{1}{\zeta} \right) - H_{c2}/\zeta \mp \left(1 + \frac{1}{\zeta} \right) \frac{4\pi R J_c}{3c} \right\} \cdot \pi R^2. \quad (2.12)$$

Note that here the significance of the signs is reversed for increasing ($-$) and decreasing ($+$) field. The rate of change in magnetic flux through the sample for changes in applied field is

$$\frac{d\Phi}{dH_a} = \left\{ 1 \mp \frac{4\pi R}{3c} \left(\frac{\partial J_c}{\partial H} \right)_T \right\} \cdot \left(1 + \frac{1}{\zeta} \right) \cdot \pi R^2.$$

This is proportional to the magnetocaloric signal, and includes the asymmetry factor given in Eq. 2.11, with negative ($-$) sign for increasing, positive ($+$) for decreasing field.

2.4 Calorimetric setup

2.4.1 Calorimeter design

For both the calorimetric and magnetocaloric measurements, we used a homemade calorimeter, of which the idealized heat-flow diagram is shown in Fig. 2.1. A representative schematic of the physical setup used is shown in Fig. 2.3.

The calorimeter is encased in a top-loading brass-copper composite can, with brass tubing side (Alloy 260) and an an Oxygen-Free High-Conductivity (OFHC) copper (Alloy 110) bottom piece. The bottom piece is semi-permanently soldered to the brass tube using 95/5 (Sn-Sb) solder. The top cap of the outer can is constructed of brass. It has been silver-soldered at the end of the sample-insert steel tube. The two brass pieces can be temporarily soldered together using low-temperature indium based solder (Indalloy 117). This junction provides a fast and reliable vacuum-tight joint.

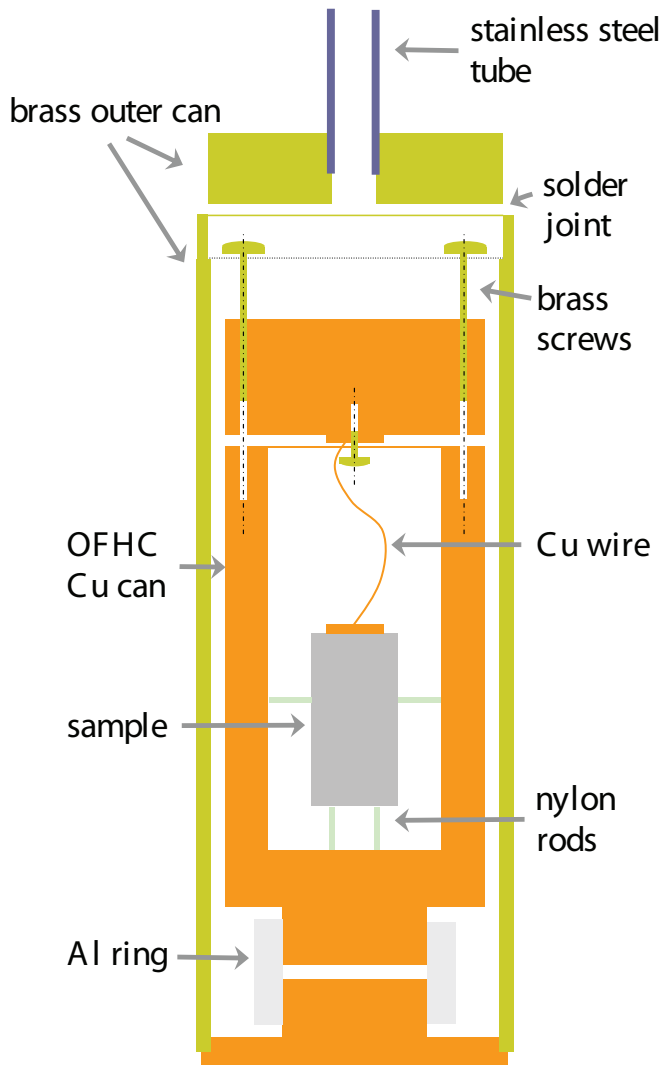


Figure 2.3: Design of the calorimeter used in our measurements. An outer brass can is used to maintain the vacuum conditions. An inner OFHC copper can serves the role of the heat bath, maintained at 4.2 K. The two are joined together by a thermal-contraction based thermal contact which uses an aluminum ring. The inner can is thermally connected to the sample via a piece of high-purity copper wire. The wire is attached to two OFHC copper disks using 95/5 (Sn-Sb) solder. One disk is attached to the sample using conductive silver epoxy. The other is fastened onto the heat-bath can with a brass screw. For simplicity we do not show the thermometers, sample heater, and ac-susceptometry coil.

Inside the external can, a second, internal, OFHC copper can serves the role of a heat bath. The internal can has an external cylindrical protrusion on its lower

side. The bottom lower cap of the external can has and identical internal protrusion machined to the same diameter with tolerance of less than 1 mil. When the calorimeter is assembled, the two pieces are joined together by an aluminum ring machined to have a slip-fit with the copper protrusions. At room temperature the three pieces can be easily assembled. On cooling, the aluminum ring contracts more than the copper pieces by more than 1 mil, providing thermal contact at low temperatures. The design of low-temperature heat contacts of this type is described in the classic Richardson and Smith book [78].

A piece of high purity copper wire is used as a thermal link between the sample and heat bath. The two ends of the copper wire are soldered on two polished OFHC plates using 95/5 (Sn-Sb) solder. This solder is superconducting below $\approx 3.7\text{ K}$, which will set the lower temperature limit for the usable range of the as-described setup. The plate on the sample side is attached to the sample surface using silver-filled epoxy (Spi supplies). The plate on the heat-bath side is held in place by a brass screw. The mechanical support for the sample inside the heat-bath can is provided by nylon rods.

Electrical manganin wire leads are brought into the calorimeter space through the stainless steel tube on the top of the external brass can. All of the leads are thermally anchored onto the heat-bath can with 1266 Styccast epoxy before proceeding to the sample stage.

2.4.2 Experimental procedures

During measurements, the heat bath is maintained at a temperature of 4.20 K and a carbon glass thermometer (Lakeshore) monitors its temperature. A second thermometer (Cernox, Lakeshore) is directly attached with silver epoxy to the lower end of the sample for reading the sample temperature. To minimize electronic noise in reading the thermometer resistance, a 10 kHz sinusoidal excitation together with

phase-sensitive detection is used. A Manganin wire, which is noninductively wound on the sample and secured with 1266 Stycast epoxy, serves as a heater. During measurements, the vacuum in the calorimeter is maintained to lower than 1 mTorr Hg by use of activated charcoal in thermal contact with the helium bath.

In the calorimetric measurements, the heat input to the sample is changed in a stepwise fashion. The duration of the heat-input steps is chosen to be in the range of 60 sec to 100 sec, depending on the temperature dependent thermal relaxation time of the sample through the heat link. This process is automated and computer-controlled, by use of Matlab code to control the digital instruments.

During magnetocaloric measurements, a constant heat input, P_{in} , is supplied to the sample through the manganin heater, fixing the temperature at a selected static value, T_{s0} . After the sample temperature has stabilized to T_{s0} , the magnetic field is ramped up, then down, at a constant rate. During a field ramp, the sample temperature as function of field, $T_s(H)$, is recorded. As we saw earlier, the temperature change of the sample (ΔT) around its static value, T_{s0} , allows us to determine the molar magnetocaloric coefficient $T_s(\partial s/\partial H)_T$ by use of Eq. 2.10. The magnetocaloric signal, $\Delta T(H)$, has to be measured with respect to a *field dependent*, static sample temperature *reading* $T_{s0} = T_{s0}(H)$, the thermometer reading at field H in the absence of field ramping. In other words one has to determine $\Delta T(H) = T_s(H) - T_{s0}(H)$.

The field dependence of the $T_{s0}(H)$ thermometer reading is a result of the following two effects: First, the magnetoresistance of the thermometer used. Second, a changing temperature gradient across the sample, as its field dependent thermal conductivity changes. This gradient can become considerable in the Meissner state for the highest measured temperatures ($\approx 8 \text{ mK / cm}$ at 8.33 K). Nevertheless, it is negligible (less than 0.5 mK / cm) in the peak effect region which is the main focus of this work. We stress here that the thermal gradient is a result of the external heat input P_{in} , not

the magnetocaloric effect.

A possible variation of the heat input with applied field, resulting from magnetoresistance of the heater, was investigated. It was verified that the heat input from the manganin heater does not vary by more than 1 part in 10^4 for the entire field range covered in any of our measurements.

The differential thermal conductance of the heat link between the sample and heat bath, G_{link} to be used in Eq. 2.9 above, is also measured at all temperatures of interest, for the entire range of applied fields. The link conductance is found to vary smoothly by no more than 1 part in 100 for the entire field range studied. This variation is insignificant compared to the random noise in the raw ΔT data.

Finally, the field ramp rate is measured through a resistor connected in series with the magnet coil, which allows us to monitor the current through the magnet. For all of the measurements presented here the ramp rate is 0.92 Oe/sec, which is the lowest possible with our system. At higher ramp rates, for example 1.87 Oe/sec, giant flux jumps were found to occur in the sample.

2.5 Magnetic ac susceptometry

2.5.1 Basic experimental setup

Magnetic ac susceptometry measurements provide a versatile tool for the characterization and study of magnetic and superconducting materials [79]. These measure the response of a system to an alternating magnetic field $H = H_0 e^{i\omega t}$. The response is probed by a pick-up coil, placed in the vicinity of the sample. The voltage induced on the coil is proportional to the rate of change of the spatially integrated induction (i.e. the magnetic flux)

$$V = N S \dot{B} = iN S \omega H (1 + 4\pi\eta\tilde{\chi}), \quad (2.13)$$

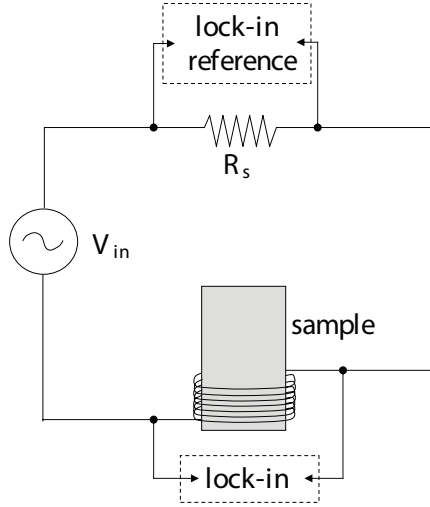


Figure 2.4: Circuit diagram for the ac-susceptometry setup used in our measurements. A signal generator provides the input voltage, V_{in} . A shunt resistor, R_s , is used to provide the in-phase signal to the reference channel of the lock-in amplifier. The coil is directly wound on the sample. The voltage on the coil terminals is fed into the signal channel of the lock-in amplifier.

where N is the number of turns in the coil, S the cross section per turn, and η is the coil filling factor. The real part of the complex susceptibility, $4\pi\chi'$, corresponds to the signal which is in phase with the applied field, while the imaginary part, $-4\pi\chi''$, yields the out-of-phase signal.

In terms of the susceptibility measurement circuit, the coil is described by a complex impedance $Z = R_0 + i\omega(1 + 4\pi\eta\tilde{\chi})L_0$, where R_0 is the resistance and L_0 the inductance of the empty coil. In writing this we assumed that the frequency is considerably far below the coil self resonance, and thus the coil parasitic capacitance is neglected. The inductive part is related to the real part of the susceptibility

$$L = (1 + 4\pi\eta\chi')L_0, \quad (2.14)$$

and a resistive contribution arises, due to the imaginary part

$$R = R_0 + 4\pi\omega\eta\chi''L_0. \quad (2.15)$$

In our measurements, we use the simple self-inductance circuit shown in Fig. 2.4.

The driving/pick-up coil is directly wound onto the sample. The ac signal is provided by a Wavetek signal generator. A 100Ω shunt resistor is connected in series with the coil. This allows us to obtain a reference signal *in-phase* with the current flowing through the circuit. The reference signal is sent to the reference channel of a PAR, Model 124A lock-in amplifier. The voltage across the coil is sent to the signal-input channel of the lock-in amplifier via a PAR, Model 116 differential preamplifier. A four point scheme is used for the measurement of the coil voltage.

In our measurements, the phase of the lock-in amplifier is adjusted in the normal state, at a temperature above T_c . The phase offset of the reference signal is adjusted so that it is 90° out of phase with the coil voltage. Since the reference voltage is in phase with the current, this configuration allows us to obtain the inductive part of the coil signal, i.e. it measures $4\pi\chi'$. The effect of the filling factor is taken into account by performing a normalization of the lock-in output which sets $4\pi\chi'$ to be -1 in the perfectly diamagnetic Meissner state at zero applied dc-field.

2.5.2 Application for superconductors

The response of a superconductor to an applied alternating magnetic field can be rather subtle, depending on the sample properties and the experimental conditions [79]. In cases where flux pinning is strong, the response of the superconductor to the applied field is determined by the Bean critical state model [38, 39]. In this case, the complex susceptibility can be calculated by taking into account the effect of Bean-type screening super-currents on the amount of flux flow into and out of the sample. The situation has been analyzed [54], yielding the results

$$4\pi\chi' = -\frac{\pi j_c d}{H_{ac}} \quad (2.16)$$

$$4\pi\chi'' = \frac{4j_c d}{H_{ac}} - \frac{16\pi j_c^2 d^2}{H_{ac}^2} \quad (2.17)$$

for complete penetration of the ac field into the sample, and

$$4\pi\chi' = -1 + \frac{H_{ac}}{4\pi j_c d} \quad (2.18)$$

$$4\pi\chi'' = \frac{H_{ac}}{3\pi^2 j_c d} \quad (2.19)$$

for partial penetration of the ac field. Here j_c is the critical current, H_{ac} the amplitude of the applied ac field, and d the sample dimension.

It is clear that in both situations the critical current increase at the peak effect will result in a dip in the real part of the susceptibility. This has become a standard way of identifying the peak effect in ac-susceptometry, and in the following chapters we use this technique to identify the location of the peak effect.

2.6 Small Angle Neutron Scattering

As mentioned, neutron diffraction is a unique tool in structural studies of vortex matter. Its power stems from the fact that it is a bulk probe, it can access large regions of a sample, and it is applicable over a wide range of fields and temperatures. Alternative techniques face limitations: Bitter decoration is limited to low fields, and can only access the sample surface [80]. Scanning probe microscopy requires atomically flat surfaces and is also limited to the sample surface [64]. Muon spin rotation can only give indirect information on the vortex structure [81].

In the following section we give a short introduction to the general aspects of neutron scattering from superconducting flux-line lattices. We then describe a geometrical Ewald construction applicable to small angle scattering experiments from flux-line lattices. This provides a useful tool in understanding the small angle neutron scattering rocking-curve measurements which we will discuss in Chapter 4. In addition it allows us to calculate the resolution function for these measurements.

2.6.1 General treatment of neutron scattering

Neutron diffraction from vortex matter occurs via the interaction of the neutron magnetic moment with the local magnetic field, $\mathbf{B}(\mathbf{r})$, inside the superconductor. Thus, neutron diffraction probes the flux-line lattice. The interaction potential, $U(\mathbf{r})$, can cause transitions between neutron plane-wave states $|\mathbf{k}\rangle$ and $|\mathbf{k}'\rangle$ with respective energies E and E' . The differential cross section for scattering into solid angle $d\Omega$ and energy interval $\hbar d\omega$ is given by [82]

$$\frac{d^2\sigma}{d\Omega d\omega} = \left(\frac{m}{2\pi\hbar^2} \right) \frac{k'}{k} |\langle \mathbf{k} | U | \mathbf{k}' \rangle|^2 \delta \left(\frac{E - E'}{\hbar} + \omega \right). \quad (2.20)$$

In small angle neutron scattering, one is interested in the structural information contained in the diffraction pattern. Then, neutrons of all final energies are summed for a certain element of solid angle, and the relevant cross section is

$$\frac{d^2\sigma}{d\Omega} \propto |\langle \mathbf{k} | U | \mathbf{k}' \rangle|^2, \quad (2.21)$$

The interaction potential contains contributions from all flux lines. One obtains

$$U(\mathbf{r}) = \sum_i V(\mathbf{r} - \mathbf{r}_i). \quad (2.22)$$

Using, this expression, one can separate the structure factor from the form factor

$$\langle \mathbf{k} | U | \mathbf{k}' \rangle = \sum_i \int e^{-i\mathbf{k}\cdot\mathbf{r}} V(\mathbf{r} - \mathbf{r}_i) e^{i\mathbf{k}'\cdot\mathbf{r}} d^3 r \quad (2.23)$$

$$= \sum_i e^{-i\mathbf{q}\cdot\mathbf{r}_i} \int e^{-i\mathbf{q}\cdot\mathbf{R}_i} V(\mathbf{R}_i) d^3 R_i \quad (2.24)$$

$$= \sum_i e^{-i\mathbf{q}\cdot\mathbf{r}_i} V(\mathbf{q}), \quad (2.25)$$

where $\hbar\mathbf{q} = \hbar(\mathbf{k}' - \mathbf{k})$ is the momentum transfer, and the change of variables $\mathbf{r} = \mathbf{R}_i + \mathbf{r}_i$ has been made. The form factor $V((\mathbf{q})$ in the above expression depends on the local magnetic field profile of an individual flux line. This can be computed numerically for arbitrary values of the magnetic induction and the Ginzburg-Landau parameter,

κ [83]. However, such a procedure is usually not necessary, since a convenient approximation exists for high values of κ , in the so-called London limit. In this case the penetration depth far exceeds the Ginzburg-Landau coherence length $\lambda \gg \xi$. Then, the local magnetic field outside the vortex core drops exponentially with distance, and as a result the vortex form factor is [5]

$$V(\mathbf{q}) \propto \frac{1}{1 + q^2 \lambda^2}. \quad (2.26)$$

Eventually, the cross section can be written

$$\frac{d^2\sigma}{d\Omega} \propto |V(\mathbf{q})|^2 \sum_{i,i'} e^{i\mathbf{q}\cdot(\mathbf{r}_i - \mathbf{r}_{i'})} \quad (2.27)$$

$$= |V(\mathbf{q})|^2 S(\mathbf{q}), \quad (2.28)$$

where the form factor and structure function contributions are separated.

The structure function reflects the structural properties of the flux lattice. The vortex assembly can be described by the density function

$$n(\mathbf{r}) = \sum_i \delta(\mathbf{r} - \mathbf{r}_i), \quad (2.29)$$

where if we assume the average magnetic field to be in the \mathbf{z} direction, the vortex positions can be parametrized by the coordinate along the field direction $\mathbf{r}_i = (\mathbf{r}_{\perp,i}, z)$.

Now, the density-density correlation function is simply

$$\overline{C_{nn}(\mathbf{r}, \mathbf{r}') = \left\langle \sum_{i,i'} \delta(\mathbf{r} - \mathbf{r}_i) \delta(\mathbf{r}' - \mathbf{r}_{i'}) \right\rangle}. \quad (2.30)$$

The angular brackets are now taken to imply thermal averaging and the over-bar implies average over quenched disorder. The structure function is the Fourier transform of the density-density correlation function

$$S(\mathbf{q}) = \int e^{-i\mathbf{q}\cdot(\mathbf{r}-\mathbf{r}')} C_{nn}(\mathbf{r}, \mathbf{r}') d^3r d^3r' \quad (2.31)$$

The neutron scattering cross section in an experiment is the averaged value given by the above expression, and it is obtained from the one of Eq. 2.28 after thermal and disorder averaging.

2.6.2 Small angle scattering rocking-curve measurements

We now discuss the specialized case of SANS experiments on flux-line lattices. In order to extract detailed information for the flux-lattice structure function from the scattering data, the instrumental resolution function has to be considered. Several authors [84, 85, 86] have considered the transverse resolution function entering in diffraction experiments. The three-dimensional resolution function of small angle scattering measurements has also been considered analytically using the Gaussian approximation [87, 88] and numerically using Monte Carlo simulations [88].

In rocking-curve measurements of FLLs, in which a FLL is rotated with respect to the neutron beam, the flux-line translational correlations in the direction of the magnetic field are probed. These measurements provide considerably higher resolution than that in the transverse (perpendicular to the magnetic field) direction. In these cases, an accurate assessment of the instrumental resolution is crucial for the deconvolution of the structure function from the measured intensity profiles. A method to determine the actual resolution function beyond the level of accuracy provided by the Gaussian approximation [88] is needed. For example, it has been noted in the Monte Carlo simulation of Harris *et al.* that the typical resolution function for rocking-curve measurements resembles a box-shaped function, which is poorly approximated in the Gaussian treatment. This discrepancy is most significant when studying systems where the intrinsic width of the diffraction peaks is close to the instrumental resolution limit. As an example, the FLLs in ultrapure superconducting samples [89, 56, 4, 36, 90] can give diffraction peaks that are resolution limited, or close to the resolution limit. Ideally, one would want to determine the resolution function for a given instrumental configuration by using direct measurements of the neutron beam collimation profile and the wavelength spread.

Here we describe a method for obtaining the resolution function for rocking-curve

measurements starting from the neutron beam collimation profile and wavelength spread. The calculation is simple, involving just two numerical integrations. As an example of this procedure we compute the resolution function for a given instrumental configuration of the 30m NG-3 instrument at NCNR-NIST, which employs a mechanical velocity selector and double pinhole collimation [91]. We compare these results with measured rocking curves which are close to the resolution limit, obtained on a FLL in niobium. The procedure we describe is built upon the Ewald construction, as applied to SANS on FLLs [32, 56]. The same description applies to diffraction from any medium consisting of line-like objects with a preferred average orientation of the lines and is useful in understanding various aspects of small angle diffraction by such systems. In specific, the Ewald construction offers a straightforward way to determine how different experimental parameters such as sample orientation, beam collimation, and wavelength spread affect the diffraction condition.

We consider a typical small angle scattering geometry, shown in Fig. 2.5, in which the neutron beam traverses the sample. A 2 dimensional position-sensitive neutron detector is located a certain distance from the sample, on the side where both the direct neutron beam and diffracted neutrons emerge. The orientation of the flux line lattice is rotated with respect to the incoming neutron beam by an angle ω . To achieve this, both the sample and magnetic field (in reality the entire magnet cryostat) are rotated with respect to the beam. This rotation is necessary for the sensitive alignment required to optimize the scattering conditions. It is also useful in performing rocking-curve measurements. In these measurements, the flux-line lattice is rotated with respect to the beam by ω , in a stepwise fashion. The intensity of a given Bragg peak varies with ω . This variation contains information about the longitudinal-parallel to the field-structure function of the lattice.

In what follows we will use two coordinate systems: The instrument-fixed frame

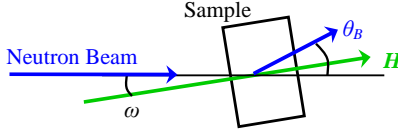


Figure 2.5: Scattering geometry in SANS measurements. The sample and magnetic field (thus, the flux line lattice) are rotated by ω with respect to the incident neutron beam. The diffracted neutrons satisfy the Bragg condition at angles θ_B .

is chosen such that the neutron beam travels in the $-z$ direction and the position sensitive detector lies on the xy plane, with x denoting the horizontal direction. In addition, we use a sample-fixed coordinate system, denoted by tilded symbols \tilde{x}_i . The orientation of the tilded coordinates is such that the average orientation of the line objects (e.g. the magnetic field) is in the \tilde{z} direction, while the \tilde{x} and \tilde{y} axes are chosen to be respectively parallel to the x , and y axes when $z \parallel \tilde{z}$. In other words, the tilded coordinates are rotated by ω with respect to the non-tilded ones (Fig. 2.6b). In practical situations, the rotation is about the vertical y axis and this will be the case we consider.

The Ewald construction offers a straightforward way to interpret scattering patterns from flux-line lattices. In reciprocal space, \mathbf{q} , the lattice corresponding to an ideal, infinite, flux-line lattice consists of a set points defined on a two dimensional plane, which by our choice of tilded coordinates is the $\tilde{q}_x \tilde{q}_y$ plane. For an imperfect lattice, long range order is lost and the reciprocal lattice points become diffuse three dimensional objects, each one centered at the position of a reciprocal lattice point of the ideal lattice. Values of momentum transfer corresponding to these points will satisfy the Bragg condition. When interference occurs, the intensity at a given point in \mathbf{q} space is determined by the structure function, $S_{av}(\mathbf{q})$, of the lattice. Interference occurs whenever the Bragg condition can be satisfied for a given scattering geometry. This is expressed geometrically by constructing a sphere in \mathbf{q} space centered on $(0, 0, -k_{in})$, with radius $|\mathbf{k}| = k_{in} = 2\pi/\lambda$, as shown in Fig. 2.6. This is the Ewald

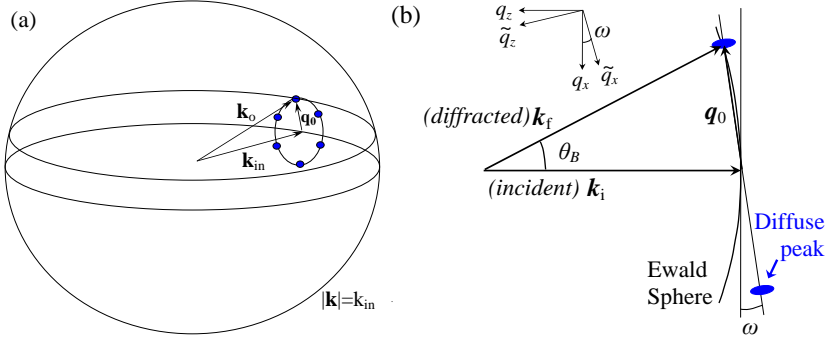


Figure 2.6: (a) Ewald construction for neutron scattering from a flux lattice. The Ewald sphere has radius $|\mathbf{k}| = k_{in}$ and is centered at $(0,0,-k_{in})$. The first order reciprocal lattice points of a hexagonal lattice are shown. A Bragg peak at momentum transfer \mathbf{q}_0 appears when the corresponding reciprocal lattice point intersects the Ewald sphere. (b) Construction corresponding to the geometry of Fig. 1, simplified to a two dimensional sketch. The diffuse reciprocal lattice peaks of a flux lattice are in reality compressed along the q_z direction due to the flux lattice elastic moduli. Here we present them elongated for ease of presentation.

sphere and describes the locus of diffracted neutron momenta consistent with momentum conservation⁴. Diffraction occurs whenever a reciprocal lattice peak intersects the Ewald sphere.

For the geometry represented in Fig. 2.5 the Ewald sphere is centered on $(q_x, q_y, q_z) = (0, 0, -k_{in})$ and the reciprocal lattice is rotated by ω around the \mathbf{q}_y axis. The tilded axes $(\tilde{q}_x, \tilde{q}_y, \tilde{q}_z)$, rotated by ω around \mathbf{q}_y (Fig. 2.6), serve to identify peaks of the rotated reciprocal lattice. This situation is depicted schematically in Fig. 2.6b. We consider a point in reciprocal space, given by

$$(\tilde{q}_{x0}, \tilde{q}_{y0}, \tilde{q}_{z0}) = (Q_0 \cos \tilde{\phi} \sin \tilde{\theta}, Q_0 \sin \tilde{\phi} \sin \tilde{\theta}, Q_0 \cos \tilde{\theta}). \quad (2.32)$$

Here the angles $\tilde{\theta}$ and $\tilde{\phi}$ are the usual polar and azimuthal angles in the tilded

⁴We can safely disregard the minute fuzziness of the Ewald sphere introduced by inelastic scattering processes

coordinate system. The location of this point in the unrotated axes is

$$q_{x0} = \tilde{q}_{x0} \cos\omega + \tilde{q}_{z0} \sin\omega \approx \tilde{q}_{x0} + \tilde{q}_{z0} \omega, \quad (2.33)$$

$$q_{y0} = \tilde{q}_{y0}, \quad (2.34)$$

$$q_{z0} = -\tilde{q}_{x0} \sin\omega + \tilde{q}_{z0} \cos\omega \approx -\tilde{q}_{x0} \omega + \tilde{q}_{z0}, \quad (2.35)$$

to first order in ω . In the case of flux line lattices, the structure function is sharp in the longitudinal (q_z) direction. The typical width $\Delta\tilde{q}_z$ is considerably smaller than the reciprocal lattice peak spacing $\tilde{q}_{x0,y0} = O(Q_0)$. Consequently the reciprocal lattice points of interest satisfy $\tilde{q}_{z0} \ll \tilde{q}_{x0,y0}$, so that the variation of q_{x0} by $\delta q_{x0} = O(\tilde{q}_{z0} \omega)$ in Eq. 2.33 above can be neglected.

These expressions elucidate how rotation of the sample allows us to obtain the longitudinal behavior of the line lattice structure function, along q_z . Consider a specific Bragg peak and integrate out the intensity on the $q_x q_y$ plane. Then, a variation in ω leads to variation in the reciprocal lattice \tilde{q}_z intersecting the Ewald sphere. The intensity profile obtained is, to first order, approximated by $I(\omega) \propto S_{av}(\tilde{q}_z = \tilde{q}_{x0} \omega)$, where the subscript “av” denotes integration in the transverse $(\tilde{q}_x \tilde{q}_y)$ plane.

2.6.3 The rocking-curve resolution function

In any diffraction experiment the measured intensity is a convolution of the structure function with the resolution function of the instrument used for the measurement. Thus, knowledge of the instrumental resolution function is necessary for performing the deconvolution of the structure function from any measured diffraction intensity profile. In the neutron diffraction experiments presented in this work the resolution function is determined by the incident beam wavelength spread and collimation. We now proceed to calculate it.

In the previous section we described the Ewald construction for a perfectly parallel and monochromatic beam. Variations in the incident beam direction lead to rotations

of the Ewald sphere with respect to the reciprocal lattice. Wavelength spread leads to a variation of the size of the Ewald sphere. The scattering pattern is the combined result of several different Ewald constructions with varying Ewald sphere sizes and orientations of reciprocal lattice with respect to the sphere. The instrumental resolution function in the rocking-curve measurement corresponds to the intensity $R(\omega)$ that would be obtained as a function of rotation angle, ω , from a $\delta(\mathbf{q}-\mathbf{q}_0)$ peak in reciprocal lattice. In what follows we will calculate resolution functions up to a normalization constant which can be determined by the normalization condition $\int R(\omega)d\omega = 1$.

The incident beam collimation is described by an angular intensity profile $I_0(\theta, \phi)$, which can be directly measured. Here θ and ϕ are polar and azimuthal angles in instrument-fixed spherical coordinates. Ideally, for double pinhole collimation and neglecting the effect of gravity on a non-monochromatic beam, the profile does not depend on azimuthal angle $I_0 = I_0(\theta)$. Parts of the incident beam with different directions correspond to different Ewald constructions, and each one will give rise to intensity from the δ peak at a slightly different rotation angle ω , thus giving rise to an intensity profile $I(\omega)$.

We include the effect of beam imperfect collimation by allowing the reciprocal lattice to rotate with respect to the Ewald sphere. The rotation is by θ_1 about $\tilde{\mathbf{q}}_y$ and then by θ_2 about the rotated $\tilde{\mathbf{q}}'_x$. The combined effect on the point at $(\tilde{q}_{x0}, \tilde{q}_{y0}, \tilde{q}_{z0})$ is

$$\begin{aligned}\tilde{q}_{x0}'' &= \tilde{q}_{x0} \cos\theta_1 - \tilde{q}_{z0} \sin\theta_1, \\ \tilde{q}_{y0}'' &= \tilde{q}_{x0} \sin\theta_1 \sin\theta_2 + \tilde{q}_{y0} \cos\theta_2 + \tilde{q}_{z0} \cos\theta_1 \sin\theta_2, \\ \tilde{q}_{z0}'' &= \tilde{q}_{x0} \sin\theta_1 \cos\theta_2 - \tilde{q}_{y0} \sin\theta_2 + \tilde{q}_{z0} \cos\theta_1 \cos\theta_2.\end{aligned}$$

In practice the angles θ_1, θ_2 are small, and we can expand the above to first order in

these angles. In addition, we take into account the condition $\tilde{q}_{z0} \ll \tilde{q}_{x0,y0}$, so that

$$\tilde{q}_{x0}'' = \tilde{q}_{x0}, \quad (2.36)$$

$$\tilde{q}_{y0}'' = \tilde{q}_{y0}, \quad (2.37)$$

$$\tilde{q}_{z0}'' = \tilde{q}_{x0} \theta_1 - \tilde{q}_{y0} \theta_2 + \tilde{q}_{z0}. \quad (2.38)$$

We consider the reciprocal lattice peak $\delta(\tilde{\mathbf{q}} - \tilde{\mathbf{q}}_0)$. This is located on the Ewald sphere for some $\omega = \omega_0$. By use of Eqs. 2.35, 2.38 we see that for the incident beam component which deviates from the average collimation by θ_1, θ_2 , this peak will be located on the Ewald sphere at $\omega = \omega_0 - \theta_1 + \tan(\tilde{\phi}) \theta_2$, with $\tilde{\phi}$ the azimuthal position of the Bragg peak on the $\tilde{q}_x \tilde{q}_y$ plane, *cf.* Eq. 2.32. The intensity at the new rotation angle is proportional to $I_0(\theta)$, where $\theta = \cos^{-1}(\cos\theta_1 \cos\theta_2)$.⁵

The collimation-related part of the resolution function magnitude at some ω can be computed by numerical integration of the measured radial intensity profile $I_0(\theta)$ for all combinations of θ_1, θ_2 consistent with the constraint $\theta_1 - \tan(\tilde{\phi}) \theta_2 = \omega$. This is expressed by

$$R_c(\omega) = \int_{-\pi}^{\pi} \int_{-\pi}^{\pi} I_0(\cos^{-1}(\cos\theta_1 \cos\theta_2)) \times \delta(\omega - \theta_1 + \tan(\tilde{\phi}) \theta_2) d\theta_1 d\theta_2.$$

The incident beam wavelength spread enters our analysis via the size of the Ewald sphere. We can introduce this effect into the resolution function starting from the case of a perfectly monochromatic beam, at incident wavevector k_{in} . We consider a δ peak in reciprocal space, the location of which is given by Eq. 2.32. This point is located on the Ewald sphere for rotation by the Bragg angle ω_0 . In the beam-fixed (non tilded) axes, the location of the delta peak satisfies

$$q_{x0}^2 + q_{y0}^2 + q_{z0}^2 = Q_0^2.$$

⁵This is simply the angle between vector $\hat{\mathbf{z}}$ and vector $\hat{\mathbf{z}}'$, rotated by small angles θ_1 around $\hat{\mathbf{y}}$ and θ_2 around $\hat{\mathbf{x}}$.

But it also belongs to the Ewald sphere, hence

$$q_{x0}^2 + q_{y0}^2 + (q_{z0} + k_{in})^2 = k_{in}^2.$$

Combination of the above two relations, leads to

$$q_{z0} = -Q_0^2 / 2k_{in}.$$

Use of this expression and Eq. 2.35 leads to the relation determining the angle of rotation, ω_0

$$\sin\omega_0 \cos\tilde{\phi} \sin\tilde{\theta} - \cos\omega_0 \cos\tilde{\theta} = Q_0/2k_{in}.$$

A slight variation of the incident wavevector (equivalently wavelength) by δk , results in a variation of the necessary angle of rotation by $\delta\omega$

$$(\cos\omega_0 \cos\tilde{\phi} \sin\tilde{\theta} + \sin\omega_0 \cos\tilde{\theta}) \delta\omega = -\frac{Q_0}{2k_{in}^2} \delta k.$$

This can be simplified, taking into account that in practice ω_0 is small and $\tilde{\theta}$ is almost $\pi/2$ (*cf.* discussion after Eq. 2.35)

$$\cos\tilde{\phi} \delta\omega = -Q_0/2k_{in}^2 \delta k.$$

The significance of the above is that for a non-monochromatic beam, the δ peak will give rise to diffracted intensity from neutrons of wavevector $k_{in} + \delta k$ at rotation angle $\omega = \omega_0 + \delta\omega$. The intensity at angle ω is proportional to the incident beam intensity at wavelength $k_{in} + \delta k$

$$R_\lambda(\omega) \propto I_\lambda(k_{in} - \frac{2k_{in}^2 \cos\tilde{\phi}}{Q_0} \omega), \quad (2.39)$$

where $I_\lambda(k)$ describes the distribution of wavelengths, and is well approximated by a Gaussian peaked at k_{in} .

Finally, we compute the complete resolution function. We assume that the wavelength distribution is independent of the angular orientation of a certain segment of

the neutron beam. This allows us to determine the resolution function as a convolution between the collimation and wavelength spread parts

$$R(\omega) = \int_{-\pi}^{\pi} R_c(\omega' - \omega) R_\lambda(\omega') d\omega'. \quad (2.40)$$

In what follows we perform the integrations numerically.

2.6.4 Small angle scattering setup

We performed SANS rocking-curve measurements on a FLL in a niobium single crystal on the NG-3 instrument at NCNR-NIST. We will report on the experimental findings in a later chapter. Here we compute the resolution function starting from the instrumental configuration and compare the result with experimentally obtained curves which are at the resolution limit.

The neutron wavelength was set to 6.0 Å, with 14% FWHM wavelength spread. The wavelength distribution for these settings is well approximated by a Gaussian [91]. Double pinhole collimation was used, with source aperture of 50 mm, sample aperture 6.35 mm, and source-to-sample aperture distance 15.78 m. We obtained a direct measurement of the incident beam profile on the SANS detector. The radial average versus angle $\alpha \equiv Q / k_{in}$ is shown in Fig. 3a. This is well approximated by⁶:

$$I(\alpha) = \frac{A}{1 + \exp((|\alpha| - 1.62)/0.26)},$$

where here and in what follows the angles are expressed in mrad. After correcting for the finite sizes of the sample aperture and the detector elements (pixels) we obtain a corrected angular profile. This is estimated by:

$$I_0(\theta) \propto \frac{1}{1 + \exp((|\theta| - 1.17)/0.16)},$$

⁶The functional form $f(x) = A / (1 + \exp(\frac{x-x_0}{a}))$ is used because it can adequately approximate box-shaped functions with a sharp cutoff around x_0 .

and it is shown by the red curve in Fig. 3b. After performing the integration defined in Eq. 2.39 one obtains the results represented by the green points in Fig. 3b. The result of the numerical integration is adequately described by the curve:

$$R_c(\omega) \propto \frac{1}{1 + \exp((|\omega| - 1.38)/0.29)}.$$

This is shown in black in Fig. 3b. The functions I , I_0 , R_c are even in ω , and we only show them for positive values of the argument.

The wavevector distribution for the settings used will be Gaussian, centered around $k_0 = 1.047 \text{ \AA}^{-1}$, with FWHM $0.14 k_0$. This is described by:

$$I_\lambda(k) \propto \exp(-((k - k_0)/0.084k_0)^2),$$

with k expressed in \AA^{-1} . Our measurements were performed at an applied magnetic field of 0.4 T , which corresponds to a scattering vector $Q_0 \approx 8.9 \times 10^{-3} \text{ \AA}^{-1}$. We will focus on a Bragg peak centered around $\tilde{\phi} = \pi/4$. Then, following Eq. 2.39, the wavelength contribution to the resolution function is a Gaussian given by:

$$R_\lambda(\omega) \propto \exp(-(\omega/0.51)^2).$$

Next, we can perform the integration of Eq. 2.40, to obtain the results shown in green in Fig. 3c. This is the instrumental resolution function. The results are well fitted by the “sharp cutoff” function:

$$R(\omega) \propto \frac{1}{1 + \exp((|\omega| - 1.38)/0.36)}.$$

The fit is shown by the black curve in Fig. 3c. The sharp cutoff of $R(\omega)$ is a result of the box-shaped angular intensity profile $I(\alpha)$. We note that $R(\omega)$ is not adequately described by a Gaussian. A Gaussian fit deviates from the curve by as much as $0.06 R(0)$.

The computed function slightly overestimates the width of the actual resolution function. For example, the rocking-curves of an ordered FLL in niobium, obtained

under the conditions introduced in our calculation, have half width of 1.2 mrad, as we will see in Chapter 4. This is approximately 87% of the width of the numerical integration result (1.38 mrad). This discrepancy is a result of the assumptions made in our calculation. We have assumed for simplicity that the neutron beam intensity profile is azimuthally symmetric, while in reality it shows asymmetry of the order of 25% in different azimuthal directions. In addition we assumed that the wavelength distribution in the beam is independent of the polar angle (θ) of the incident neutrons, whereas the two can be convoluted in an unknown way.

2.7 The niobium sample and sample properties

The sample used in this work is a niobium single crystal, which was kindly provided by the NIST Center for Neutron Research. It has an imperfect cylindrical shape (radius 0.5 cm, length 2.47 cm) with the cylinder axis oriented parallel to the [111] crystallographic direction. At the time of the magnetocaloric and calorimetric measurements the sample mass was 24.78 g.

The resistivity of the sample was measured at room temperature and at 10 K by use of the Bean Eddy-current technique [92]. We obtained $\rho_{300\text{K}} = 14.9 \mu\text{ohm cm}$ and $\rho_{10\text{K}} = 1.2 \mu\text{ohm cm}$. The residual resistivity ratio from 300 K to 10 K of this sample is 12. The low temperature resistivity value allows us to estimate the electronic mean free path by use of the Drude formula, $\Lambda = mv_F / \rho_n ne^2$. Using the values of $n = 5.56 \cdot 10^{22} / \text{cm}^3$ for the average free electron density and $v_F = 1.37 \cdot 10^8 \text{ cm/sec}$ for the average Fermi velocity [93], we obtain $\Lambda_{10\text{K}} = 720 \text{ \AA}$. The Pippard coherence length for pure superconductors is given by $\xi_0 = \hbar v_F / \pi \Delta(0)$ [5]. For niobium, with $\Delta(0) = 1.764 k_B T_c \approx 1.4 \text{ meV}$, one obtains $\xi_0 \approx 2050 \text{ \AA}$. Thus, the niobium single crystal used in this work is close to the dirty limit, $\Lambda \ll \xi_0$.

Previous to the experiments described here, the sample had been studied by means

of ac susceptometry and Small Angle Neutron Scattering (SANS) [4, 2]. Here we summarize results obtained in those measurements. For completeness, we also include properties of the sample derived in the course of our measurements.

The Nb crystal has a zero field transition temperature $T_c = 9.16\text{ K}$. The zero temperature upper critical field, is estimated from the slope of the upper critical field $H_{c2}(0) = -0.69 T_c (dH_{c2}/dT)_{T_c} \approx 5600\text{ Oe}$ [94]. The upper critical field for temperatures above 4K is well described by the relation $H_{c2}(\text{Oe}) = 8226 - 906 \cdot T(\text{K})$ [2]. This relation was used to adjust the calibration of the thermometers used in the magnetocaloric and calorimetric measurements, versus those used in the previous ac-susceptometry and SANS studies [4, 2].

We used the heat-pulse (relaxation) technique to perform a zero field specific heat measurement. From this measurement we obtain the thermodynamic critical field at zero temperature $H_c(0) = 1832\text{ Oe}$. This way we obtain the generalized Ginzburg-Landau parameter $\kappa_1(0) = H_{c2}(0) / \sqrt{2} H_c(0) = 3.4$. In addition from this measurement we find a superconducting transition width of 83 mK.

The values of upper critical field, thermodynamic critical field and normal state resistivity of this crystal are consistent with reported values of Nb with approximately 1at.% oxygen impurities [50, 95]. Energy Dispersive X-ray spectorscopic (EDX) studies repeatedly confirmed the existence of elevated oxygen concentration, approximately 25at.%, to a depth of several microns from the sample surface. Consequently, we expect the main impurity content of this crystal to be oxygen.

Chapter 3

Magnetocaloric and Calorimetric Measurements

3.1 Introduction

We saw in the first chapter how, in spite of early predictions [27, 28], the long-range topological order associated with broken continuous symmetries can survive in systems with random pinning [33, 34]. In bulk type-II superconductors with weak point-like disorder the existence of a novel Bragg glass phase has been predicted [34]. This reaffirmed experimental facts known since the 1970s, that vortex lattices in weak-pinning, bulk, type-II superconductors can produce pronounced Bragg peaks in neutron diffraction [31]. Recent experiments [4, 64] have shown that a genuine order-disorder transition occurs in vortex matter. This transition appears to be the underlying mechanism of the well-known anomaly of the peak effect [96] in the critical current near H_{c2} .

Previous studies in the niobium single crystal used in this work have revealed an intriguing picture of the peak effect in weakly-pinned conventional superconductors.

Neutron scattering has shown that a vortex lattice order-disorder transition occurs in the peak effect region. This transition shows hysteresis and is believed to be first order, separating a low temperature ordered phase from a high temperature disordered one [4]. The hysteresis was not observed across the lower field part of the superconducting-to-normal phase boundary. Magnetic ac-susceptometry showed that at lower fields the peak effect disappears as well, indicating further connection between the peak effect and the order-disorder transition [2]. In addition, the line of surface superconductivity, H_{c3} , terminates in the vicinity of the region where the peak effect disappears. These findings on the $H - T$ phase diagram are summarized in Fig. 3.1.

It was thus proposed that the peak effect is the manifestation of a first-order transition which terminates at a multicritical point (MCP) where the peak effect line meets a continuous, Abrikosov transition, H_{c2} . The MCP would be bicritical if a third line of continuous transitions ends there. The transition lines considered as a possible third candidate were a continuous vortex glass transition, T_{c2} , and the line of surface superconductivity. Alternatively, the MCP would be tricritical if the disordered phase is a pinned liquid with no high field transition into the normal state [2]. The disappearance of the peak effect at low fields has also been reported in other systems [52, 65, 97].

Thermodynamic considerations [2] suggest that the MCP is likely a bicritical point. Since bicriticality implies the existence of competing types of order in the vortex system the question of which of the two lines, T_{c2} or H_{c3} , is relevant to the bicritical point has major importance. Its answer will provide insight into the disordered vortex state above the peak effect and the disordering transition itself. Evidently, the possible relevance of surface superconductivity to the destruction of bulk Bragg glass ordering, and hence the existence of the multicritical point, cannot be dismissed a

a priori. In fact it is well known that surface premelting plays an important role in solid-liquid transitions [98].

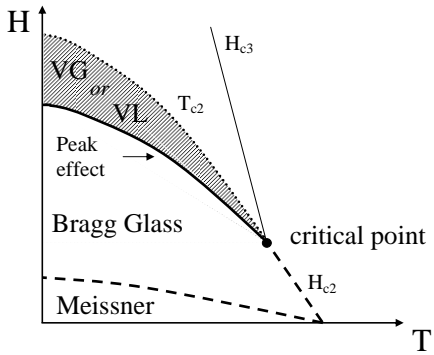


Figure 3.1: A sketch of the phase diagram of the Nb single crystal from Park *et al.* [2]. The nature of the phase in the shaded region remained undetermined, VG being a Vortex Glass, VL a Vortex Liquid phase. Note the definitions of distinct T_{c2} , H_{c2} and peak effect lines.

This issue could be resolved by repeating the ac magnetic susceptibility measurements after having suppressed surface superconductivity with appropriate surface treatment. Our efforts to nondestructively achieve this, e.g. by electroplating the sample surface with a ferromagnetic layer, proved unfruitful, possibly due to high oxygen content of the surface.

Here we report a study of the peak effect using a magnetocaloric technique. Clear features associated with the peak effect, have been identified in the magnetocaloric data. We find that the superconducting to normal transition shows inhomogeneity broadening at all fields. The peak effect in the bulk critical current becomes unobservable when it enters into the inhomogeneity broadened transition region. It is concluded that the concurrent disappearance of surface superconductivity and the peak effect is likely due to interference of surface superconductivity with the ac-susceptibility measurements. Nevertheless, the location of the MCP, as determined from magnetocaloric measurements, is in close vicinity to the location previously reported [2]. Moreover, the transition across T_{c2} has the same magnetocaloric signature

as that at H_{c2} , and surface superconductivity plays only a coincidental role in the critical point. This result suggests that the disordered vortex state, which is represented by the shaded part in Fig. 3.1, is a distinct thermodynamic phase. Bicriticality implies that this phase has an order parameter competing with that of the Bragg glass phase.

3.2 Calorimetric Measurements

Before presenting the magnetocaloric results, which are our main focus, we show selected results from a series of specific heat measurements. These did not reveal any anomalies in the peak effect region. Their value in this work is that they serve to determine, independently from magnetocalorics, the width of the superconducting transition and the absence of critical fluctuation broadening of the transition for upper critical fields up to 3400 Oe.

The setup described in the previous chapter was used to perform calorimetric measurements in zero field and at various applied fields. As already mentioned in the previous chapter, in these measurements we change the heat input to the sample in a stepwise fashion and record the resulting temperature change.

We show in Fig. 3.2 an example of representative temperature *vs.* time data, which were taken in zero applied magnetic field. We include data taken on both increasing and decreasing temperature. In Fig. 3.2c we show the exponential relaxation fit, $T = T_0 + \Delta T e^{-t/\tau}$, performed to these data. The fit follows the data remarkably closely. However, on decreasing the temperature step, ΔT , the fits become less reliable and the computed specific heat values start to display increased scatter. The limiting factor is the noise in reading the sample temperature. Empirically, a good compromise between the density of measured specific heat points and the noise in the final data was achieved by setting the temperature step to be in the neighborhood of 20 mK. For

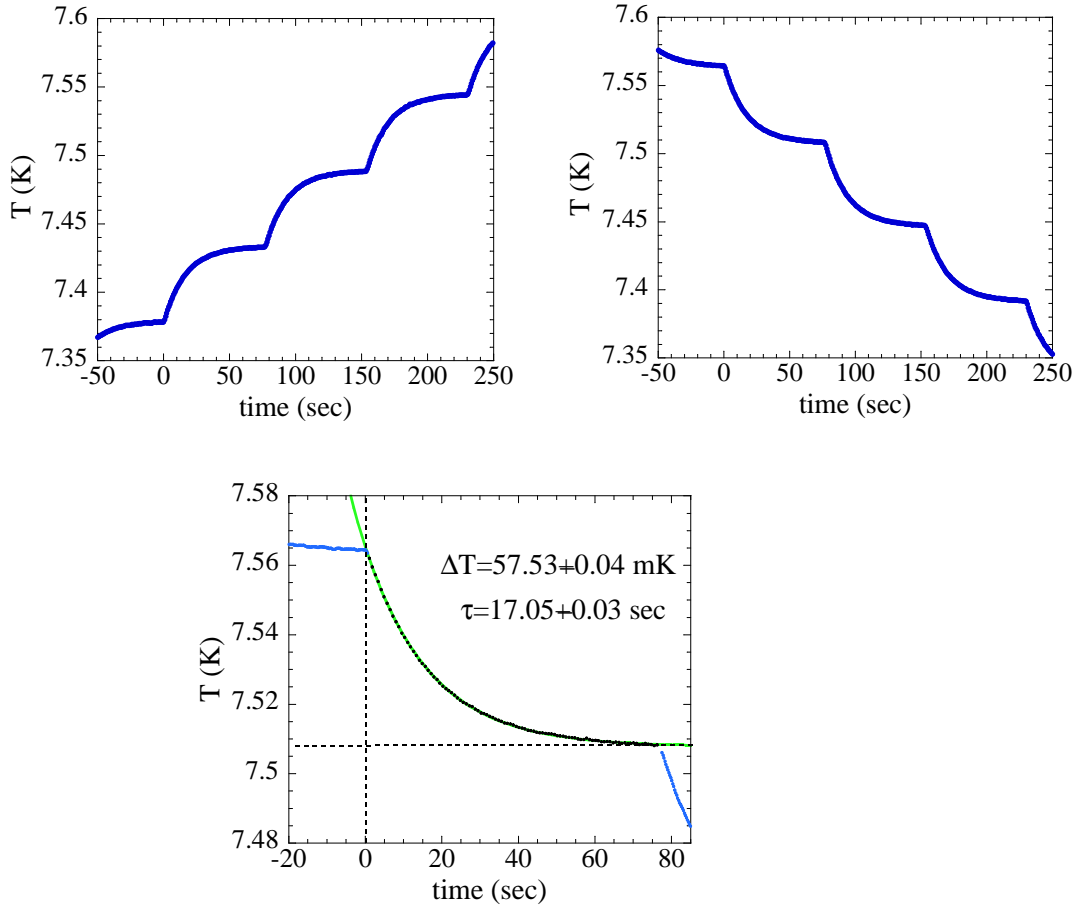


Figure 3.2: Example of temperature variation versus time in relaxation calorimetry measurements. Data shown are in zero applied field for (a) increasing and (b) decreasing temperature. In (c) we show an exponential fit performed to a temperature step. The fitted line $T = T_0 + \Delta T e^{-t/\tau}$ is shown in green. The data points over which the fit was performed are shown in black. The preceding and subsequent temperature steps are shown in blue.

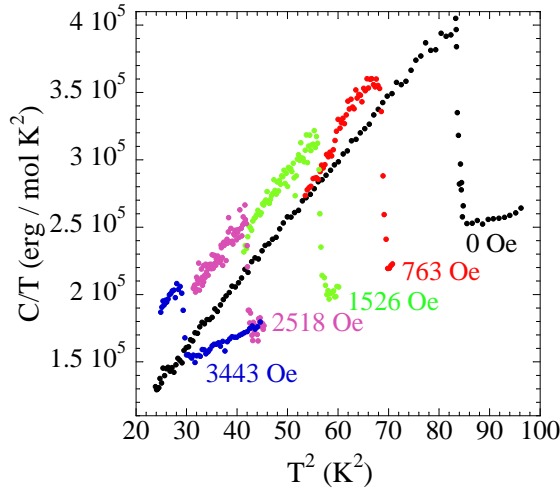


Figure 3.3: Measured values of C/T versus T^2 . The values of applied H field are shown in color code corresponding to the respective data points. The measurements were performed on increasing temperature. The decreasing temperature data are identical. No features corresponding to the peak effect are discerned.

smaller temperature steps the thermometry noise rendered the specific heat results unusable.

We show a representative summary of the specific heat measurements at various values of the applied magnetic field in Fig. 3.3. These measurements were performed on increasing temperatures, but the decreasing temperature measurements are identical within the reproducibility of our results. These measurements did not reveal any specific heat signature of the peak effect. In addition, no hysteresis in the neighborhood of the upper critical field was discerned. For example, we show in Fig. 3.4 the measurements at 3052 Oe for increasing and decreasing temperature.

In conclusion, the relaxation technique does not offer enough sensitivity to allow us to conclude that no latent heat is involved in the peak effect transition. On the other hand these measurements offer a good measure of the superconducting transition width and of the thermodynamic critical field in our sample. The superconducting transition in the measured curves varies by a few percent about an average of 83 ± 8 mK to within one standard deviation. The individual transition widths for different fields

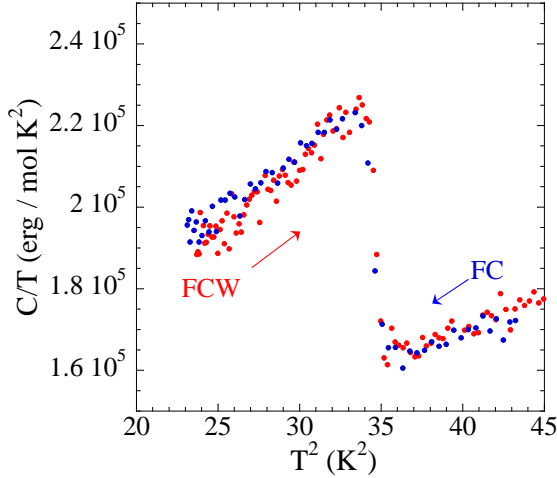


Figure 3.4: Specific heat measurements at an applied field of 3052 Oe. The measurements were performed upon in field cooling (FC) and subsequent field cooled warming (FCW). The behavior is reversible to within our resolution.

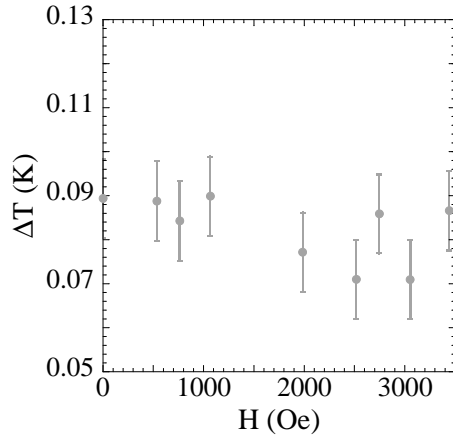


Figure 3.5: Superconducting transition widths as a function of applied field from the specific heat measurements. No change is detectable as the field is varied.

are shown in Fig. 3.5.

3.3 Magnetocaloric Measurements

As discussed in the previous chapter, the magnetocaloric coefficient is determined by recording the change of the sample temperature around its static value during H -field

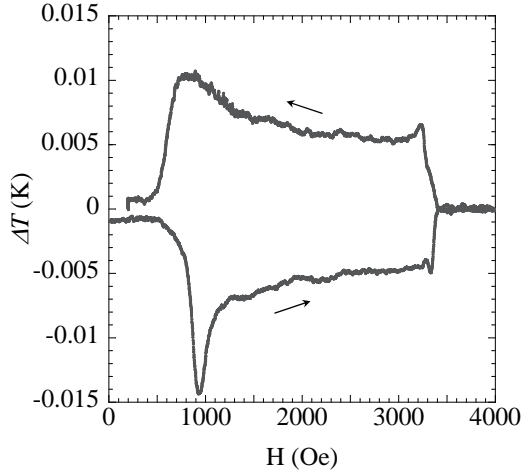


Figure 3.6: Magnetocaloric temperature variation around $T_{s0} = 5.37\text{ K}$ *vs.* applied field, for increasing and decreasing field. The field ramp direction is indicated by arrows. $dH/dt = 0.92\text{ Oe/sec}$ was used.

ramps. The two were shown to be connected by the relation

$$n T_s (\partial S / \partial H)_T = -\tilde{G}(T_0) \Delta T (dH/dt)^{-1}. \quad (3.1)$$

In Fig. 3.6, a typical example of raw magnetocaloric data in a full field scan is shown. The measured temperature change ΔT is of the order of a few mK at the lowest measured temperature of 4.2 K, and as a result high resolution temperature measurements are crucial.

In what follows, we choose to display the magnetocaloric coefficient normalized by the sample temperature. We denote this quantity by (dS/dH) . This can be straightforwardly perceived as the product of the entropy per vortex with the amount of vortex flux flow into, or out of, the sample. The reason for choosing to use the above notation, instead of $(\partial S / \partial H)_T$, is that the measured quantity is not the thermodynamic magnetocaloric coefficient due to the presence of irreversible and non-equilibrium effects already discussed in chapter 2.

Main features in field scans

In Fig. 3.7a & Fig. b, we summarize the molar entropy derivative, (dS/dH) , measurements on increasing (a) and decreasing (b) fields, at different temperatures. (dS/dH) is calculated from the $T_S(H)$ data following the procedure outlined earlier.

As indicated for the lowest temperature curve, 4.83 K (the upper most curve in Fig. 3.7a), several important features are to be noted. On increasing fields a peak occurs at low field. This is marked by H_1 . It corresponds to the lowest field for vortex entry through a surface barrier. Its locus on the $H - T$ plane closely follows the thermodynamic field, $H_c(T)$, but occurs slightly lower. This behavior is expected for a sample with finite demagnetizing factor and mesoscopic surface irregularities [74]. It should be emphasized, that the field H_1 is larger than the lower critical field, $H_{c1}(T)$. No peak corresponding to H_1 is present on decreasing fields. Rather, a smoother increase of (dS/dH) occurs as the field is lowered, before entry of part of the sample into the Meissner state where the magnetocaloric signal vanishes, as seen in Fig. 3.6 & Fig. 3.7b.

In intermediate fields, we identify a novel feature which was not observed in previous magnetic susceptibility studies [2]. This appears as a knee in (dS/dH) , which shows larger negative slope as a function of field for fields lower than H_{knee} , as illustrated in Fig. 3.7c. The feature is the same for both field-ramp directions. With our setup we can identify the H_{knee} feature up to 7.41 K. As the temperature is increased, the region between H_1 and H_{c2} narrows and it becomes increasingly difficult to discern H_{knee} . Thus it is unclear how this new feature terminates, i.e. whether it ends on the H_{c2} line at around $H = 1000$ Oe, or if it continues to lower fields.

At high field, across H_{c2} , the equilibrium mean-field theory of Abrikosov predicts a step function for M_T [6]. Thus, in the simplest picture one would expect a simple step of the molar entropy derivative $(\partial S/\partial H)_T$ at H_{c2} . Instead, we observe that across the

peak-effect regime, complex features of valley and peak appear in (dS/dH) below the field marked H_{c2}^{up} . The valley in (dS/dH) corresponds to the peak effect, as indicated in Fig. 3.7. Similar features appear on decreasing the field. At fields above the peak effect, the disappearance of the magnetocaloric effect marks the upper critical field, H_{c2} . As we will soon discuss, the upper critical field shows inhomogeneity broadening. In Fig. 3.7 we mark with H_{c2}^{up} the upper end of the upper critical field. This is the value of field at which the magnetocaloric signal in the mixed state exceeds the normal state noise level. Our technique is not sensitive to H_{c3} effects and the data are featureless above H_{c2}^{up} .

Identification of the peak effect

To verify the identification of the peak effect in our measurements, we performed simultaneous magnetocaloric and ac-susceptibility measurements, as shown in Fig. 3.8a. In the quasi-adiabatic magnetocaloric setup, the ac-amplitude used for the susceptometry measurements has to be small. For large amplitudes inductive heating occurs in the mixed state and the sample temperature increases rapidly by several degrees *as the peak effect is crossed*. We used an amplitude of 0.5 Oe at 107 Hz as a compromise between feasibility of the magnetocaloric measurement and resolution in the χ' results. The results are shown in Fig. 3.8a.

In this combined measurement we find that both the onset and the peak of the peak effect have corresponding features. Moreover, we find no clear change in χ' when the upper critical field, determined from the magnetocaloric measurement, is crossed. A slight change occurs in the slope of the $\chi'(H)$ curve across H_{c2} , but significant amount of screening, caused by surface superconductivity, remains when the bulk of the sample is in the normal state. This is a typical example of the inadequacy of ac-susceptometry in determining the upper critical field. Even with the use of larger

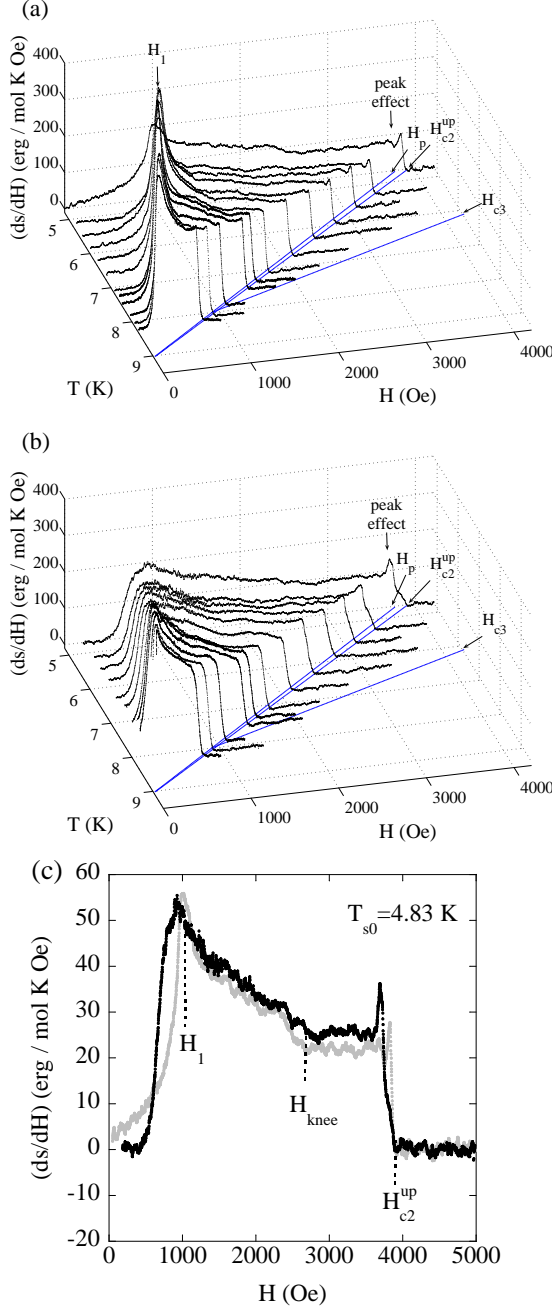


Figure 3.7: Results of magnetocaloric measurements on (a) increasing and (b) decreasing field. Also shown (in blue) are the loci traced on the $H - T$ plane by H_p , H_{c2}^{up} , and H_{c3} . The H_{c3} line is drawn according to Park *et al.* [2]. (c) Full field scan at $T_{s0} = 4.83$ K. Grey: Increasing field. Black: Decreasing field. The fields H_1 and H_{knee} , and the upper limit of the upper critical field are marked.

ac fields the change in slope of $\chi'(H)$ turns into a shoulder which does not reveal the exact location or characteristics of the bulk superconducting transition [2].

Features of the peak effect

In light of the first-order transition underlying the peak effect [4], it is tempting to interpret the peak appearing in (dS/dH) at the peak effect as a manifestation of the entropy discontinuity of the transition. Nevertheless, a simpler interpretation is offered in the context of critical state [38, 39] induced, non-equilibrium magnetization during the field ramps.

We start with increasing field data. At temperatures below 6.79 K the peak effect is observed, resulting in the following behavior: The magnetocaloric signal starts dropping at the onset, H_{on} , of the peak effect. A minimum occurs in the vicinity of the peak of the peak effect, H_p , and it is followed by a peak, see Fig. 3.8b. This indicates slowing down, then acceleration of vortex entry into the sample, as the critical state profile becomes steep, then levels, in the peak effect region. Finally the magnetocaloric signal gradually drops to zero in the region of the upper critical field.

On decreasing field a magnetically reversible region is revealed to exist for fields between H_{end} , the “end” of the peak effect, and H_{c2}^{up} . This is shown in Fig. 3.8b. Such behavior can be understood keeping in mind that the upper critical field in our sample is characterized by inhomogeneity broadening. We believe that the sliver of magnetic reversibility corresponds to the appearance of superconducting islands in our sample. These give rise to magnetocaloric effects, but they are isolated within the bulk and cannot support a screening supercurrent around the circumference of the sample, hence the reversible behavior. The “end” of the peak effect marks the onset of irreversibility and corresponds to a shoulder in the decreasing field curve. This occurs when continuous superconducting paths form around the sample and a

macroscopic critical current is supported. As the applied field is lowered below H_{end} , flux exit is delayed due to the increase in critical current. When $H < H_p$, the critical state profile relaxes and accelerated flux exit results in the observed peak in (dS/dH) below H_p .

(dS/dH) peak in absence of peak effect

In both field-ramp directions, the features due to the peak effect become less pronounced with increasing temperature, and finally become unobservable even before the previously identified [2] critical point is reached. On increasing fields, for $T > 7.18 \text{ K}$, a new peak appears in (dS/dH) just below the critical field, shown in Fig. 3.8c. A similar feature has already been reported in calorimetric measurements in pure Nb and Nb₃Sn [16, 18]. It has been attributed to critical fluctuations in the superconducting order parameter which set in as the critical field is approached [13]. If this is the cause of the observed peak, we expect it to exist in the curves displaying the peak effect features, but its presence will be obscured by the dramatic results of non-equilibrium magnetization discussed above. Interestingly a similar peak is *not* observed on the decreasing field data, Fig. 3.8c. It is evident in Fig. 3.8c, that apart from hysteretic behavior over an approximately 100 Oe wide region between H_{hyst} and H_{c2}^{up} the behavior of the sample is reversible to within noise levels. We attribute this to critical state flux screening in opposite field-ramp directions. The hysteresis occurs consistently at all temperatures where the peak effect is not observed.

The superconducting to normal transition region

A striking feature of our data is the invariance of the shape of the transition into (or out of) the bulk normal state with changing temperature, or critical field. For increasing fields, the transition into the normal state occurs between the fields H_0

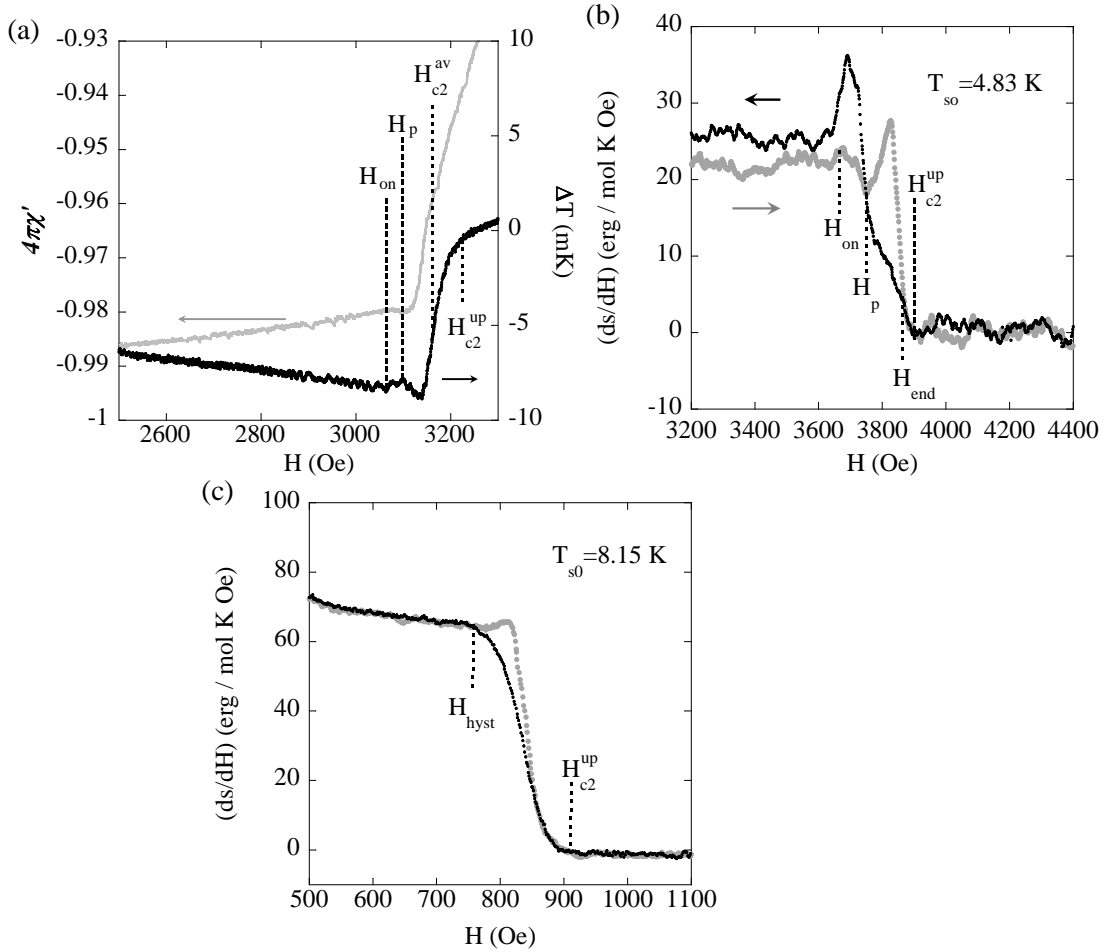


Figure 3.8: (a) Magnetocaloric temperature variations and ac magnetic susceptibility for increasing field, at $T = 5.76 \text{ K}$. The peak effect in χ' is not pronounced due to the small ac amplitude used ($h_{ac} = 0.5 \text{ Oe}$, $f = 107 \text{ Hz}$). (b) Detail of magnetocaloric measurement in the upper critical field region at $T = 4.83 \text{ K}$. Grey: increasing field. Black: Decreasing field. (c) Same as b, at $T = 8.15 \text{ K}$.

and H_{c2}^{up} , where (dS/dH) drops to zero monotonically. To illustrate this, in Fig.3.9 we show the *normalized* entropy derivatives as a function of field for temperatures ranging from 4.83 K to 8.33 K, with an expanded view of the upper critical field region. The normalization has been performed such that the average of $(dS/dH)_n$ over a 50 Oe wide region below the onset of the peak effect equals unity. The curves have also been horizontally offset, on a $\Delta H = H - H_{c2}^{\text{up}}$ axis. The horizontal alignment can alternatively be performed by aligning the ordinate of either H_0 , or the part of the curve where the signal equals a given value, for example 0.1 in the normalized Y axis. All different criteria result in alignments differing by only a few Oe. The case is similar for decreasing fields.

In Fig. 3.9a we present increasing field data that display the peak effect on the normalized/offset axes. For comparison, one curve which does not display the peak effect has been included. This corresponds to $T = 7.41$ K. In Fig. 3.9b we present the corresponding decreasing field data. In Fig. 3.9c we show only curves without a peak effect, for both increasing and decreasing field. These figures illustrate the uniform characteristics of the transition between the mixed state and the normal state. This is most evident in Fig. 3.9c: All different curves collapse onto one uniform curve for each field ramp direction. In Fig. 3.9a & Fig. 3.9b, the occurrence of the peak effect results in variations of the magnetocaloric signal around this uniform transition. These variations are, as already discussed, consistent with critical state induced flux screening on the field ramps. The uniformity of the transition for all field values implies that critical fluctuation broadening of the transition plays a minor role in our sample. Rather, inhomogeneity broadening seems to be the cause for the observed behavior.

For increasing fields the gradual disappearance of the magnetocaloric signal in the region between H_0 and H_{c2}^{up} corresponds to the gradual loss of bulk superconductivity

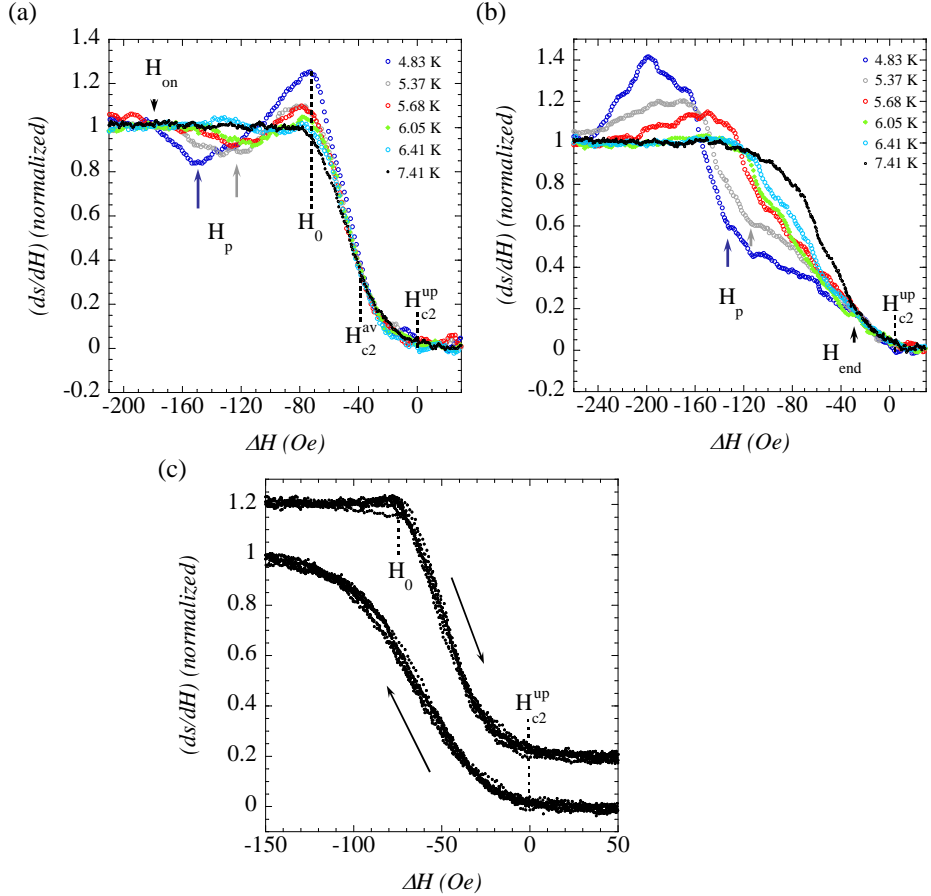


Figure 3.9: Normalized entropy derivative (ds/dH) versus $\Delta H = H - H_{c2}^{up}$, for the magnetocaloric data in the upper critical field region. (ds/dH) is rescaled to unity in the ΔH region between -300 and -250 Oe. (a) Increasing field data with and without the peak effect. The 7.41 K data do not show peak effect. The upper critical field shows inhomogeneity broadening between fields H_0 and H_{c2}^{up} . (b) Same as a for decreasing field. (c) Collapsed magnetocaloric curves without peak effect, for increasing (top, vertically offset by +0.2) and decreasing (bottom) fields. Temperatures included: 7.18 K, 7.41 K, 7.55 K, 7.94 K, 8.15 K, 8.33 K.

in our sample. In all of our measurements, the width $H_{c2}^{\text{up}} - H_0$ is essentially constant around a mean of 74.1 ± 1.9 Oe (Fig. 3.9a & Fig. 3.9c), which translates to a width of 78.8 ± 2.0 mK on the temperature axis. This value is in good agreement with the value of 83 mK obtained in the calorimetric measurement, given the finite temperature step of 10 to 15 mK used in the latter. Based on the identification of the lower and upper limits of the upper critical field, we identify the location of the mean field transition, H_{c2}^{av} , to be in the midpoint of the H_0 to H_{c2}^{up} range, see Fig. 3.9a. Local variations in electronic properties in the sample cause the broadening around this value.

The width of the superconducting transition is significantly larger than the expected lowest Landau level fluctuation broadening of the transition given by

$$\begin{aligned}\Delta T_{fl} &\approx 10 \delta \\ &= 10 \left(\frac{k_b}{8\pi\xi_0^3\Delta c(T)} \frac{B}{T_c(0)dH_{c2}/dT} \sqrt{\frac{T}{T_c(0)}} \right)^{2/3} T \\ &\approx 20 \text{ mK}\end{aligned}$$

at 4000 Oe [16, 13]. Consequently, it is not surprising that no broadening of the transition is observed with increasing field. In the above expression the coefficient of 10 multiplying δ is an approximation to the range over which the transition gets broadened in the LLL treatment of Thouless [13]. The exact expression for broadening of the H_{c2} transition has been tested experimentally in Nb [16] and Nb₃Sn [18] and the results are in excellent agreement with the theoretical predictions.

3.3.1 Discussion

Disappearance of the peak effect in (ds/dH)

We already mentioned that in the magnetocaloric measurements the peak effect becomes unobservable for temperatures above 7.18 K, or critical fields H_{c2}^{av} below

1718 Oe. However, in previous χ' ac-susceptometry measurements on the same sample, the peak effect was found to occur for fields as low as 900 Oe [2]. We believe this discrepancy is a result of the two different techniques used. Magnetocaloric measurements probe bulk flux changes and critical currents in the sample, while ac-susceptometry is more sensitive to effects occurring near the surface.

We will see that the peak effect becomes unobservable in the magnetocaloric measurement when it crosses into the region where only parts of the sample are superconducting. This occurs in the vicinity of 1700 Oe. It is not clear whether the bulk peak effect continues to exist for lower fields. It seems likely that it becomes undetectable due the absence of bulk macroscopic critical current in the partially superconducting sample. However, the peak effect continues to manifest in ac-susceptibility [2]. This is not surprising, since surface superconductivity assists in the formation of current-supporting, superconducting paths near the sample surface, even when such paths do not exist in the bulk (cf. Fig. 3.8a). This argument also provides an explanation for the approximately simultaneous disappearance of the peak effect and surface superconductivity in previous work [2].

In order to follow the evolution of the peak effect in magnetocalorics, we trace the evolution of the positions of the onset and peak features in our increasing field data. We focus on increasing fields, because in these the range of the upper critical field transition between H_0 and H_{c2}^{up} is clearly discernible. The locations of H_0 and H_p are each identified by the intersection of two linear fits on different sections of the (dS/dH) curve. Each fit is performed in a limited ΔH range on either side of the turning point where the feature occurs. For example, H_p is defined by the intersection of two linear fits to the data, one roughly in the range of H_{on} to H_p and one in the range of H_p to H_0 .

Following this procedure, we construct an $H - T$ diagram of the observed features.

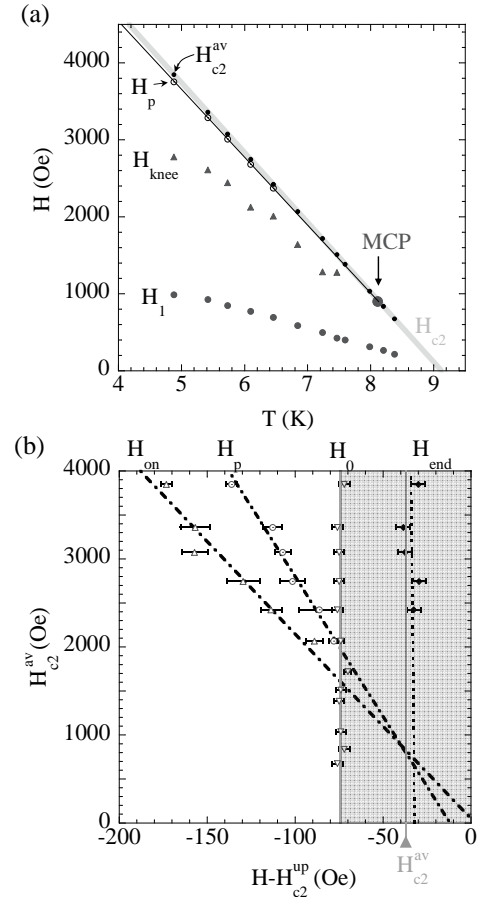


Figure 3.10: Phase diagram obtained from magnetocaloric measurements. (a) The identified features in H – T axes. The thin solid line and wide shaded line are linear fits through H_p and H_{c2}^{av} . The width of the H_{c2} line represents the extent of inhomogeneity broadening. The location of the MCP after Park *et al.* is indicated. (b) Detail of the upper critical field region: distance of various features from the conventionally defined H_{c2}^{up} line, vs. H_{c2}^{av} . The shaded area corresponds to the upper critical field region.

In Fig. 3.10a we show the positions of H_1 , H_{knee} , H_p , and H_{c2}^{av} in H vs. T axes. We also indicate the position of the MCP as identified by Park *et al* [2]. In Fig. 3.10b we focus on the region of the peak effect. For this reason we choose ΔH vs. H_{c2}^{av} axes. We mark the positions of the onset, the peak, and the end of the peak effect, as well as the lower end (H_0) and the midpoint (H_{c2}^{av}) of the H_{c2} transition. It is evident in this more detailed figure that the peak effect is no longer observed after it has crossed over into the H_0 to H_{c2}^{up} range, where bulk superconductivity is partially lost due to sample inhomogeneity.

These results also support the previously proposed multicriticality picture [2]. The observation with ac-susceptometry of a continuation of the bulk peak effect line on the surface of the sample is an indication that the peak effect continues to exist in isolated superconducting islands inside the sample, despite the existence of normal regions. Moreover, as shown in Fig. 3.10, the linear extrapolation of the onset and the peak of the peak effect, as well as H_{c2}^{av} , merge at a field of approximately 850 Oe, suggesting that this may indeed be the vicinity of the critical point where the first-order phase transition underlying the peak effect ends.

The H_{c2} and T_{c2} transition lines

The nature of the MCP which was previously identified by Park *et al.* [2] remained unresolved. As discussed, our findings suggest that surface superconductivity plays only a coincidental role in the disappearance of the peak effect. Thus, the nature of the MCP is determined from the nature of the H_{c2} and T_{c2} lines mentioned in the beginning of this chapter.

We have a means of comparing the H_{c2} and T_{c2} transitions. The approximate location of the MCP in ac-susceptometry is at $T = 8.1$ K, $H = 900$ Oe. Yet, as mentioned the peak effect becomes unobservable in magnetocaloric measurements in the

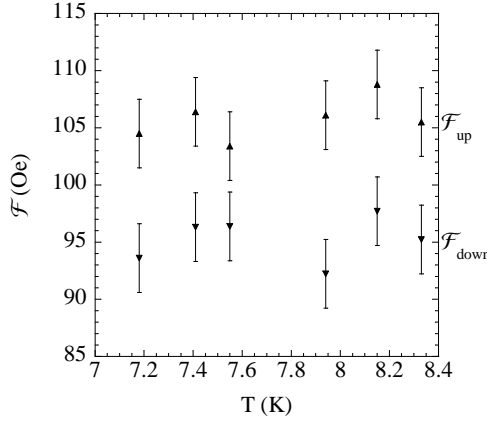


Figure 3.11: Integrals of $(ds/dH)_n$ for ΔH from -150 Oe to 30 Oe, for increasing (\mathcal{F}_{up} , \blacktriangle) and decreasing (\mathcal{F}_{down} , \blacktriangledown) fields. The peak effect feature was not observed at these temperatures. The error bars reflect the uncertainty in alignment of the magnetocaloric curves. Temperatures above 8.15 K correspond to the H_{c2} line of transitions indicated by Park *et al.* [2].

neighborhood of 7.0 K, 1700 Oe on the (T, H) plane. This allows us to compare the magnetocaloric transitions into the bulk normal state on the two sides of the proposed MCP. As shown in Fig. 3.9c, all the curves with $H_{c2}^{\text{av}} < 1718$ Oe (or equivalently $T > 7.18$ K) for both increasing and decreasing fields collapse strikingly on two different curves. These data include transitions on both sides of the MCP. This suggests that the phase transitions out of the Bragg Glass (H_{c2}) and disordered (T_{c2}) phases are of the same nature. In other words, well defined vortices exist in the disordered vortex state above the peak effect. Here “well defined” is taken to mean that their magnetocaloric signature is indistinguishable from the one obtained in the transition between the normal and the Bragg Glass phases. However, it has to be borne in mind that changes in critical behavior can be subtle and hard to identify in our sample which shows significant inhomogeneity broadening.

We can overcome this difficulty and look for changes in critical behavior by integrating the normalized experimental curves, $(ds/dH)_n$. This way, a change or a

trend in critical behavior obscured by inhomogeneity broadening, will be more easily discernible as a trend in the computed integrals. The computed integrals of the normalized increasing (\mathcal{F}_{up}) and decreasing (\mathcal{F}_{down}) field curves around the region of the upper critical field are plotted in Fig. 3.11. The integration has been performed between limits -150 Oe and 30 Oe in the offset axis, ΔH . More explicitly

$$\mathcal{F} = \int_{-150}^{30} (ds/dH)_n d(\Delta H).$$

The error bars arise from the uncertainty in choosing H_{c2}^{up} . All temperatures refer to the T_{c2} transition, except for the two higher ones which correspond to H_{c2} . We see no systematic trend in either \mathcal{F}_{up} nor \mathcal{F}_{down} , in any of the available temperatures. In conclusion, as far as the inhomogeneity of our sample allows us to discern, there is no detectable change between the low-field H_{c2} transition and the high-field T_{c2} transition to the normal state.

End of the peak effect

We turn to the “end” of the peak effect. Its position in the phase diagram is shown in Fig. 3.10b. H_{end} occurs in a range between 32 and 39 Oe below H_{c2}^{up} . H_{end} has been identified as the field at which a continuous superconducting network which can support a macroscopic screening supercurrent forms inside the sample. We note that it occurs slightly above the midpoint of the H_0 to H_{c2}^{up} range, as shown in Fig. 3.10b. This indicates that the critical current appears when roughly half of the sample is in the mixed state while the rest is still in the normal state. This observation is very interesting but requires further investigation. The role of surface superconductivity in establishing macroscopic supercurrents in the superconducting network can be examined experimentally.

The “knee” feature

Finally we return to the newly identified “knee” feature, shown in Fig. 3.7c. From the occurrence of the knee in both ramp directions we conclude that it corresponds to an equilibrium feature of the thermodynamic behavior inside the Bragg Glass phase. To appreciate this argument, note that all three sources of irreversible and non-equilibrium effects discussed in the appendix, will induce asymmetry on the (dS/dH) curves for opposite field-ramp directions. For example, the two curves of Fig. 3.7c show asymmetry consistent with surface barrier-related heating¹ on increasing field. On the other hand, symmetric trends in the measured (ds/dH) curves have to be related to equilibrium behavior, and we thus conclude that H_{knee} corresponds to an equilibrium feature. Neutron scattering did not reveal any structural changes in the vortex lattice [4, 2] in the region of H_{knee} , which suggests that the nature of this feature is rather subtle. It would be interesting to investigate the corresponding part of the phase diagram for changes in dynamical response, as well as for a possible relation of this novel feature to the thermomagnetic instability in Nb.

3.3.2 Summary and discussion

In this work we identified the magnetocaloric signature of the peak effect on the Nb crystal previously studied with SANS and ac-susceptometry [4, 2]. The observed behavior is consistent with a previous report [99] on Nb₃Sn. Our data allow us to correlate the evolution of the peak effect with other aspects of the superconducting phase diagram of this sample.

The upper critical field had previously been proposed to consist of two distinct lines of transitions, the low field H_{c2} and high field T_{c2} [2]. In ac-susceptibility measurements there is no clear signature of T_{c2} . Our magnetocaloric measurements

¹See the discussion on irreversible and non-equilibrium effects in chapter 2.

here indicate that the low field transition from the Bragg Glass phase into the normal state (H_{c2}) is of the same nature as the high field transition between the structurally disordered [4] vortex state and the normal state (T_{c2}). The widths of both transitions do not increase with increasing field, which is indicative of inhomogeneity broadening. In magnetocaloric measurements, the peak effect disappears in the $H - T$ phase diagram at low fields, but at a field value considerably higher than that found in ac-susceptometry.

The ac-susceptibility measurement is sensitive to the screening current near the surface, which is assisted by a superconducting surface layer. Thus the simultaneous disappearance of H_{c3} and H_p in ac-susceptometry is not related to the proposed MCP. In addition, the observation of a peak effect near the sample surface with ac-susceptometry indicates that at low fields the peak effect occurs in the bulk of the sample in the isolated regions that are superconducting. The H_{on} , H_p , and H_{c2}^{av} lines in our data extrapolate to a location in close vicinity to the MCP proposed by *Park et al* [2].

Our results have strong implications for understanding the nature of the multicritical point where the peak effect disappears [2, 65, 97]. A tricritical point can be ruled out since the change in slope between the H_p and low field H_{c2} lines would lead to violation of the thermodynamic 180° rule [100, 2]. The fact that the magnetocaloric transition appears to be continuous and of the same character across both T_{c2} and H_{c2} , suggests that the critical point is bicritical. Bicriticality implies competing order parameters in the two bulk vortex phases [101, 102, 103]. In our case these are the ordered Bragg glass [33, 34], and a disordered vortex glass. The vortex glass phase is not necessarily superconducting in the sense of the original proposal [1], but it has to be a genuine phase possessing an order parameter absent in the normal state, and *in competition* with that of the Bragg glass. We will return to the vortex glass case

in the concluding chapter. Alternatively, in the absence of a MCP, the region of the phase diagram between H_p and T_{c2} may be attributed to a dirty vortex state of the Griffiths type [104, 105].

The peak effect consistently occurs slightly below T_{c2} . It is pronounced in a region where no Lowest Landau Level (LLL) fluctuation effects [13] were observed or expected. For example, at 3850 Oe the peak effect occurs more than 100 Oe below H_{c2}^{av} and 60 Oe below H_0 . These translate to distances of more than 100 mK and 60 mK on the temperature axis, far outside the LLL fluctuation region for this field [13, 15], given by $\Delta T_{fl} \approx 20$ mK. We thus attribute the peak effect in our sample to a disorder-driven order-disorder transition of the vortex lattice. In recent work, the peak effect in Nb₃Sn [18] and NbSe₂ [106] has been found to occur in the regime of strong LLL fluctuations, close to the upper critical field. We attribute the suppression of the peak effect transition temperature in our sample to increased level of disorder. The Bragg glass disordering transition, just like melting of a crystalline solid, can be thermally driven or disorder driven, with increased disorder leading to lowering of the melting temperature [107].

Chapter 4

Flux-lattice longitudinal correlation measurements at the Bragg Glass transition

4.1 Introduction

As mentioned in the first chapter, the investigation of vortex phases in type-II superconductors is interesting for understanding the behavior of these materials, as well as for studying phase transitions in the presence of disorder. The existence of liquid [108, 109, 110, 111], glass-like [1], and quasi-long range ordered (QLRO) elastic–Bragg Glass [33, 34]–vortex phases has been proposed, but their properties and extent in superconducting phase diagrams are not fully understood. In this context the peak effect anomaly [112] has fundamental importance: It is related to an underlying, order-disorder phase transition in the vortex lattice.

In neutron diffraction experiments [4], the peak effect was shown to coincide with a hysteretic order-disorder transition. Phase coexistence of ordered and disordered

vortex phases has been directly observed in the peak effect region [62] via Hall probe microscopy. Moreover, the concept of phase coexistence is useful in explaining transport anomalies in the peak effect region[63]. However, direct structural information on how a Bragg glass phase with QLRO emerges from a disordered vortex phase at the Bragg glass transition is absent.

This question is of general interest for the study of crystallization processes in the presence of disorder and frustration [113]. In studying these processes concepts from the theory of defect-mediated melting in two dimensions [114, 115, 116, 117] have been used. These processes offer a road-map for describing the processes by which a two-dimensional glassy system approaches a defect-free solid phase [118, 119]. The outcome of this effort is a general mechanism upon which the crystallization occurs via a two-step process: liquid –to hexatic-glass –to solid. This occurs in a way analogous to the crystallization of a two-dimensional solid, via the pairing-up first of disclinations and then of free dislocations in the system. These ideas also serve as a paradigm by which to study the Bragg glass transition, that is the crystallization of vortex matter. Of course, the nature of this process can be significantly more involved than the study of two-dimensional glasses due to the polymer-like nature of vortices.

Here we report a systematic study of vortex lattice correlations in the peak effect region of our niobium single crystal. The translational correlations are measured using Small Angle Neutron Scattering (SANS) rocking-curve measurements. Our measurements show that upon cooling in a magnetic field, the vortex state is disordered longitudinally (along the field direction), as well as in transverse directions as reported previously [4]. Over a wide temperature range below the peak effect, we observe coexistence of Bragg Glass with a metastable disordered phase. The longitudinal correlations grow rapidly with decreasing temperature, indicating the emergence of QLRO. However, QLRO fails to be fully established on field cooling to the lowest

temperature. With subsequent warming, the longitudinal correlations show further increase. We interpret this behavior as the gradual emergence of the Bragg Glass phase from a disordered phase; this process occurs via annealing of defects trapped in the vortex lattice.

4.2 Experimental findings

The measurements were performed at the NIST Center for Neutron Research in the configuration described in chapter 2. As mentioned earlier in rocking-curve measurements two-dimensional SANS patterns are obtained for several different values of the angle, ω , between the incident neutron beam and the flux lattice. These measure translational flux-lattice correlations in the direction of the applied magnetic field, and provide significantly higher \mathbf{q} -space resolution compared to the SANS resolution in the direction perpendicular to the magnetic field.

For our experiment the magnet cryostat was mounted on a Huber stage, allowing for precise rotation on the horizontal plane. The angle ω was varied in steps of 0.10° around the configuration where the neutron beam is parallel to the field, \mathbf{H} . All the measurements were performed at a fixed field of 4000 Oe. Data were acquired on field cooling (FC) down to 3.2 K and on subsequent field-cooled warming (FCW).

The temperature scale in these measurements has been calibrated against those used in the previous chapter and in earlier work [4]. This was done by taking advantage of the fact that in mean field the integrated intensity, $I(T)$, from any Bragg peak vanishes quadratically as the superconducting transition is approached, that is [120]

$$I(T) = I_0 \cdot (T - T_{c2}(H))^2.$$

In this expression I represents the integrated intensity of a certain Bragg peak, which is obtained by summation of the measured intensities in the region of the peak for all

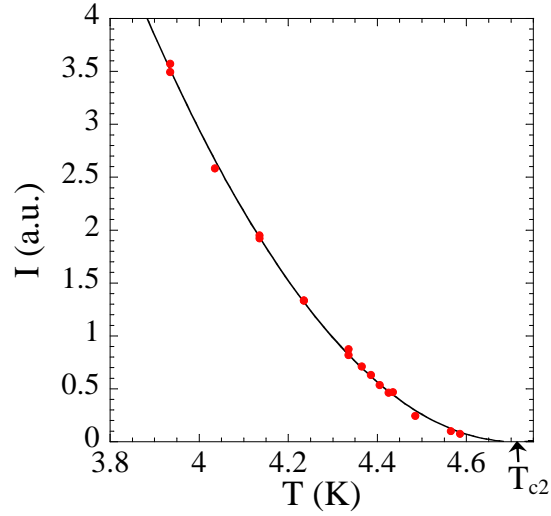


Figure 4.1: Typical integrated intensity versus temperature (red data points) and quadratic fit of the form $I = I_0 \cdot (T - T_{c2})^2$ (black line). The fit yields a $T_{c2} = 4.71$ K, in accordance with the phase diagrams in earlier work [4] and with Chapter 3. The data shown correspond to the (1,-1) peak according to the notation defined in Fig. 4.2

the different values of the rotation angle, ω . Typical data for the integrated intensity of a certain first-order Bragg peak are shown in Fig. 4.1. From the extrapolated value $T_{c2} = 4.71$ K of the fit, we define the temperature of the sample in the SANS measurements with reference to the temperature scale used earlier. We estimate the offset between the temperature scales used in previous work (in [4] and in Chapter 3) and in the present experiment to be at most 50 mK at the lowest temperature of 3.23 K used in the SANS measurements. This discrepancy has no consequences on our analysis and the conclusions we will reach, since these focus on temperature features separated by intervals of several hundred mK.

4.2.1 General features

We now proceed to present our results. A typical succession of SANS patterns is shown in Fig. 4.2. In the inset of Fig. 4.3a we also show a schematic of the scattering geometry, reproduced from Chapter 2. In Fig. 4.2, six first order Bragg peaks are

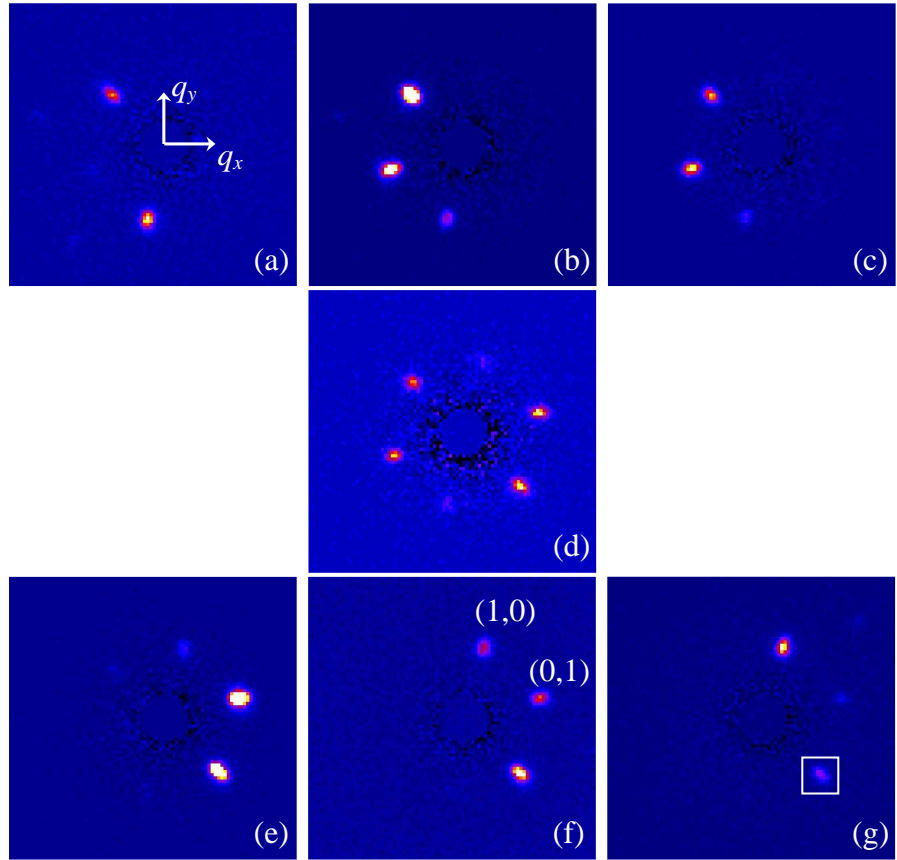


Figure 4.2: Typical succession of SANS patterns in a vortex lattice rocking curve measurement. The SANS detector lies on the xy plane. The data shown were obtained on FCW at $T = 3.35\text{ K}$, $H = 4000\text{ Oe}$. Rotation angles, left to right, are $\omega = -0.30^\circ, -0.20^\circ, -0.10^\circ, 0.00^\circ, 0.10^\circ, 0.20^\circ, 0.30^\circ$. We use the peak labeling scheme shown in (f).

present, indicating the existence of an orientationally ordered flux-line lattice. Each one of the observed peaks follows a curve of increasing and decreasing intensity as ω is changed. This is quantified by the $q_x q_y$ -integrated intensity: the sum of the intensity incident on the $q_x q_y$ detector in the region of the peak, for example inside the white frame encircling the $(-1,1)$ peak in Fig. 4.2g. The $q_x q_y q_z$ -integrated intensity (or simply the integrated intensity, as shown in Fig. 4.1) of a certain peak, at a given temperature, is determined by summation of the $q_x q_y$ -integrated intensities for the given peak, for all values of the rotation angle, ω , at that temperature.

4.2.2 Qualitative features

In Fig. 4.3a we show the $q_x q_y$ -integrated intensity versus rotation angle, of the (-1,1) Bragg peak, for different temperatures and thermal histories. We find that a good phenomenological fit to the data is a Lorentzian function, with width $\Delta\omega$

$$I(\omega) \propto 1/((\omega - \omega_0)^2 + \Delta\omega^2). \quad (4.1)$$

Sharper curves, for example a Gaussian, fail to describe the tail parts of the rocking-curve data. The $I(\omega)$ curves arising from the peaks (1,0) and (-1,0), i.e. those closest to the q_y axis, are not suitable for quantitative analysis, as they only include points on one side of the full curve and will result in underdetermined curve-fitting situations.

The Lorentzian fit results serve to summarize the qualitative behavior of flux-lattice longitudinal correlations on FC and subsequent FCW. In Fig.4.3b we show the half width $\Delta\omega$ of the Lorentzian fits performed to the data. On FC the rocking curves are wider than on FCW. Upon cooling from T_{c2} , $\Delta\omega$ decreases continuously, and the linearly extrapolated value joins the FCW branch at $T_0 \approx 3.87$ K. On FCW the half width is in the vicinity of 0.10° . Interestingly, on warming from 3.23 K, $\Delta\omega$ follows a downward trend with increasing temperature. Moreover the slope of $\Delta\omega(T)$ on the FCW branch changes slightly in the neighborhood of T_0 , as seen from the linear fits shown in Fig.4.3b. The observed behavior reveals a gradual increase of longitudinal translational order on FC, and subsequent further increase of this order on FCW. The sharpest rocking curves in the neighborhood of 4.4 K are in the resolution limit.

The hysteresis and temperature dependence in $\Delta\omega$ cannot be attributed to a demagnetization effect such as that observed in a pristine niobium crystal without the peak effect anomaly [90]. Instead, what we see is the process of vortex matter crystallization in the presence of disorder. The hysteresis is consistent with previous reports on the transverse structure function $S(q_x, q_y)$ of this Nb single crystal [4]. For

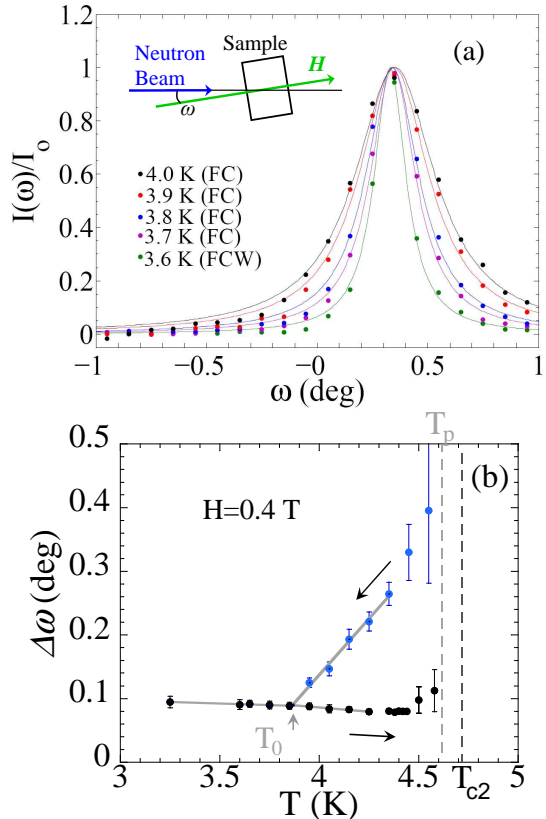


Figure 4.3: (a) Normalized intensity versus rotation angle for the (1,-1) Bragg peak at different temperatures on both FC and FCW paths. Also shown are fitted Lorentzian curves. Inset: Geometry of the rocking curve measurement. (b) Half width of Lorentzian fits to the rocking curve data. FC is in blue, FCW in black. Arrows also indicate thermal history. The locations of the peak of the peak effect (T_p) and superconducting transition (T_{c2}) are marked. Grey lines are linear fits performed on the data points within the ranges where the lines are drawn.

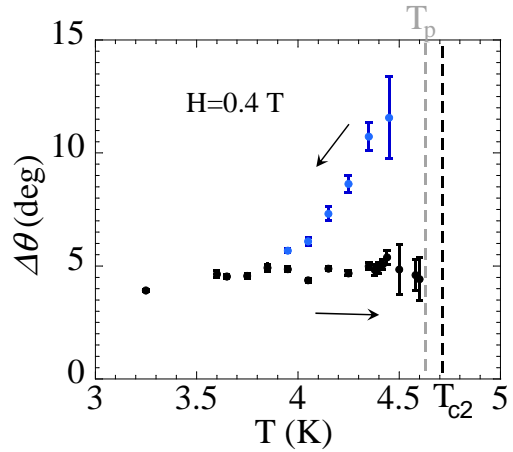


Figure 4.4: Azimuthal widths of Bragg peaks on the $q_x q_y$ plane, in agreement with Ref.[4]

example, in Fig.4.4 we show the typical behavior of a Bragg peak azimuthal width, $\Delta\theta$, on the $q_x q_y$ detector. Our findings indicate that with decreasing temperature, the increasing flux-line interactions lead to gradual enhancement of both longitudinal translational (Fig.4.3b) and orientational (Fig.4.4) flux lattice order.

4.2.3 Quantitative analysis

As explained in Chapter 2, the vortex lattice longitudinal structure function $S_z(q_z) \equiv S(\mathbf{q}_{\perp 0}, q_z)$ enters the observed rocking curve via function

$$F(\omega) = S_z(q_z = \omega q_{x0}), \quad (4.2)$$

convoluted with the instrumental resolution function. In order to extract quantitative information from the rocking-curves, the instrumental resolution function, $R(\omega)$, is needed. This can be estimated by taking into account the beam collimation and wavelength spread. The result is of the form

$$R(\omega) \propto \frac{1}{1 + \exp((|\omega| - \omega_c)/\delta)} \quad (4.3)$$

and, as mentioned in Chapter 2, has a half width which is only slightly larger than the width of the sharpest rocking curves [68]. In what follows, we assume $R(\omega)$ to be of the same form. We empirically estimate $R(\omega)$ for every pair of inversion symmetric Bragg peaks to have the half width of the sharpest rocking curve for that pair of peaks.

The convolution of the resolution function with a non-singular structure function can sufficiently describe the central part of the measured rocking curves, but not the smooth tails at larger angles. This is evident from the dashed line fit in Fig. 4.5a, where the measured curve is fitted with a Lorentzian, $L(\omega)$, convoluted with $R(\omega)$

$$I(\omega) = (L * R)(\omega). \quad (4.4)$$

We find instead, that a two-component curve of the form

$$I(\omega) = I_0 \left(f \cdot R(\omega) + (1 - f) \cdot (L * R)(\omega) \right), \quad (4.5)$$

shown as a solid line in Fig. 4.5a, provides a better fit. This curve accommodates both the resolution dominated central portion and the Lorentzian-like smooth tails of the curve. The slight asymmetry present in the rocking-curve (the left side of the curve is lower than the right side) is due to asymmetry in the neutron beam angular profile, and does not undermine our central observation that a two-component curve provides a better fit to the data.

In the two-component curve, the central, resolution limited, portion ($\propto f \cdot R(\omega)$) can be accounted for by the presence of the Bragg Glass phase, characterized by translational quasi-long range order [36]. The interpretation of the smooth rocking curve tails is less straightforward. They could arise from the behavior of the flux lattice in the so-called Larkin regime [29], which is relevant for the Bragg Glass phase on small length-scales [34]. Alternatively, the Lorentzian tails of the curves can arise from the presence of a frozen-in entangled phase [109, 110, 111]. In both cases,

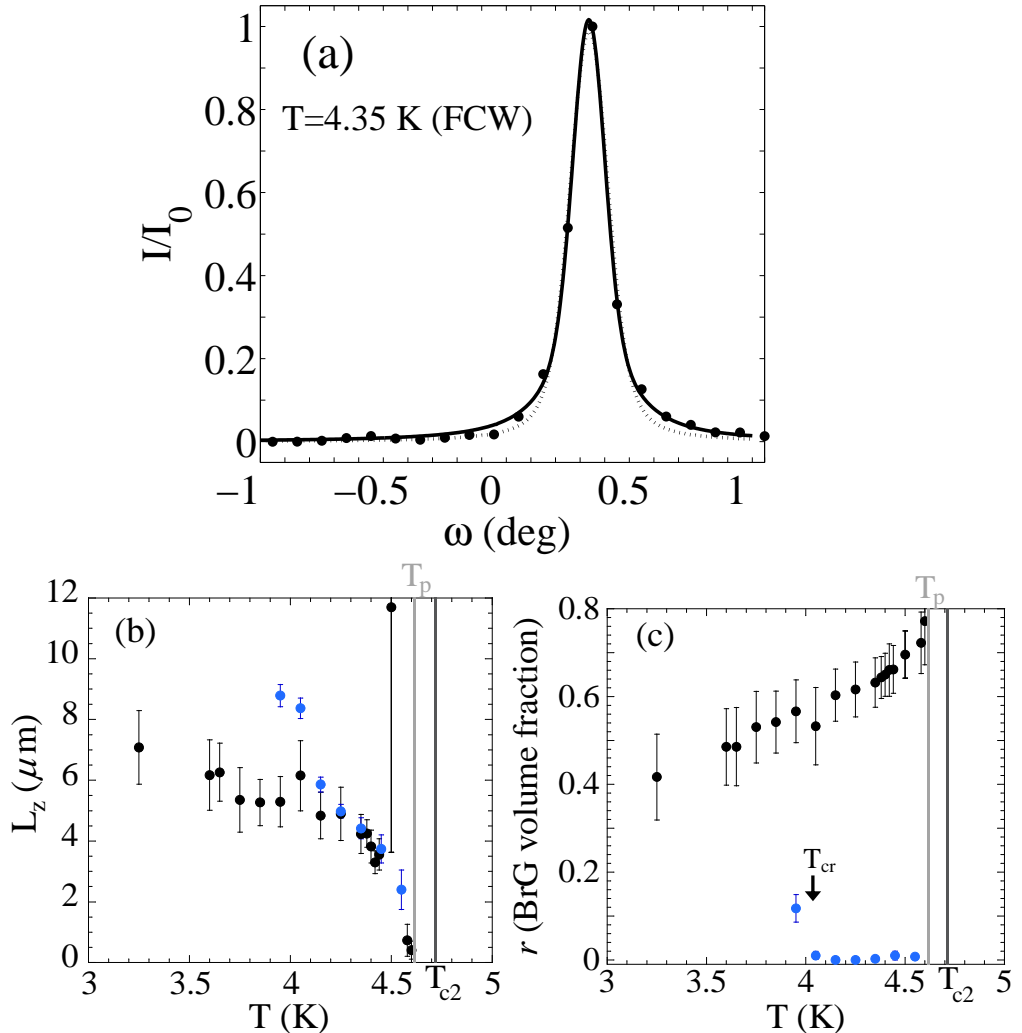


Figure 4.5: (a) Fits to a FCW rocking curve. Dashed line is a Lorentzian structure function convoluted with the resolution function. Solid line is the two-component fit. (b) Longitudinal correlation length L_z , in the disordered phase. Blue symbols: FC, black symbols: FCW. (c) Volume fraction of Bragg Glass phase in the coexistence picture, for FCW and FC paths. The values shown in (b) and (c) are averages of values obtained from four peaks, error bars are variances about the average.

the structure function is expected to be Lorentzian, hence the Lorentzian-like tail $(1 - f) \cdot (L * R)(\omega)$.

A Lorentzian component in the structure function implies exponential decay of the flux-line lattice correlation function

$$C_{Q_0}(z) = \langle e^{i \mathbf{Q}_0 \cdot (\mathbf{u}(z) - \mathbf{u}(0))} \rangle \propto e^{-z/L_z}, \quad (4.6)$$

with longitudinal correlation length L_z . The width Δ of the Lorentzian component

$$L(\omega) \propto \frac{1}{(\omega - \omega_0)^2 + \Delta^2}, \quad (4.7)$$

allows us to determine the correlation length. For a Bragg peak located at $(Q_{0,x}, Q_{0,y})$ this is

$$L_z = (\Delta \cdot Q_{0,x})^{-1}. \quad (4.8)$$

In Fig. 4.5b we show the L_z value obtained as the average of the values determined from the first order Bragg peaks, excluding (1,0) and (-1,0) for the reason mentioned earlier. Error bars are variances about the average. We find that the correlation length lies in the $2\text{-}9 \mu\text{m}$ range. On FC, it shows a roughly linear increase from zero, with decreasing temperature. The temperature variation on FCW is weaker, and the value varies between 3 and 7 μm .

We argue that the origin of the Lorentzian rocking-curve component is a metastable entangled phase. In the spirit of the analysis performed by Nelson and Marchetti [111], this phase is characterized by trapped screw dislocations which disrupt longitudinal order, but not the transverse orientational order. We can justify the conclusion that screw dislocations are responsible for the Lorentzian broadening, solely on qualitative grounds: The rocking-curve width for FC at some temperature between T_0 and T_{c2} (*cf.* Fig. 4.3b) is considerably larger than the width on the FCW branch, at the same temperature. In the absence of dislocations, the flux-line interactions, pinning strength, and effect of thermal fluctuations at the given temperature would be the

same for both branches, and the rocking-curve width would have to be the same. Consequently, the observed hysteresis in the extent of longitudinal correlations has to be related to the presence of trapped screw dislocations on the FC branch.

We can further justify this conclusion by estimating the effect of random point-pinning on the structural properties of the flux lattice. We then find that the measured L_z values imply the existence of significant amounts of frozen-in flux lattice defects which disrupt translational quasi-long range order in the flux-line lattice. We estimate the longitudinal correlation length arising due to collective pinning in the short length scale, Larkin, regime. Following the notation of Blatter *et al.* [121], the flux-line displacement field follows

$$\langle (u(z) - u(0))^2 \rangle = z \frac{\gamma_U}{(2\pi^2 \lambda \alpha_0 c_{66} \sqrt{(c_{44} c_{66})})} \equiv z \cdot \ell. \quad (4.9)$$

Here dispersionless elastic constants, c_{44} , c_{66} , can be used, and $\gamma_U \propto \langle \delta T_c^2 \rangle / T_c^2$ characterizes the strength of “ δT_c ” pinning. For our sample we have previously determined (*cf.* Chapter 2) the upper critical field and κ , which allow us to calculate the elastic moduli [30] and penetration depth λ in Eq. 4.9. Using the measured transition width $\delta T_c \approx 80$ mK we approximate the T_c distribution by a Gaussian of mean $T_{c0} \approx 9$ K and standard deviation $\sigma_T \approx 35$ mK, i.e. a probability distribution for T_c : $p(T_c) = \frac{1}{\sqrt{\pi}\sigma_T} e^{-(T_c - T_{c0})^2/\sigma_T^2}$. We thus obtain the value $g \equiv \langle \delta T_c^2 \rangle / T_c^2 \approx 3 \times 10^{-5}$. This allows us to estimate the pinning strength parameter by [121]

$$\gamma_U \approx 30\pi g \left(\frac{H_c^2}{4\pi} \right)^2. \quad (4.10)$$

To proceed further, we rewrite the correlation function, Eq. 4.6

$$C_{Q_0}(z) = \langle e^{i\mathbf{Q}_0 \cdot \mathbf{u}(z)} \rangle, \quad (4.11)$$

by setting $\mathbf{u}(0) = 0$. If the statistical weight of the displacement field is Gaussian, the correlation function in the vicinity of reciprocal lattice point \mathbf{Q}_0 can be written

[109]

$$C_{Q_0}(z) = e^{-\frac{1}{2}\langle(\mathbf{Q}_0 \cdot \mathbf{u}(z))^2\rangle}. \quad (4.12)$$

Now we can use the fact that

$$\langle(\mathbf{Q}_0 \cdot \mathbf{u}(z))^2\rangle = Q_0^2 \langle u^2(z) \cdot \cos^2 \theta_{[\mathbf{Q}_0, \mathbf{u}]} \rangle = \frac{1}{2} Q_0^2 \langle u^2(z) \rangle. \quad (4.13)$$

Finally, by use of the collective pinning result Eq. 4.9, one arrives at

$$C_{Q_0}(z) \propto e^{-\frac{1}{4}Q_0^2 \ell \cdot z}. \quad (4.14)$$

As a result the structure function is a Lorentzian

$$S(q_z) \propto \frac{1}{(q_z^2 + (\frac{1}{4}Q_0^2 \ell)^2)}, \quad (4.15)$$

which yields $L_z = \alpha_0^2 / (\pi^2 \ell)$. By using this result and Eq. 4.9 we estimate $L_z \approx 200 \mu\text{m}$ at field of 4000 Oe and temperatures in the range between 3 and 4 K.

The estimated value is significantly larger than the measured one. Even in the case of non- δT_c pinning, such as atomic lattice defects and strain fields acting in addition to the impurity related pinning of our calculation, these mechanisms are unlikely to account for the discrepancy by a factor of 20 between the two results. Therefore we consider unlikely the crossover to the Larkin regime as the source of the two-component rocking curve results.

Instead, we attribute the reduced extent of longitudinal flux-line correlations to the presence of a supercooled, disordered vortex phase. In this phase the short longitudinal correlations are caused by entanglement, i.e. presence of trapped screw dislocations, as proposed by Nelson [108, 109, 110, 111]. The disordered phase also contains frozen-in edge dislocations and disclinations. These defects disrupt the translational and orientational order on larger scales, leading to the behavior reported by Ling *et al.* and observed here. The gradual sharpening of the rocking-curves in Fig. 4.3b is the result of *phase coexistence* in the flux-lattice obtained on field cooling:

The Bragg Glass phase starts to crystallize with decreasing temperature, but it occupies only a fraction of the flux lattice volume. This fraction is expected to increase as the temperature is lowered below the peak effect.

The extent of each phase present in the system is proportional to the integrated intensity of the corresponding component of the measured rocking curve. Thus we determine the fraction of Bragg Glass phase as

$$r \equiv \frac{\int f \cdot R(\omega) d\omega}{\int [f \cdot R(\omega) + (1 - f) \cdot (L * R)(\omega)] d\omega}. \quad (4.16)$$

The results are plotted in Fig. 4.5c. On FC the fraction of Bragg Glass phase remains undetectable down to approximately $T_{cr} = 4.0$ K. Subsequently, the Bragg Glass phase starts to nucleate, and its volume fraction increases to $r \approx 0.4$ at 3.23 K. Thus, the flux lattice obtained after FC down to 3.23 K has been only partly transformed to the Bragg Glass phase. Upon FCW from 3.23 K, the Bragg Glass fraction increases linearly with temperature, giving rise to the observed sharpening of the rocking curves, Fig. 4.3b.

4.3 The process of Bragg Glass crystallization

We are now in a position to examine the process by which the disordered phase anneals on FC. In Fig. 4.4, we show that the Bragg peak azimuthal width decreases continuously with temperature. This process has to be interaction driven. It occurs as increasing flux-line interactions cause flux lattice defects to anneal. In the same range, the longitudinal correlation length increases from 2 to 8 μm , due to elasticity driven annealing of screw dislocations. On FC to 4.0 K, the azimuthal width is slightly higher than the instrumental resolution limit, and corresponds to a bond-angle spread of 1° over 40000 vortex spacings. The range of longitudinal correlations is much more limited, $L_z \approx 8 \mu\text{m}$, corresponding to approximately 100 vortex spacings. These

structural properties of the supercooled disordered phase in the neighborhood of 4.0 K reaffirm early observations of a hexatic glass [122, 123]. Therefore, the state obtained on FC from above T_p can be described as a hexatic glass. Upon cooling between T_p and T_{cr} , the only change that occurs is that the longitudinal correlation length L_z and the transverse bond-angle correlation length (ξ_6) increase in a continuous manner, leading to the observed behavior.

Below $T_{cr} = 4.0$ K, the hexatic phase becomes unstable. As a result Bragg Glass nucleates from the hexatic glass phase, as indicated by the abrupt increase of r in Fig. 4.5c. Although Bragg Glass starts to crystallize, an amount of frozen-in entangled phase remains in the system, and the Bragg Glass phase can only get further established upon subsequent warming. The reason for this is that the interaction-driven ordering has limited effectiveness in annealing flux lattice defects. As the temperature decreases below T_{c2} the vortex-line crossing energy increases [124], which means that screw dislocations become harder to anneal. As a result, the metastable, entangled hexatic phase can be supercooled far beyond the temperature T_{cr} , at which Bragg Glass starts to crystallize. Thus, the field-cooled flux lattice at 3.23 K contains only a fraction $r \approx 0.4$ of Bragg Glass phase. Nevertheless, once the thermodynamically stable Bragg Glass phase has started to nucleate, it can be assumed to be more effective in annealing screw dislocations than the hexatic glass. As a result, on FCW from 3.23 K the Bragg Glass fraction increases considerably. This counter-intuitive behavior is due to the fact that the decrease in vortex cutting energy as the upper critical field is approached, assists in annealing of screw dislocations.

The fact that the Bragg glass fraction keeps increasing on FCW between T_{cr} and T_p indicates that the hexatic phase observed to exist on FC between these temperatures is only metastable. This is in agreement with the picture of the Bragg glass transition being located at the peak of the peak effect. A puzzling feature of this conclusion is

that the phase transition, occurring at T_p , is at the higher end of the temperature range where the hexatic glass exists, in contrast to the usual two-dimensional melting scenario. However, it is important to note that the major type of defect probed in our longitudinal correlation measurements are screw dislocations, which are entirely absent in a two-dimensional system. Thus, the hexatic glass found in flux lattices is rather different from the one envisioned by studies of two-dimensional glasses. The main open question in this work is what mechanism drives annealing of screw dislocations and makes them highly unstable below T_{cr} .

4.4 Summary

We performed structural measurements in a vortex lattice thermally cycled through the Bragg Glass transition. Our results indicate coexistence of Bragg Glass with the metastable disordered phase, over a large region below the peak of the peak effect. Both orientational and translational order are argued to proceed via interaction-driven annealing of flux-lattice defects. We find that orientational order is established considerably faster than translational order, giving rise to a metastable hexatic glass. The Bragg Glass phase nucleates out of the latter, but fails to be fully established on field cooling. Nevertheless, on warming from a partially equilibrated Bragg Glass phase, quasi-long-range order emerges.

In the next chapter we will try to incorporate the new knowledge reported thus far in the framework of vortex phases, phase transitions, and the peak effect phase diagram.

Chapter 5

Conclusions

5.1 Introduction

In the previous chapters we presented experimental work performed on a niobium single crystal displaying the peak effect anomaly in the critical current. We repeat here previous findings on the same sample for completeness. It was studied by the Brown-NIST collaboration using Small Angle Neutron Scattering and simultaneous *in situ* ac-susceptometry [4]. This revealed a hysteretic symmetry-breaking transition of the flux lattice, between an orientationally and translationally disordered phase above the peak of the peak effect and an ordered hexagonal vortex lattice below the peak of the peak effect. This ordered phase was interpreted as the Bragg glass phase, since it gives rise to resolution limited neutron diffraction peaks. The hysteretic behavior was taken to be the result of supercooling and superheating due to the first order nature of the phase transition between Bragg glass and the disordered phase. The nature of this disordered phase, pinned vortex liquid or vortex glass remained undetermined.

The hysteresis in the structure factor was absent in a later report of SANS measurements by the Birmingham-ILL collaboration on a different niobium single crystal of very high purity *without* the peak effect [90].

This motivated further work by the Brown group on the same crystal used in their earlier work [2]. Careful ac-susceptibility measurements traced the evolution of the peak effect on the $H - T$ phase diagram. It was shown that the peak effect is absent at low dc H fields, and appears in the vicinity of 900 Oe. It then progressively gets more pronounced as H is increased. The hysteresis in the structure factor also disappeared at low fields. It was thus concluded that the first order transition is tied to the peak effect, and terminates when the peak effect terminates.

Moreover, it was found that the peak effect line terminates on the upper critical field H_{c2} line, where the surface superconductivity line H_{c3} also terminates. This striking observation raised the possibility of a multicritical point related to the disappearance of the peak effect. This would be bicritical if the disordered phase was a real phase separated from the normal phase by the H_{c2} transition. It would be a tricritical point if the H_{c2} line was just a crossover between the normal phase and a vortex liquid, which would in turn be separated from Bragg glass by the peak effect transition.

5.2 Insight from Magnetocalorics

The magnetocaloric measurements described in chapter 3 shed some light into the nature of the effects taking place in the vicinity of the peak effect and of H_{c2} . They revealed that the superconducting transition of the studied sample shows inhomogeneity broadening of the order of 80 mK. This is large enough that no broadening of the transition due to Lowest Landau Level scaling was observed up to fields of 4000 Oe, in neither magnetocalorics nor calorimetry. The location of the peak effect was traced in magnetocalorics. In agreement with the ac-susceptometry report by Park *et al.*, we found that the peak effect approaches the upper critical field as the temperature is increased.

Nevertheless the bulk peak effect, to which the magnetocaloric technique is sensitive, is only present when the entire sample is superconducting: In other words, it only occurs outside of the inhomogeneity broadened H_{c2} transition. Clearly then, the peak effect occurs far outside the range of significant lowest Landau level (LLL) fluctuations. This can be understood as the suppression of the Bragg glass transition temperature by disorder. One can see this schematically by a Lindemann-type argument. The transition in the pure system will occur when the thermal wandering of a flux line is a fraction of the lattice spacing $\langle u^2 \rangle \approx c_L^2 a^2$, with some constant $c_L \sim 0.1 - 0.3$. In the presence of quenched disorder, one can estimate the new transition temperature by adding the thermal wandering in the clean system ($\langle u^2 \rangle$) to the disorder induced wandering in the absence of thermal fluctuations ($\overline{u^2}$)

$$\langle u^2 \rangle + \overline{u^2} \approx c_L a^2.$$

Thus, the transition temperature in the presence of disorder will be suppressed.

The report on this niobium crystal of the peak effect outside the strong fluctuation region is significant in view of recent reports of peak effects in the regime of strong thermal fluctuations [18, 106]. Our finding suggests that in the more general case, the peak effect will occur outside the region of strong LLL thermal fluctuations. Thus, treatments of vortex lattice melting in the clean system such as the excellent work of Li and Rosenstein [15] have limited value in elucidating the peak effect transition.

The magnetocaloric measurement addresses some of the issues raised in the work of Park *et al.* We observed the disappearance of the bulk peak effect in magnetocalorics at fields $H \approx 1700$ Oe, significantly higher than the field of ≈ 900 Oe reported by ac-susceptometry. The absence in our measurements of a bulk peak effect inside the broadened upper critical field transition led us to conclude that the observation of the peak effect for $900\text{ Oe} < H < 1700\text{ Oe}$ in ac susceptometry is an artifact of the technique: The peak effect appears in ac-susceptometry by local screening near the

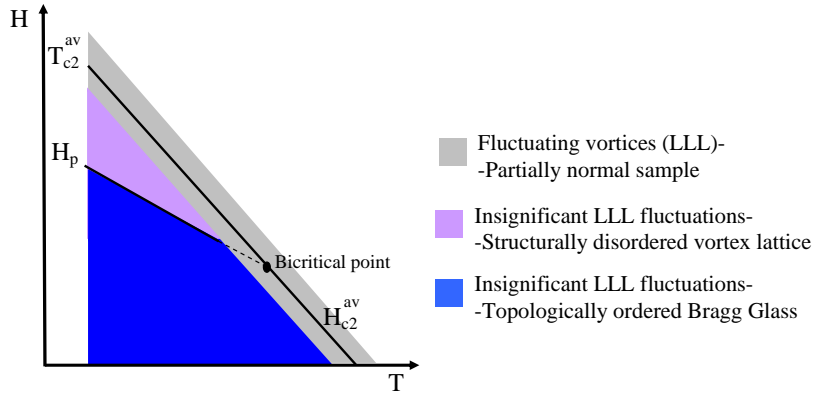


Figure 5.1: Schematic of the phase $H - T$ phase diagram of the niobium single crystal used in this work. Three distinct regions are designated: The grey region corresponds to the formation of a vortex lattice. In it, Lowest Landau Level fluctuation effects are significant but not the sole significant factor, since normal regions still exist in the sample. The purple region has insignificant fluctuation effects, i.e. vortices are well formed in this region. In this region the equilibrium vortex lattice is structurally disordered. The blue region is a Bragg glass with insignificant fluctuation effects. The Meissner phase is not shown, for simplicity.

sample surface; this is assisted by surface superconductivity and thus the simultaneous disappearance of the H_{c3} line and the peak effect is an artifact of ac susceptometry.

The phase diagram arising from these observations is illustrated schematically in Fig. 5.1. We use the notation of Park *et al.* (introduced in chapter 3) for the superconducting transitions at high (T_{c2}) and low (H_{c2}) fields. We see that the inhomogeneity broadened transition occupies a band (the grey region) on the $H - T$ plane, separating the normal from the superconducting part. The superconducting part is divided into two phases: the ordered Bragg glass (in blue) below the H_p line, and the mysterious structurally disordered phase (shown in purple) above it. We focus on this purple region. A very important result from the magnetocaloric measurement is that this region has insignificant Lowest Landau Level fluctuations of the order parameter amplitude. Thus well formed, stable vortices are present in the sample in this region, and they form a structurally disordered lattice. This observation substantiates the earlier proposal [2] that the structurally disordered region could be a vortex glass

phase, and indicates a way to a theoretical treatment of the problem: one can neglect the order parameter amplitude fluctuations and ask whether the pinned vortex lattice arising in this purple region can have superconducting phase coherence. If yes, this phase is a vortex glass with vanishingly small ohmic resistivity.

Experimentally one has to devise a way to test some of the expected vortex glass characteristics on the niobium sample. The simplest possibility would be frequency-dependent, ultra low-frequency ac-susceptometry. Such a setup would allow one to test the frequency-dependent scaling of resistivity proposed in the Fisher-Fisher-Huse proposal [1]. Alternatively one could perform an inductive flux-relaxation measurement [125]. A simple calculation shows that such a measurement using a pick-up coil of 1000 turns and having voltage sensitivity of 10 nV would provide sensitivity of 1 mG/sec in measuring magnetic induction changes. As discussed in [1], to distinguish between a vortex glass and a pinned liquid of the Anderson-Kim type [41], one would need the ability to detect changes in flux relaxation rates over a wide range of temperatures. Since this measurement also has to be performed in the region above the peak of the peak effect, this measurement would have to be done in fields as high as 6000 Oe and temperatures as low as 1 K , a currently unexplored part of the phase diagram of the niobium sample.

The description of the “purple” phase as a vortex glass will have, as already mentioned, significant consequences on the nature of the critical point: If the disordered phase is a vortex glass, the critical point has to be bicritical. The phase diagram will then consist of three thermodynamically distinct phases: Bragg Glass, vortex glass and normal metal. In addition, bicriticality would suggest competition between the topological ordering of Bragg Glass and the off-diagonal long range order in the vortex glass.

5.3 Insight from SANS rocking-curve measurements

The quantitative analysis of the SANS rocking-curve measurements presented in the previous chapter uncovers very exciting features of both the structurally disordered state above H_p and the process of Bragg glass crystallization. The structural hysteresis of the transverse structure function, $S_{\perp}(q_x, q_y)$, reported earlier by Ling *et al.* [4], is present in the longitudinal structure function, $S_{\parallel}(q_z)$, as well.

Upon in-field cooling from the normal state the disordered vortex lattice displays exponential decay of longitudinal correlations. The correlation length is approximately $2 \mu\text{m}$ or less in the immediate vicinity of the H_{c2} transition. As the temperature is decreased further below H_{c2} , the disordered phase evolves into a metastable hexatic glass phase, in which both the longitudinal correlation length (L_z) and the bond-angle correlation length (ξ_6) increase on cooling. The vortex lattice for this temperature range and thermal history contains a large amount of trapped defects. These are both edge and screw dislocations and they disrupt translational order in the transverse and longitudinal directions respectively.

Below a certain temperature T_{cr} , the topologically ordered Bragg Glass phase starts to nucleate from the hexatic glass. Nevertheless, screw dislocations are hard to anneal due to the high energy barrier for vortex crossing at temperatures $T < T_{cr}$. As a result, the Bragg glass phase is only partially established even upon cooling by more than one degree below the superconducting transition. This situation could, in principle, persist all the way down to zero temperature. Hence, once Bragg Glass has started to nucleate below T_{cr} the most efficient way to further anneal the vortex lattice is by increasing the temperature towards T_{c2} . This leads to decrease of the vortex-cutting energy barrier, and the Bragg Glass very effectively anneals trapped screw dislocations on increasing temperature.

It is very tempting to propose a mechanism for the emergence of the entangled

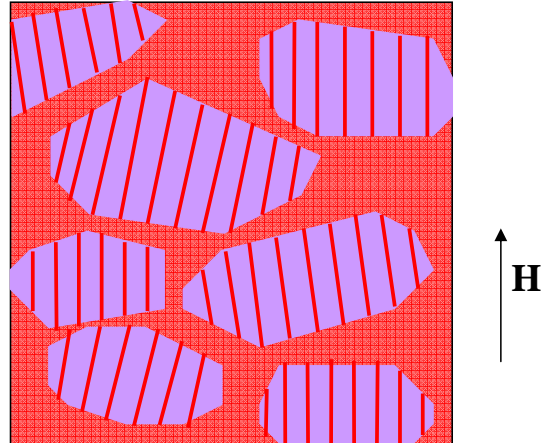


Figure 5.2: Schematic representation of the process by which the vortex lattice formation proceeds in our niobium single crystal. We show a snapshot of the system in the temperature region where parts of the sample are still normal (red regions). The vortex lines (also in red) inside the superconducting grains (in purple) are tilted with respect to the applied field due to geometric factors and pinning. This process naturally leads to formation of vortex lattice defects upon cooling, in the regions where the domains join each other.

phase on field-cooling at 4000 Oe based on the knowledge obtained from the magnetocaloric measurement. A key finding is that the range of inhomogeneity broadening of the superconducting transition is significantly larger than the fluctuation range at dc field of 4000 Oe. Thus, for temperatures in the grey region of Fig. 5.1 fairly stable (i.e. not wildly fluctuating) vortices have formed in superconducting islands, while other parts of the sample are still normal. The orientation of vortices in the superconducting islands is tilted with respect to the applied field, due to geometric factors and pinning. This situation is depicted in Fig. 5.2. Clearly as T is lowered, the merging of neighboring superconducting islands with tilted vortex lattices will introduce defects in the forming vortex lattice. Once the entire sample has gone superconducting and this process has completed, the largest concentrations of defects will occur in the regions in which the superconducting islands merged last, i.e. the regions of lowest T_c . Thus, the disordered, entangled lattice which we observe on the

field-cooling measurements is formed. This lattice does not anneal to a more ordered state because the equilibrium phase above the peak of the peak effect is strongly pinned.

In this context it is useful to return to transverse structure function measurements at applied field of 2000 Oe by Park *et al.* [2]. These measurements did not show any structural hysteresis, although a peak effect was present. This was unexpected given that the hysteresis at higher field extended to temperatures of about 1 K below the peak effect. Our current understanding allows us to resolve this mystery. At 2000 Oe the peak effect occurs exactly at the lower end of the superconducting transition (H_0 in chapter 3). This means that the disordered, entangled state formed on field-cooling becomes thermodynamically unstable to Bragg Glass at a temperature where certain regions of the sample are still undergoing strong LLL fluctuations. These are the regions of the lowest T_c and they are actually the same regions where the highest concentration of defects has formed. But since strong thermal fluctuations make the vortices in these regions “soft”, the defects anneal easily and the Bragg Glass phase is established with minor supercooling effects.

With these last observations we close our concluding chapter. We summarized our two sets of experiments that advanced current understanding of the peak effect and the peak-effect phase diagram. The magnetocaloric measurements allowed us to evaluate the significance (or lack thereof) of surface superconductivity for the peak effect problem. In addition they led us to reevaluate the importance of thermal fluctuations in relation to the location of the peak effect and the sample inhomogeneities. The neutron diffraction experiments revealed a very fascinating picture of Bragg Glass crystallization. In combination with the knowledge provided by the magnetocaloric measurements they could offer a better explanation for the rather intricate phenomenology of the peak effect.

Bibliography

- [1] Daniel S. Fisher, Matthew P. A. Fisher, and David A. Huse. Thermal fluctuations, quenched disorder, phase transitions, and transport in type-II superconductors. *Physical Review B*, 43(1):130–159, Jan 1991.
- [2] S. R. Park, S. M. Choi, D. C. Dender, J. W. Lynn, and X. S. Ling. Fate of the Peak Effect in a Type-II Superconductor: Multicriticality in the Bragg-Glass Transition. *Physical Review Letters*, 91(16):167003, Oct 2003.
- [3] S. S. Banerjee, N. G. Patil, S. Ramakrishnan, A. K. Grover, S. Bhattacharya, P. K. Mishra, G. Ravikumar, T. V. Chandrasekhar Rao, V. C. Sahni, M. J. Higgins, C. V. Tomy, G. Balakrishnan, and D. Mck. Paul. Re-entrant peak effect in an anisotropic superconductor 2H-NbSe₂: Role of disorder. *Europhysics Letters (EPL)*, 44(1):91–97, 1998.
- [4] X. S. Ling, S. R. Park, B. A. McClain, S. M. Choi, D. C. Dender, and J. W. Lynn. Superheating and Supercooling of Vortex Matter in a Nb Single Crystal: Direct Evidence for a Phase Transition at the Peak Effect from Neutron Diffraction. *Physical Review Letters*, 86(4):712–715, Jan 2001.
- [5] M. Tinkham. *Introduction to superconductivity*. McGraw-Hill, New York, second edition, 1996.

- [6] P. G. deGennes. *Superconductivity of metals and alloys*. W. A. Benjamin Inc., New York, Amsterdam, 1966.
- [7] H. F. Hess, R. B. Robinson, R. C. Dynes, J. M. Valles, and J. V. Waszczak. Scanning-Tunneling-Microscope Observation of the Abrikosov Flux Lattice and the Density of States near and inside a Fluxoid. *Physical Review Letters*, 62(2):214–216, Jan 1989.
- [8] A. A. Abrikosov. On the Magnetic Properties of Superconductors of the Second Group. *Soviet Physics JETP*, 5, 1957.
- [9] L. D. Landau. *The collected papers of L. D. Landau*. Gordon and Breach-Pergamon, New York, 1965.
- [10] B. I. Halperin, T. C. Lubensky, and Shang-keng Ma. First-Order Phase Transitions in Superconductors and Smectic-*A* Liquid Crystals. *Physical Review Letters*, 32(6):292–295, Feb 1974.
- [11] E. Brézin, D. R. Nelson, and A. Thiaville. Fluctuation effects near H_{c2} in type-II superconductors. *Physical Review B*, 31(11):7124–7132, Jun 1985.
- [12] A. Houghton, R. A. Pelcovits, and A. Sudbø. Flux lattice melting in high- T_c superconductors. *Physical Review B*, 40(10):6763–6770, Oct 1989.
- [13] D. J. Thouless. Critical Fluctuations of a Type-II Superconductor in a Magnetic Field. *Physical Review Letters*, 34(15):946–949, Apr 1975.
- [14] G. J. Ruggeri and D. J. Thouless. Perturbation series for the critical behaviour of type II superconductors near H_{c2} . *Journal of Physics F*, 6, 1976.

- [15] Dingping Li and Baruch Rosenstein. Supercooled vortex liquid and quantitative theory of melting of the flux-line lattice in type-II superconductors. *Physical Review B*, 70(14):144521, 2004.
- [16] S. P. Farrant and C. E. Gough. Measurement of the Fluctuation Heat Capacity of Niobium in a Magnetic Field. *Physical Review Letters*, 34(15):943–946, Apr 1975.
- [17] A. Schilling, R. A. Fisher, N. E. Phillips, U. Welp, W. K. Kwok, and G. W. Crabtree. Anisotropic Latent Heat of Vortex-Lattice Melting in Untwinned $\text{YBa}_2\text{Cu}_3\text{O}_{7-\delta}$. *Physical Review Letters*, 78(25):4833–4836, Jun 1997.
- [18] R. Lortz, F. Lin, N. Musolino, Y. Wang, A. Junod, B. Rosenstein, and N. Toyota. Thermal fluctuations and vortex melting in the Nb_3Sn superconductor from high resolution specific heat measurements. *Physical Review B*, 74(10):104502, 2006.
- [19] Gert Eilenberger. Thermodynamic Fluctuations of the Order Parameter in Type-II Superconductors near the Upper Critical Field H_{c2} . *Physical Review*, 164(2):628–635, Dec 1967.
- [20] H. C. Kao, B. Rosenstein, and J. C. Lee. Systematic low-temperature expansion in the Ginzburg-Landau model. *Physical Review B*, 61(18):12352–12360, May 2000.
- [21] A. Schilling, U. Welp, W. K. Kwok, and G. W. Crabtree. Vortex-lattice melting in untwinned $\text{YBa}_2\text{Cu}_3\text{O}_{7-\delta}$ for $H \perp c$. *Physical Review B*, 65(5):054505, Jan 2002.

- [22] Neil Overend, Mark A. Howson, and Ian D. Lawrie. 3D X-Y scaling of the specific heat of $\text{YBa}_2\text{Cu}_3\text{O}_{7-\delta}$ single crystals. *Physical Review Letters*, 72(20):3238–3241, May 1994.
- [23] Mark A. Howson, Ian D. Lawrie, and Neil Overend. Howson, Lawrie, and Overend Reply:. *Physical Review Letters*, 74(10):1888, Mar 1995.
- [24] N. Overend, M. A. Howson, and I. D. Lawrie. Overend, Howson, and Lawrie Reply:. *Physical Review Letters*, 75(9):1870, Aug 1995.
- [25] M. Roulin, A. Junod, and J. Muller. Comment on 3D X-Y Scaling of the Specific Heat of $\text{YBa}_2\text{Cu}_3\text{O}_{7-\delta}$ Single Crystals. *Physical Review Letters*, 75(9):1869, Aug 1995.
- [26] Stephen W. Pierson, J. Buan, B. Zhou, C. C. Huang, and Oriol T. Valls. Comment on 3D X-Y Scaling of the Specific Heat of $\text{YBa}_2\text{Cu}_3\text{O}_{7-\delta}$ Single Crystals. *Physical Review Letters*, 74(10):1887, Mar 1995.
- [27] A. I. Larkin. Effect of inhomogeneities on the structure of the mixed state of superconductors. *Soviet Physics JETP*, 31, 1970.
- [28] Yoseph Imry and Shang-keng Ma. Random-Field Instability of the Ordered State of Continuous Symmetry. *Physical Review Letters*, 35(21):1399–1401, Nov 1975.
- [29] A. I. Larkin and Y. N Ovchinnikov. Pinning in type II superconductors. *Journal of Low Temperature Physics*, 34, 1979.
- [30] E. H. Brandt and U. Essman. The Flux-Line Lattice in Type-II Superconductors. *Physica Status Solidi (b)*, 144, 1987.

- [31] D. K. Christen, F. Tasset, S. Spooner, and H. A. Mook. Study of the intermediate mixed state of niobium by small-angle neutron scattering. *Physical Review B*, 15(9):4506–4509, May 1977.
- [32] D. K. Christen, H. R. Kerchner, S. T. Sekula, and P. Thorel. Equilibrium properties of the fluxoid lattice in single-crystal niobium. II. small-angle neutron-diffraction measurements. *Physical Review B*, 21(1):102–117, Jan 1980.
- [33] Thomas Nattermann. Scaling approach to pinning: Charge density waves and giant flux creep in superconductors. *Physical Review Letters*, 64(20):2454–2457, May 1990.
- [34] Thierry Giamarchi and Pierre Le Doussal. Elastic theory of pinned flux lattices. *Physical Review Letters*, 72(10):1530–1533, Mar 1994.
- [35] Jean-Philippe Bouchaud, Marc Mézard, and Jonathan S. Yedidia. Variational theory for disordered vortex lattices. *Physical Review Letters*, 67(27):3840–3843, Dec 1991.
- [36] T. Klein, I. Journaud, S. Blanchard, J. Marcus, R. Cubitt, T. Giamarchi, and P. LeDoussal. A Bragg glass phase in the vortex lattice of a type II superconductor. *Nature*, 413, Sep 2001.
- [37] John Bardeen and M. J. Stephen. Theory of the Motion of Vortices in Superconductors. *Physical Review*, 140(4A):A1197–A1207, Nov 1965.
- [38] C. P. Bean. Magnetization of Hard Superconductors. *Physical Review Letters*, 8(6):250–253, Mar 1962.
- [39] Charles P. Bean. Magnetization of High-Field Superconductors. *Reviews of Modern Physics*, 36(1):31–39, Jan 1964.

- [40] P. W. Anderson. Theory of Flux Creep in Hard Superconductors. *Physical Review Letters*, 9(7):309–311, Oct 1962.
- [41] P. W. Anderson and Y. B. Kim. Hard Superconductivity: Theory of the Motion of Abrikosov Flux Lines. *Reviews of Modern Physics*, 36(1):39–43, Jan 1964.
- [42] J. S. Langer and Michael E. Fisher. Intrinsic Critical Velocity of a Superfluid. *Physical Review Letters*, 19(10):560–563, Sep 1967.
- [43] J. S. Langer and Vinay Ambegaokar. Intrinsic Resistive Transition in Narrow Superconducting Channels. *Physical Review*, 164(2):498–510, Dec 1967.
- [44] R. H. Koch, V. Foglietti, W. J. Gallagher, G. Koren, A. Gupta, and M. P. A. Fisher. Experimental evidence for vortex-glass superconductivity in Y-Ba-Cu-O. *Physical Review Letters*, 63(14):1511–1514, Oct 1989.
- [45] D. R. Strachan, M. C. Sullivan, P. Fournier, S. P. Pai, T. Venkatesan, and C. J. Lobb. Do Superconductors Have Zero Resistance in a Magnetic Field? *Physical Review Letters*, 87(6):067007, Jul 2001.
- [46] N. Akino and J. M. Kosterlitz. Domain wall renormalization group study of the XY model with quenched random phase shifts. *Physical Review B*, 66(5):054536, Aug 2002.
- [47] Peter Olsson. Vortex glass transitions in disordered three-dimensional XY models: Simulations for several different sets of parameters. *Physical Review B*, 72(14):144525, 2005.
- [48] M. A. R. Le Blanc and W. A. Little. Proceedings of the VII International Conference on Low Temperature Physics. Toronto, 1960), pages=198. University of Toronto Press.

- [49] T. G. Berlincourt, R. R. Hake, and D. H. Leslie. Superconductivity at High Magnetic Fields and Current Densities in Some Nb-Zr Alloys. *Physical Review Letters*, 6(12):671–674, Jun 1961.
- [50] Warren DeSorbo. Effect of Dissolved Gases on Some Superconducting Properties of Niobium. *Physical Review*, 132(1):107–121, Oct 1963.
- [51] S. Bhattacharya and M. J. Higgins. Dynamics of a disordered flux line lattice. *Physical Review Letters*, 70(17):2617–2620, Apr 1993.
- [52] M. Pissas, S. Lee, A. Yamamoto, and S. Tajima. Peak Effect in Single Crystal MgB₂ Superconductor for $H \parallel c$ -Axis. *Physical Review Letters*, 89(9):097002, Aug 2002.
- [53] P. H. Kes and C. C. Tsuei. Collective-Flux-Pinning Phenomena in Amorphous Superconductors. *Physical Review Letters*, 47(26):1930–1934, Dec 1981.
- [54] X. S. Ling and J. Budnick. Magnetic Susceptibility of Superconductors and Other Spin Systems. pages 377–388, New York, 1991. Plenum Press.
- [55] A. B. Pippard. A possible mechanism for the peak effect in type II superconductors. *Philosophical Magazine*, 19:217–220, 1969.
- [56] U. Yaron, P. L. Gammel, D. A. Huse, R. N. Kleiman, C. S. Oglesby, E. Bucher, B. Batlogg, D. J. Bishop, K. Mortensen, K. Clausen, C. A. Bolle, and F. De La Cruz. Neutron Diffraction Studies of Flowing and Pinned Magnetic Flux Lattices in 2H-NbSe₂. *Physical Review Letters*, 73(20):2748–2751, Nov 1994.
- [57] A. C. Marley, M. J. Higgins, and S. Bhattacharya. Flux Flow Noise and Dynamical Transitions in a Flux Line Lattice. *Physical Review Letters*, 74(15):3029–3032, Apr 1995.

- [58] W. Henderson, E. Y. Andrei, M. J. Higgins, and S. Bhattacharya. Metastability and Glassy Behavior of a Driven Flux-Line Lattice. *Physical Review Letters*, 77(10):2077–2080, Sep 1996.
- [59] X. S. Ling, J. E. Berger, and D. E. Prober. Nature of vortex lattice disordering at the onset of the peak effect. *Physical Review B*, 57(6):R3249–R3252, Feb 1998.
- [60] Takekazu Ishida, Kiichi Okuda, and Hidehito Asaoka. Sequential vortex states upon lattice melting in untwinned single-crystal $\text{YBa}_2\text{Cu}_3\text{O}_7$. *Physical Review B*, 56(9):5128–5131, Sep 1997.
- [61] Jing Shi, X. S. Ling, Ruixing Liang, D. A. Bonn, and W. N. Hardy. Giant peak effect observed in an ultrapure $\text{YBa}_2\text{Cu}_3\text{O}_{6.993}$ crystal. *Physical Review B*, 60(18):R12593–R12596, Nov 1999.
- [62] M. Marchevsky, M. J. Higgins, and S. Bhattacharya. Two coexisting vortex phases in the peak effect regime in a superconductor. *Nature*, 409, 2001.
- [63] Z. L. Xiao, O. Dogru, E. Y. Andrei, P. Shuk, and M. Greenblatt. Observation of the Vortex Lattice Spinodal in NbSe_2 . *Physical Review Letters*, 92(22):227004, 2004.
- [64] A. M. Troyanovski, M. van Hecke, N. Saha, J. Aarts, and P. H. Kes. STM Imaging of Flux Line Arrangements in the Peak Effect Regime. *Physical Review Letters*, 89(14):147006, Sep 2002.
- [65] Maria G. Adesso, Davide Uglietti, Rene Flukiger, Massimiliano Polichetti, and Sandro Pace. Transition between the Bragg glass and the disordered phase in Nb_3Sn detected by third harmonics of the ac magnetic susceptibility. *Physical Review B*, 73(9):092513, 2006.

- [66] Yaakov Kraftmakher. Modulation calorimetry and related techniques. *Physics Reports*, 356:1–117, Jan 2002.
- [67] Frank Pobell. *Matter and methods at low temperatures*. Springer-Verlag, second edition, 1996.
- [68] N. D. Daniilidis, I. K. Dimitrov, V. F. Mitrović;, C. Elbaum, and X. S. Ling. Magnetocaloric studies of the peak effect in Nb. *Physical Review B*, 75(17):174519, 2007.
- [69] Y. Shapira and L. J. Neuringer. Magnetoacoustic Attenuation in High-Field Superconductors. *Physical Review*, 154(2):375–385, Feb 1967.
- [70] Ivo K. Dimitrov. *Ultrasonic Attenuation, AC Magnetic Susceptibility, and Small Angle Neutron Scattering Studies of Vortex States in Single-Crystal Nb and V-Ti Alloys*. PhD thesis, Brown University, 2007.
- [71] A. T. Fiory and B. Serin. Observation of a “Peltier” Effect in a Type-II Superconductor. *Physical Review Letters*, 16(8):308–310, Feb 1966.
- [72] F. A. Otter and P. R. Solomon. Thermal Forces on Vortices and Entropy Transport by Vortex Flow in Type-II Superconductors. *Physical Review Letters*, 16(16):681–683, Apr 1966.
- [73] C. P. Bean and J. D. Livingston. Surface Barrier in Type-II Superconductors. *Physical Review Letters*, 12(1):14–16, Jan 1964.
- [74] P. G. de Gennes. Vortex nucleation in type II superconductors. *Solid State Communications*, 3(6):127–130, Jun 1965.
- [75] J. R. Clem. Low Temperature Physics-LT13. volume 3, New York, 1974. Plenum Press.

- [76] L. Burlachkov. Magnetic relaxation over the Bean-Livingston surface barrier. *Physical Review B*, 47(13):8056–8064, Apr 1993.
- [77] Ming Xu. Calculations of remanent magnetization for hard superconductors in various critical-state models. *Physical Review B*, 44(6):2713–2720, Aug 1991.
- [78] R. C. Richardson and E. N. Smith. *Experimental Techniques in Condensed Matter Physics at Low Temperatures*. Addison Wesley, 1998.
- [79] R.A. Hein, T.L. Francavilla, and D.H. Liebenberg, editors. *Magnetic Susceptibility of Superconductors and Other Spin Systems*. Plenum Press, New York, 1991.
- [80] U. Essmann and H. Träuble. The direct observation of individual flux lines in type-II superconductors. *Physics Letters*, 24A, 1967.
- [81] S. L. Lee, M. Warden, H. Keller, J. W. Schneider, D. Zech, P. Zimmermann, R. Cubitt, E. M. Forgan, M. T. Wylie, P. H. Kes, T. W. Li, A. A. Menovsky, and Z. Tarnawski. Evidence for Two-Dimensional Thermal Fluctuations of the Vortex Structure in $\text{Bi}_{2.15}\text{Sr}_{1.85}\text{CaCu}_2\text{O}_{8+\delta}$ from Muon Spin Rotation Experiments. *Physical Review Letters*, 75(5):922–925, Jul 1995.
- [82] J. Byrne. *Neutrons, nuclei, and Matter*. Institute of Physics Publishing, Bristol, 1995.
- [83] Ernst Helmut Brandt. Precision Ginzburg-Landau Solution of Ideal Vortex Lattices for Any Induction and Symmetry. *Physical Review Letters*, 78(11):2208–2211, Mar 1997.
- [84] V. Ramakrishnan. A treatment of instrumental smearing effects in circularly symmetric small-angle scattering. *Journal of Applied Crystallography*, 18:42–46, 1985.

- [85] J. S. Pedersen, D. Posselt, and K. Mortensen. Analytical treatment of the resolution function for small-angle scattering. *Journal of Applied Crystallography*, 23:321–333, 1990.
- [86] J. G. Barker and J. S. Pedersen. Instrumental Smearing Effects in Radially Symmetric Small-Angle Neutron Scattering by Numerical and Analytical Methods. *Journal of Applied Crystallography*, 28:105–114, 1995.
- [87] R. Cubitt, E. M. Forgan, D. McK. Paul, S. L. Lee, J. S. Abell, H. Mook, and P. A. Timmins. Neutron diffraction by the flux lattice in high-T_c superconductors. *Physica B: Condensed Matter*, 180–181:377–379, 1992.
- [88] B. Lebech P. Harris and J. S. Pedersen. The Three-Dimensional Resolution Function for Small-Angle Scattering and Laue Geometries. *Journal of Applied Crystallography*, 28:209–222, 1995.
- [89] J. W. Lynn, N. Rosov, T. E. Grigereit, H. Zhang, and T. W. Clinton. Vortex dynamics and melting in niobium. *Physical Review Letters*, 72(21):3413–3416, May 1994.
- [90] E. M. Forgan, S. J. Levett, P. G. Kealey, R. Cubitt, C. D. Dewhurst, and D. Fort. Intrinsic Behavior of Flux Lines in Pure Niobium near the Upper Critical Field. *Physical Review Letters*, 88(16):167003, Apr 2002.
- [91] C. J. Glinka, J. G. Barker, B. Hammouda, S. Krueger, J. J. Moyer, and W. J. Ortis. The 30 m Small-Angle Neutron Scattering Instruments at the National Institute of Standards and Technology. *Journal of Applied Crystallography*, 31:430–445, 1998.

- [92] C. P. Bean, R. W. DeBlois, and L. B. Nesbitt. Eddy-Current Method for Measuring the Resistivity of Metals. *Journal of Applied Physics*, 30(12):1976–1980, 1959.
- [93] N. W. Ashcroft and N. D. Mermin. *Solid State Physics*. Saunders, 1976.
- [94] N. R. Werthamer, E. Helfand, and P. C. Hohenberg. Temperature and Purity Dependence of the Superconducting Critical Field, H_{c2} . III. Electron Spin and Spin-Orbit Effects. *Physical Review*, 147(1):295–302, Jul 1966.
- [95] Warren DeSorbo. Resistive Transition and Current Density Characteristics in Superconducting Niobium Containing Dissolved Gases. *Physical Review*, 134(5A):A1119–A1135, Jun 1964.
- [96] Warren DeSorbo. The peak effect in substitutional and interstitial solid solutions of high-field superconductors. *Reviews of Modern Physics*, 36(1):90–94, Jan 1964.
- [97] D. Jaiswal-Nagar, D. Pal, M. R. Eskildsen, P. C. Canfield, H. Takeya, S. Ramakrishnan, and A. K. Grover. Vortex phase diagram studies in the weakly pinned single crystals of $\text{YNi}_2\text{B}_2\text{C}$ and $\text{LuNi}_2\text{B}_2\text{C}$. *Pramana: Indian Journal of Physics*, 66:113–130, 2006.
- [98] Robert W. Cahn. Materials science: Melting and the surface. *Nature*, 323:668–669, 1986.
- [99] R. Lortz, N. Musolino, Y. Wang, A. Junod, and N. Toyota. Origin of the magnetization peak effect in the nb_3sn superconductor. *Physical Review B (Condensed Matter and Materials Physics)*, 75(9):094503, 2007.
- [100] John C. Wheeler. The 180° rule at a class of higher-order triple points. *Physical Review A*, 12(1):267–271, Jul 1975.

- [101] Robert B. Griffiths. Thermodynamics Near the Two-Fluid Critical Mixing Point in He³-He⁴. *Physical Review Letters*, 24(13):715–717, Mar 1970.
- [102] J. F. Nagle and J. C. Bonner. Ising Chain with Competing Interactions in a Staggered Field. *The Journal of Chemical Physics*, 54(2):729–734, 1971.
- [103] Kao-Shien Liu and Michael E. Fisher. Quantum lattice gas and the existence of a supersolid. *Journal of Low Temperature Physics*, 10:655–683, 1973.
- [104] Robert B. Griffiths. Nonanalytic Behavior Above the Critical Point in a Random Ising Ferromagnet. *Physical Review Letters*, 23(1):17–19, Jul 1969.
- [105] Thomas Vojta. Rare region effects at classical, quantum and nonequilibrium phase transitions. *Journal of Physics A: Mathematical and General*, 39:143–206, 2006.
- [106] Shyam Mohan, Jaivardhan Sinha, S. S. Banerjee, and Yuri Myasoedov. Instabilities in the Vortex Matter and the Peak Effect Phenomenon. *Physical Review Letters*, 98(2):027003, 2007.
- [107] Nghi Q. Lam, Paul R. Okamoto, and Mo Li. Disorder-induced amorphization. *Journal of Nuclear Materials*, 251:89–97, 1997.
- [108] David R. Nelson. Vortex entanglement in High- T_c superconductors. *Physical Review Letters*, 60(19):1973–1976, May 1988.
- [109] David R. Nelson and H. Sebastian Seung. Theory of melted flux liquids. *Physical Review B*, 39(13):9153–9174, May 1989.
- [110] David R. Nelson and Pierre Le Doussal. Correlations in flux liquids with weak disorder. *Physical Review B*, 42(16):10113–10129, Dec 1990.

- [111] M. Cristina Marchetti and David R. Nelson. Dislocation loops and bond-orientational order in the Abrikosov flux-line lattice. *Physical Review B*, 41(4):1910–1920, Feb 1990.
- [112] Th. Giamarchy and S. Bhattacharya. *Vortex Phases, in “High Magnetic Fields: Applications in Condensed Matter Physics and Spectroscopy”*. Springer-Verlag, 2002.
- [113] D. R. Nelson. *Defects and Geometry in Condensed Matter Physics*. Cambridge University Press, Cambridge, UK.
- [114] J M Kosterlitz and D J Thouless. Ordering, metastability and phase transitions in two-dimensional systems. *Journal of Physics C: Solid State Physics*, 6(7):1181–1203, 1973.
- [115] B. I. Halperin and David R. Nelson. Theory of Two-Dimensional Melting. *Physical Review Letters*, 41(2):121–124, Jul 1978.
- [116] David R. Nelson and B. I. Halperin. Dislocation-mediated melting in two dimensions. *Physical Review B*, 19(5):2457–2484, Mar 1979.
- [117] A. P. Young. Melting and the vector Coulomb gas in two dimensions. *Physical Review B*, 19(4):1855–1866, Feb 1979.
- [118] D. R. Nelson, M. Rubinstein, and F. Spaepen. *Philosophical Magazine A*, 46, 1982.
- [119] David R. Nelson. Reentrant melting in solid films with quenched random impurities. *Physical Review B*, 27(5):2902–2914, Mar 1983.
- [120] E H Brandt. The flux-line lattice in superconductors. *Reports on Progress in Physics*, 58(11):1465–1594, 1995.

- [121] G. Blatter, M. V. Feigel'man, V. B. Geshkenbein, A. I. Larkin, and V. M. Vinokur. Vortices in high-temperature superconductors. *Reviews of Modern Physics*, 66(4):1125–1388, Oct 1994.
- [122] C. A. Murray, P. L. Gammel, D. J. Bishop, D. B. Mitzi, and A. Kapitulnik. Observation of a hexatic vortex glass in flux lattices of the high- T_c superconductor $\text{Bi}_{2.1}\text{Sr}_{1.9}\text{Ca}_{0.9}\text{Cu}_2\text{O}_{8+\delta}$. *Physical Review Letters*, 64(19):2312–2315, May 1990.
- [123] Philip Kim, Zhen Yao, and Charles M. Lieber. Vortex Lattice Structure in $\text{Bi}_2\text{Sr}_2\text{CaCu}_2\text{O}_{8+\delta}$ at High Temperatures. *Physical Review Letters*, 77(25):5118–5121, Dec 1996.
- [124] Carlo Carraro and Daniel S. Fisher. Barriers to vortex-line cutting in high- T_c superconductors. *Physical Review B*, 51(1):534–538, Jan 1995.
- [125] Y. B. Kim, C. F. Hempstead, and A. R. Strnad. Critical persistent currents in hard superconductors. *Physical Review Letters*, 9(7):306–309, Oct 1962.